



DI Alexander Schenk, BSc.

The oxygen reduction reaction in high temperature proton
exchange membrane fuel cells: Long term behaviour of
platinum-cobalt catalysts under ex-situ and in-situ conditions

DISSERTATION

in order to obtain the academic degree

“Doctor of Engineering Sciences”

at

Graz University of Technology

Supervisor:

Assoc.Prof. DI Dr. Viktor Hacker

Institute of Chemical Engineering and Environmental Technology

Graz University of Technology

Graz, November 2014

Eidesstattliche Erklärung

Affidavit

Ich erkläre an Eides statt, dass ich die vorliegende Arbeit selbstständig verfasst, andere als die angegebenen Quellen/Hilfsmittel nicht benutzt, und die den benutzten Quellen wörtlich und inhaltlich entnommenen Stellen als solche kenntlich gemacht habe. Das in TUGRAZonline hochgeladene Textdokument ist mit der vorliegenden Dissertation identisch.

I declare that I have authored this thesis independently, that I have not used other than the declared sources/resources, and that I have explicitly indicated all material which has been quoted either literally or by content from the sources used. The text document uploaded to TUGRAZonline is identical to the present doctoral dissertation.

Datum/Date

Unterschrift/Signature

to my family

“The scientific man does not aim at an immediate result. He does not expect that his advanced ideas will be readily taken up. His work is like that of the planter - for the future. His duty is to lay the foundation for those who are to come, and point the way.”

—Nikola Tesla

Preface

The work presented in this PhD thesis was carried out at the Fuel Cell Systems Laboratory at the Institute of Chemical Engineering and Environmental Technology at Graz University of Technology in cooperation with elcomax GmbH between the years 2011 and 2014. A considerable amount of the herein described work has been published under the title “*Platinum-Cobalt Catalysts for the Oxygen Reduction Reaction in High Temperature Proton Exchange Membrane Fuel Cells – Long Term Behavior Under Ex-situ and In-situ Conditions*” in *Journal of Power Sources* 266 (2014) 313-322.

In 2014 an internship at the Center for Individual Nanoparticle Functionality (CINF) at the Institute of Physics at the Technical University of Denmark (DTU) was performed. The work there provided a deeper insight into electrochemistry and a better understanding of the fundamental reactions which occur in fuel cells.

Financial support during the course of this work was provided by the Austrian Federal Ministry of Transport, Innovation and Technology (BMVIT) and The Austrian Research Promotion Agency (FFG) through the program a3plus and the IEA research cooperation. Furthermore, the support of NAWI Graz is gratefully acknowledged.

Acknowledgements

First of all, I would like to thank my supervisor Assoc.Prof. Viktor Hacker and Prof. Matthäus Siebenhofer, head of the Institute of Chemical Engineering and Environmental Technology at Graz University of Technology, for the opportunity to write this PhD thesis. I am very grateful to Viktor for his guidance and all the support I got during the course of my thesis.

Special thanks go to Markus Perchthaler from elcomax GmbH, who was like a co-tutor to me, for his commitment to guide me and his support with in-situ fuel cell testing, for the fruitful discussions and his encouraging attitude.

I am appreciative to my friends, all my colleagues of the institute and especially to all members of the Fuel Cell Systems Laboratory for their collaboration, assistance, friendship and the great time we had. In this context, I want to point out Christoph and Birgit for their support in the laboratory and Stephan for performing the equivalent circuit analysis. In addition, I thank Christoph Heinzl for preparing STEM images and Prof. Franz-Andreas Mautner for carrying out the XRD measurements.

Furthermore, I would like to thank Prof. Ib Chorkendorff, Asst.Prof. Ifan Stephens, Dr. María Escudero-Escribano and all my colleagues from the Center for Individual Nanoparticle Functionality for receiving me so friendly as a Guest-PhD student in their institution, for their help, support, guidance and friendship throughout my time at the Technical University of Denmark.

Last, and most of all, I wish to express my deepest gratitude to Dorith for her love, for motivating me in difficult times and her understanding, and to my parents and my sister, who provided me with all the help I needed.

I devote this thesis to you!

Abstract

Platinum cobalt catalysts (Pt-Co) have attracted much interest as cathode catalysts for proton exchange membrane fuel cells (PEMFCs) due to their high activity towards oxygen reduction reaction (ORR). Many of the reported catalysts show outstanding performance in ex-situ experiments. However, the laborious synthesis protocols of these Pt-Co catalysts disable an efficient and economic production of membrane electrode assemblies (MEAs). This thesis presents an economic, flexible and continuous platinum-transition metal (Pt-M/C) catalyst preparation for a large scale membrane electrode assembly manufacturing for high temperature PEMFCs.

HT-PEM cathodes were prepared by impregnating gas diffusion electrodes with precursor solutions containing dissolved Pt and Co salts. The salts were reduced into the corresponding metallic nanoparticles by applying a heat treatment. In order to improve the catalytic properties of the Pt-Co/C catalysts post-preparation treatments, i.e. acid-leaching and annealing, were identified and introduced into the manufacturing process. This processes led to an increased electrochemical surface area, improved catalytic activity towards ORR and a higher stability against the corrosive environment of the HT-PEM fuel cell.

The leached and heat-treated Pt-Co/C catalysts showed a very high stability in HT-PEM fuel cell operation under constant load and during start-stop cycling. In comparison to a commercial HT-PEM MEA the herein described Pt-Co based HT-PEM MEA performed equally, even though having approx. 20% lower Pt-loading at the cathode.

Kurzfassung

Aufgrund der hohen Aktivität gegenüber der Sauerstoffreduktionsreaktion (ORR) gelten Platin-Cobalt-Katalysatoren (Pt-Co) als vielversprechende Kathodenkatalysatoren für Protonenaustauschmembran-Brennstoffzellen (PEMFC). Viele wissenschaftliche Studien beschreiben die hervorragende Leistung dieser Pt-Co Katalysatoren in Ex-situ-Experimenten. Jedoch aufgrund der aufwändigen Synthesemethoden bzw. -vorschriften dieser Katalysatoren wird eine effiziente und wirtschaftliche Produktion von Membran-Elektroden-Einheiten (MEA) für die HT-PEMFC verhindert. Diese Arbeit präsentiert eine Möglichkeit Pt-Co Katalysatoren wirtschaftlich, flexibel und kontinuierlich herzustellen.

HT-PEMFC Kathoden wurden durch Imprägnierung von Gasdiffusionselektroden mit gelösten Pt- und Co-Salzen hergestellt. Die Salze wurden thermisch zu den entsprechenden metallischen Nanopartikeln reduziert. Um die katalytischen Eigenschaften der Pt-Co Katalysatoren zu verbessern, wurden Nachbehandlungsschritte wie Säure-Laugung und Temperung in den Herstellungsprozess eingebracht. Diese Verfahren führten zu einer erhöhten elektrochemisch aktiven Katalysatoroberfläche, zu verbesserter katalytischer Aktivität gegenüber der ORR und zu einer höheren Stabilität in der korrosiven Umgebung der HT-PEM-Brennstoffzelle.

Die gelaugten und wärmebehandelten Pt-Co/C-Katalysatoren zeigten im HT-PEM-Brennstoffzellen-Betrieb unter Dauerlast und während sog. Start-Stopp-Versuche eine sehr hohe Stabilität. Im Vergleich zu einem kommerziellen HT-PEM MEA basierend auf Pt zeigte die hergestellte Pt-Co-HT-PEM MEA eine gleichwertige Leistung, obwohl ca. 20% weniger Pt an der Kathode verwendet wurden.

Content

1	Introduction.....	18
1.1	The world energy demand – current aspects and future prospects.....	18
1.2	Renewable resources - the role of hydrogen and fuel cells.....	24
1.3	The aim of this thesis.....	30
2	Theory.....	31
2.1	Fuel cell fundamentals.....	31
2.2	High temperature PEM fuel cells.....	37
2.2.1	Improved kinetics.....	38
2.2.2	Improved tolerance towards contamination.....	38
2.2.3	Simplified water and heat management.....	40
2.2.4	Acid-base polymer electrolytes for HT-PEM fuel cells.....	42
2.2.5	Catalyst development for HT-PEM fuel cells.....	45
2.3	Oxygen reduction reaction.....	46
2.4	Platinum alloys for the oxygen reduction reaction.....	50
2.5	Pt-Co/C catalysts.....	52
3	Results and discussion.....	55
3.1	Catalyst preparation.....	56
3.2	Structural and chemical analysis.....	61
3.3	Ex-situ electrochemical studies.....	66
3.3.1	Measurement set-up and data treatment.....	66
3.3.2	Catalytic activity and degradation tests.....	72
3.4	In-situ electrochemical studies.....	82

3.4.1	Preparation of the PBI membrane	82
3.4.2	Preparation of the membrane electrode assembly	83
3.4.3	Measurement set-up and data treatment	84
3.4.4	HT-PEM single cell measurements.....	87
3.4.5	HT-PEM stack measurements.....	102
4	Summary and outlook.....	106
5	Experimental.....	110
5.1	Materials and methods	110
5.1.1	Chemicals.....	110
5.1.2	Instruments and equipment.....	111
5.1.3	Data treatment.....	112
5.2	Catalyst preparation.....	112
5.2.1	Preparation of gas diffusion electrodes	112
5.2.2	Impregnation solution.....	113
5.2.3	Reduction of the precursor salts	113
5.2.4	Post-preparation treatments.....	114
5.3	Electrochemical characterisation of the catalyst samples and data treatment 115	
5.3.1	Data treatment.....	117
5.4	Structural and chemical analysis.....	120
5.4.1	Scanning transmission electron microscopy	120
5.4.2	X-ray diffraction analysis.....	121
5.5	Fuel cell testing and characterisation.....	122
5.5.1	Membrane electrode assembly preparation.....	123

5.5.2	In-situ characterisation	124
6	References	127
7	Appendix.....	136
7.1	Abbreviations	136
7.2	List of figures.....	138
7.3	List of tables.....	143
7.4	Publication	144

*“The secret of genius is to carry the spirit
of the child into old age, which means
never losing your enthusiasm.”*

—Aldous Huxley

Chapter 1

1 Introduction

*“At some point, almost certainly
within this decade, we will peak
in the amount of oil that is
produced worldwide”*

—Richard E. Smalley, 2005

1.1 The world energy demand – current aspects and future prospects

Ever, since the rise of human civilisation, energy was and is the single most important factor for any developing society. Relying on renewable resources in early years, mankind’s demand in energy increased steadily. Beginning with the industrial revolution the worldwide need of energy faced a tremendous increase, leading to a change of the primary energy source and ending up in the modern

civilisation with its well-established fossil fuel based energy infrastructure as we know it today.

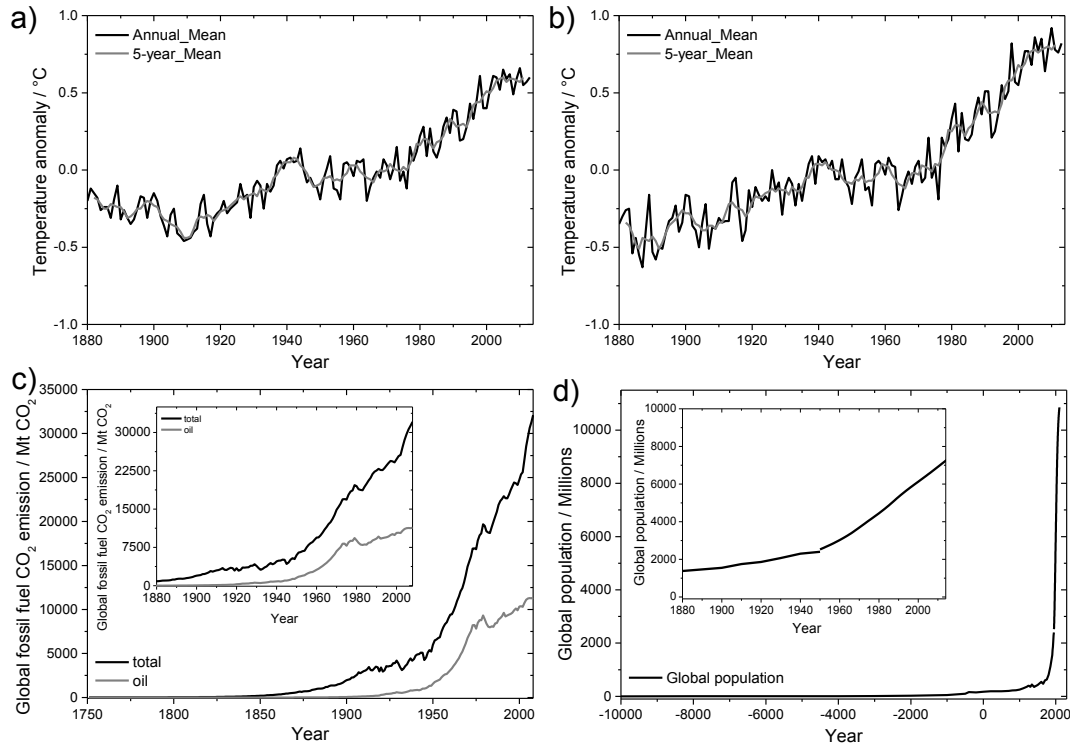


Figure 1: Global warming and causal connection to increasing CO₂ emissions and increasing global population. a) global land and ocean temperature index [1], b) global temperature (meteorological stations) [1], c) global fossil fuel CO₂ emissions (the insert shows the increase of CO₂ emissions from 1880-2014) [2], and d) global population (the insert shows the increase of population from 1880-2014) [3,4].

The data for a) and b) were obtained from NASA, Goddard Institute for Space Studies (GISS) [1]. Ad d): Note: 1950-2010 are estimates and from 2011-2100 are projected populations in the medium-fertility variant obtained from World Population Prospects 2012 by United Nations, Department of Economic and Social Affairs, Population Division [3]. The data before 1950 are the lower estimates from Historical Estimates of World Population by United States Census Bureau [4].

Within the last 40 years the worldwide consumption of energy doubled [5]. Currently, the world’s total energy consumption is accounted to 16 TW, whereof more than 80% are provided by burning fossil fuels, such as oil, natural gas or coal [6,7]. With an increasing global population, the world’s demand for primary energy is estimated to double by 2050 again. Therefore, we face a fast depletion of these fossil resources [7–9]. *“At some point, almost certainly within this decade, we will*

peak in the amount of oil that is produced worldwide”, Nobel laureate in chemistry Richard E. Smalley predicted the point at such the produced amount of fossil oil will reach its maximum by latest 2010 [8]. Even though he was wrong, dealing with evanescent fossil fuel resources has become one of the major concerns in the world.

Besides dwindling fossil energy resources, global climatic changes, negative consequences of environmental pollution and their increasing presence in the media led to a renaissance of environmental awareness within the world's population. It is a matter of fact that within the last century the average surface temperature on earth has been going up, whereby land regions have warmed faster than the oceans [1,10]. This phenomenon is usually known as global warming and coincides with a steep increase of the CO₂ concentration in the atmosphere during the same time span (see Figure 1) [2].

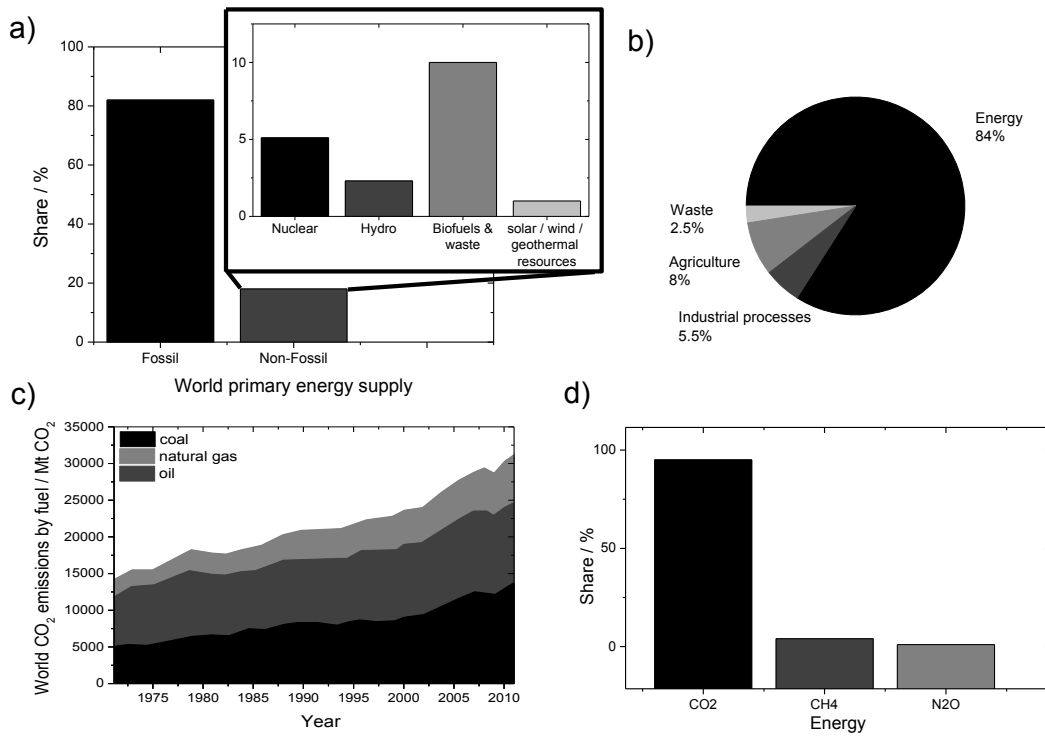


Figure 2: a) World primary energy supply 2011, shares of fuels [6,7,11], b) origin and share of anthropogenic GHG emissions [11], c) global CO₂ anthropogenic emissions by fossil fuels [5], and d) shares of different GHG emitted by energy production and consumption [11].

The causal connection between global warming, increasing global population, increasing levels of CO₂ emissions and the combustion of fossil fuels is evident. Whereby the latter, burning fossil fuels, is the single largest human influence on world's climate [11,12]. Since the industrial revolution, the demand for more and more energy led to a dramatic increase of greenhouse gas (GHG) emissions into the atmosphere. Anthropogenic GHG, like CO₂, CH₄, N₂O and O₃, accumulate in the atmosphere, perturb the Earth's energy balance with space and produce net warming, by the so-called "greenhouse-effect" [11,13]. Among all human activities, the use of energy represents more than 80% of global anthropogenic GHG emissions, originating from the production, transformation, handling and consumption of all kinds of energy commodities deriving from fossil fuels (see Figure 2) [11].

So far global warming increased world's mean temperature "only" by 0.5-1.0 °C since 1975 (Figure 1a) [1,13]. A temperature increase by 0.5-1.0 °C seems to be rather negligible, but the dramatic effects of the global warming induced climate change on our environment are already appreciable. Worldwide mountain glaciers as well as ice caps at the poles are melting and receding rapidly [14]. Increases in sea level are also consistent with melting ice masses. Between 1993 and 2003 the global average sea level rose at an average rate of about 3.1 mm per year [10]. Worldwide, weather extremes, such as droughts and floods tend to happen more frequently, as well as severe storms seem to occur more often [10,15]. Not only, but to a great extent the associated losses and costs for damage compensation of these natural catastrophes raised the public awareness towards environmental pollution and its negative consequences [15].

*“We don’t have to save the world.
The world is big enough to look after itself.
What we have to be concerned about is
whether or not the world we live in
will be capable of sustaining us in it.”*

–Douglas Adams

Both topics, energy and environment, are currently ranked in the list of the top 10 global concerns of the next century to come, as given in Table 1. Richard E. Smalley sees in energy the key to solve all of these problems in the world. For example, cheap and sustainable energy for everyone¹ will enable pure fresh water for drinking and agricultural use in large amounts by desalination of sea water. It further enables the production of food, and in the end will be a mean to increase safety worldwide and reduce conflicts all over the world [8].

Table 1: Prioritised ranking of the most critical global problems for the next 100 years [8].

<hr/> Concerns <hr/>	
1	Energy
2	Water
3	Food
4	Environment
5	Poverty
6	Terrorism and war
7	Disease
8	Education
9	Democracy
10	Population

¹ According to Richard E. Smalley, approximately only half of World’s population has access to modern energy at the level that we know from developed countries. In other words, instead of the projected 30 TW of energy, we will need worldwide approx. 60 TW in 2050 [8].

But how shall we accomplish these goals? Where do we find the “next oil”, the basis for worldwide energy prosperity in our future?

*“The future is green energy,
sustainability, renewable energy.”*

—Arnold Schwarzenegger

It is obvious, to avoid both, the future energy crisis and environmental pollution, we need to convert energy in a clean and sustainable way. Over the last decades, many efforts have been devoted to find an alternative to fossil fuels, deriving from renewable and sustainable resources [16]. But currently the shares of renewable and sustainable sources for the primary energy supply are negligible low. Considering Figure 2a, nuclear fission as well as biomass played a significant role in World’s energy supply. Since fission is a non-renewable and non-sustainable source of energy, it should not be considered as solution to the given problem of energy security, although it will be a significant energy source in our near future. Most of the used biomass was utilised in less-developed countries, where the access to modern energy is not available or affordable [8,17]. Biomass itself has great potential as future energy resource. However, keeping a growing population and a water and food deficiency in mind, biomass is topic of an ethical food-energy-controversy. Hydropower is very well developed and has only little potential in developed countries to be further increased [8,18]. Therefore, the greatest potential to become our primary energy sources are those resources we are using the less, solar energy, wind energy and geothermal heat [8].

Solar radiation will play the most significant role in World’s future energy supply, as sun provides roughly 165,000 TW of energy, which is more than 10,000 times higher than needed [8]. Furthermore, wind energy is also caused to great extent by the

difference in absorption of solar energy between the equator and the poles and would provide ground near approximately 400 TW of power [19].

Both, solar and wind energy converting technologies exhibit an extensive increase over the last 20 years [17]. Now they have reached a level of development, at which they affect, due to their intermittent nature, the grid's stability. At peak production levels the excess of energy of solar parks or wind farms needs to be stored to maintain a reliable grid. This could either be achieved by combining the wind farm with hydroelectricity, where hydroelectric plants can hold back their water during periods of blowing wind, or by using any other forms of grid storage, such as compressed air, batteries, flywheels, and hydrogen.

1.2 Renewable resources - the role of hydrogen and fuel cells

Energy resources are divided into 3 different groups: fossil fuels, nuclear resources and renewable resources. Driven by the search for reducing anthropogenic greenhouse gas emissions, improving urban air quality, ensuring energy security and creating a new industrial and technological energy basis, renewable energy resources, such as solar energy, wind energy, biomass energy, geothermal energy, etc. are going to play the most important role in future's energy supply, because they can be used over and over again at zero or almost zero emissions of GHG and air pollutants [20,21]. But due to their episodic or fluctuating nature, e.g. day/night cycle, summer/winter, weather conditions, different growth rates of plants, etc., they are considered to be unreliable. This "unreliability" causes the need for energy storage.

Besides many forms of grid storage, the chemical storage of energy in form of hydrogen (H_2), either in compressed or liquefied form, is expected to play a key role in the World's energy future [20–24].

Since centuries generations of people and visionaries, like Jules Verne, were fascinated by hydrogen and its clean and simple conversion to heat and electricity.

Hydrogen is the most common element in our universe and the third most abundant chemical element in the Earth's crust, respectively, but does not exist in its elemental form in nature. It is invariably bound up in chemical compounds and molecules, and is therefore an energy carrier but not a primary energy source. Hydrogen has to be separated from hydrogen-containing sources by heat, electricity or chemical reactions, and then be utilised in high-efficiency power generation systems, e.g. fuel cells. This can be achieved either renewable (solar, wind, hydro, biomass, geothermal) or non-renewable (natural gas, coal, nuclear) at very high efficiency from almost any primary energy source [20–23].

Today, hydrogen is economically produced in large amounts from natural gas by steam reforming. Since this method yields carbon dioxide (CO_2) as by-product, it needs to be replaced by other GHG emission-free hydrogen synthesis routes [21,23]. There are several possible and promising routes to produce hydrogen, which fulfill the goals of being CO_2 -free and sustainable. The oxygen-free high-temperature pyrolysis of hydrocarbons, biomass or municipal solid waste into hydrogen and carbon black is one of these promising processes. Furthermore, splitting up water into hydrogen and oxygen through various methods including electrolysis (using renewable electricity), photo and photo-biological splitting and high-temperature decomposition are also possible hydrogen production processes [21,23]. But also the use of nuclear fission and fusion could supply the energy for future's hydrogen production.

Besides the possibility of producing hydrogen out of diverse resources and its high abundance in Earth's crust, it offers the attractive feature of being a chemical storage medium for electricity. Especially for intermittent, renewable energy resources it is necessary to store excess electricity produced during periods of peak production for periods with insufficient electricity generation. Therefore, the storage of electricity, through electrolysis of water, in form of hydrogen provides a solution to one of the biggest obstacles of sustainable energy technologies, its unreliability.

Although the storage of electrical energy in form of chemical energy is very attractive, hydrogen related technology faces crucial barriers for its widespread uptake in the energy supply chain. Currently, there is no efficient, low-cost, low-weight and safe method for storing hydrogen [21,23]. Today, usually hydrogen is stored in compressed form in high-pressure gas containers, but there is also the option of storing hydrogen cryogenically cooled in liquid state. Since hydrogen is the lightest element in the periodic table, it takes lots of effort to compress or to liquefy it. Up to 20% and 40% of the energy content of the stored hydrogen are used for compressing and liquefying it, respectively [21]. Even though significant improvements in hydrogen (storage) technology have been made, public acceptance is not necessarily given. And there is still another major drawback: large investments need to be done to establish a hydrogen distribution and fueling infrastructure for a widespread use as energy carrier [23].

The ongoing discussion of hydrogen technology resembles the question, what came first, the egg or the hen. It is still widely discussed, if the establishment of a society based on sustainable hydrogen energy needs the important infrastructure or the necessary energy conversion technology first. In fact in both directions, storage and conversion technology, many an effort is devoted to get hydrogen energy economically viable.

A technology to convert the stored chemical energy in hydrogen into electrical energy was already discovered 176 years ago by Sir William Robert Grove and Christian Friedrich Schönbein in 1838 [25-27]. In their discovery they describe the current generated from hydrogen and oxygen dissolved in diluted acid on platinum surfaces; i.e. the reaction, which is nowadays known to occur in hydrogen fuel cells. In general, fuel cells can be considered as permanently recharging batteries. While batteries store energy, fuel cells continuously convert chemical energy very efficiently into electrical energy as long as the reactants, hydrogen and oxygen, are supplied. The reaction of hydrogen and oxygen in fuel cells produces besides the desired electrical energy only water as exhaust gas and virtually no air pollutants or greenhouse gases. Therefore, fuel cell technology is expected to be one of the key technologies for clean energy production of the future [21,23].

Fuel cell technology has seen an astonishing progress within the last 30 years and is now emerging as leading alternative to internal combustion engines in automotive applications [21]. The use of hydrogen in combination with fuel cells is an attractive alternative to carbon-based fossil fuels, and one of the few options to enable transportable power without pollutant and GHG emissions at the point of use. Additionally, fuel cell technology not only meets the criteria and energy demand for transportation, but also the needs for stationary and portable power [21,23]. Depending on the energy application at varying scales different types of fuel cells have been developed (see Table 2).

Table 2: Summary of fuel cell types [21].

Fuel cell types	Operating temperature / °C	Applications
Alkaline (AFC)	70-130	Space, military
Proton exchange membrane (PEMFC)	60-110	Mobile, portable
Direct methanol (DMFC)	60-120	Portable
High temperature PEMFC	160-200	Small-scale power and CHP
Phosphoric acid (PAFC)	175-210	Medium- to large-scale power and CHP
Molten carbonate (MCFC)	550-650	Large-scale power generation Medium- to large-scale power
Solid oxide (SOFC)	500-1000	and CHP, auxiliary power units, off-grid power and μ -CHP

A main field of fuel cell research are proton exchange membrane fuel cells (PEMFCs)². Due to their many attractive features, including high power density, rapid start-up and high efficiency the research is mainly driven by major automakers to find a low-pollutant and high-efficiency alternative to the internal combustion engines (ICE) [22]. Since fuel cells are not subject to the limitations of the Carnot cycle, they offer, unlike ICEs, high efficiency across their whole power output range. In general, fuel cells convert fuel to electricity twice as efficient as internal combustion engines [21].

Besides automotive applications of fuel cells, distributed generation of electrical energy and heat in combined heat and power (CHP) systems has emerged to be a very promising market for fuel cells [28]. In comparison to automotive applications

² The abbreviation PEMFCs is also often referred to polymer electrolyte membrane fuel cells. It is notable, that the term polymer electrolyte membrane applies to all fuel cell technologies using polymeric electrolytes, i.e. acidic and alkaline. Whereas proton exchange membranes only refer to the usage of acidic electrolytes.

different needs apply for stationary power and heat generation. Therefore, fuel cells operating at higher temperatures have been developed. High temperature fuel cells are ideal for decentralised energy generation and supply, as they produce high-grade waste heat as well as electrical power [21]. Since these high temperature fuel cells can be fuelled not only by hydrogen but also by hydrocarbons such as natural gas, this technology is independent from the development of a hydrogen infrastructure [21]. *P.P. Edwards et al.* see in high temperature fuel cells an interesting transition from today's hydrocarbon fuels to a future hydrogen economy [21]. Currently, these fuel cells offer an efficiency gain over conventional combustion of hydrocarbons. In near future high temperature fuel cells will be even more efficient when renewable biofuels become cost-effective and finally, they will operate at very high efficiencies when hydrogen is widely available [21].

Depending on the scales of combined heat and power applications or plants, different high temperature fuel cell technologies have been developed. For medium- to large-scale power supply especially solid oxide fuel cells (SOFCs) and molten carbonate fuel cells (MCFCs) have been pursued. For small-scale applications a combination of phosphoric acid fuel cells (PAFCs) and proton exchange membrane fuel cells (PEMFCs), the so-called high temperature (HT-) PEMFC has been developed [29]. In contrast to SOFCs and MCFCs, HT-PEMFCs require an external reforming of hydrocarbons to hydrogen-rich gas.

While the continuous operation over several thousand hours has been already proven by several demonstration projects, e.g. ene.field, Serenergy, Enymotion, DLR Antares, Vießmann, UTC Power and ClearEdge Power, high temperature PEM fuel cell technology still lacks a widespread commercial uptake. The main hindrance for market uptake is located in the relatively high costs of HT-PEM fuel cell systems. Reaching the cost targets and maintaining the high durability of these fuel cell

systems requires extensive research on the development of the fuel cell key component, the membrane electrode assembly (MEA) [30]. A significant cost reduction can be achieved by understanding the fundamental electrocatalytical reactions in fuel cells and tuning the electrocatalysts towards higher activity. But also an appropriate manufacturing of the MEA enables an important possibility to reduce production costs and therefore system costs effectively.

1.3 The aim of this thesis

Platinum transition metal catalysts (Pt-M) have attracted much interest as cathode catalysts for proton exchange membrane fuel cells due to their high activity towards oxygen reduction reaction (ORR) at the cathode of fuel cells. Many of the reported catalysts show outstanding performance in ex-situ experiments. However, the laborious synthesis protocols of these Pt-Co catalysts disable an efficient and economic production of membrane electrode assemblies (MEAs). Therefore, this thesis deals with the integration of an economic, flexible and continuous platinum-transition metal (Pt-M/C) catalyst preparation into a large scale membrane electrode assembly manufacturing for high temperature PEMFCs. The focus of the work is set on the establishment of an active and stable catalyst system, which opens up the possibility for the reduction of the precious metal loading, thus a cost reduction of a state-of-the-art membrane electrode assembly [31].

Chapter 2

2 Theory

“Yes my friends, I believe that water will one day be employed as fuel, that hydrogen and oxygen which constitute it, used singly or together, will furnish an inexhaustible source of heat and light, of an intensity of which coal is not capable.... When the deposits of coal are exhausted we shall heat and warm ourselves with water. Water will be the coal of the future.”

–Jules Verne, *The Mysterious Island* (1874-5)

2.1 Fuel cell fundamentals

Electricity is without doubt the most convenient and versatile carrier of energy in our world. Traditionally, electricity is produced in large centralised power plants from fossil fuels. However, nowadays there is an emerging interest of producing electricity in a smaller decentralised way, due to its higher overall efficiency and due to its better compatibility with the usage of renewable resources, e.g. wind power [29]. These changes in the energy supply chain also require new technologies for storing energy into fuels, for instance in hydrogen through the

electrolysis of water. Furthermore, these changes also involve the development of efficient ways to re-convert the fuels into electrical energy.

As described above, fuel cell technology provides all necessary properties for a decentralisation of electricity generation. Fuel cells can be thought of as solid state generators of electricity and heat by combining electrochemically a gaseous fuel and an oxidant gas through electrodes and across an ion conducting electrolyte [32].

In contrast to batteries, a fuel cell does not require any recharging. As long as a fuel cell is continuously supplied with reactants, it will produce electric energy. In comparison to any conventional thermo-mechanical system, such as internal combustion engines, fuel cells are characterised by their ability to convert the chemically stored energy of a fuel directly into electricity and heat, resulting in much higher conversion efficiencies than any current electricity generators can yield. In other words, fuel cells produce more electricity from the same amount of fuel than any combustion technology [32]. As the conversion of the fuel to electrical energy can be performed also in a very clean way, the fuel cell may represent one fundamental progress towards a sustainable society [33].

Among the most common types of fuel cells, as given in Table 2, the PEMFC is especially of interest because it uses a polymeric membrane instead of a liquid electrolyte, which enables compacter systems resulting in a high power density and easy handling [34]. In Figure 3 a schematic drawing illustrates the basic principles of a polymer electrolyte membrane fuel cell (PEMFC).

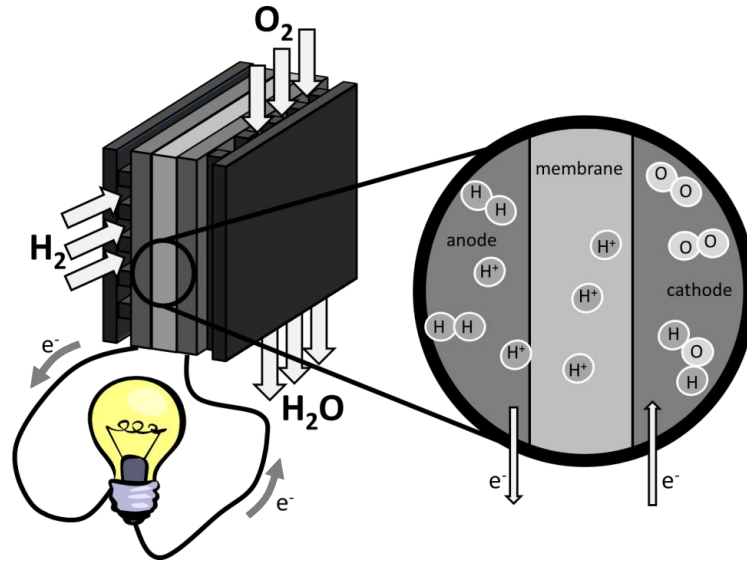
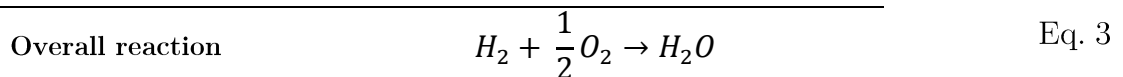
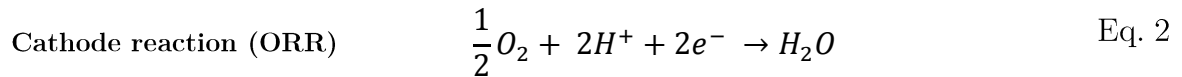
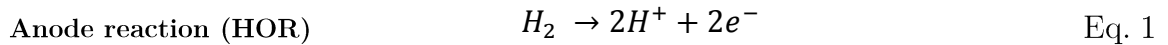


Figure 3: Scheme of a PEMFC

The most interesting part of a PEM fuel cell is the so-called membrane electrode assembly (MEA). The MEA resembles the heart or the central part of a PEM fuel cell and consists of two electrodes, i.e. anode and cathode, and the electrolyte. The electrolyte is as mentioned above a quasi-solid polymeric film. The required properties of this polymer electrolyte vary with the working condition of the fuel cell and the particular application [29]. Nevertheless, these polymer electrolytes should offer high proton conductivity and high chemical, mechanical and thermal stability in order to sustain a high lifetime of the PEMFC. Most commonly perfluorinated polymers (similar to polytetrafluoroethylene, PTFE) containing $-\text{SO}_3\text{H}$ groups (perfluorosulphonic acid, PFSA) are employed. The PTFE-like backbone provides the membrane with chemical inertness, high mechanical and good thermal stability, whereas the $-\text{SO}_3\text{H}$ groups are superacid and protogenic in hydrated state, and provide the necessary proton conductivity [29,35]. To maintain a high proton conductivity, these PFSA membranes must be hydrated at all times during operation. Usually this is achieved by leading the fuel and oxidant gases through water before introducing them into the fuel cell.

The two electrodes (anode and cathode) which are located on either side of the membrane usually consist of three layers, a carbon gas diffusion paper/cloth (Figure 15a), a highly porous gas diffusion layer and the active or catalyst layer. The gas diffusion layer is generally made out of high surface area carbon (HSAC), in order to provide a fine structured porous network in which the reactant gases can be transported to the active layer, and PTFE, which renders the gas diffusion layer hydrophobic, thus disabling a wetting and blocking of the pores with water. The active layer usually contains an active catalyst supported on HSAC, which enables the oxidation of hydrogen at the anode (HOR, hydrogen oxidation reaction) and the reduction of oxygen at the cathode (ORR, oxygen reduction reaction) [29,35].

Hydrogen (H_2) is introduced into the PEM fuel cell from the anode side, where it is converted into protons (H^+) and electrons (e^-) through the HOR. The electrons are transferred through the electrical conductive gas diffusion layer and are collected at an external circuit, providing electrical energy. The protons are transported through the polymer electrolyte membrane to the cathode. Once protons reach the cathode side, they react with oxygen (O_2) and electrons producing water (H_2O) via the ORR [29,33,35]. The reactions which occur at the anode and the cathode are summarised below.



Considering both reactions, HOR and ORR, the thermodynamical theoretical cell voltage of a H_2/O_2 fuel cell can be described by a combination of the two Nernst

equations for the anode and cathode and would be 1.229 V at standard conditions [34,35].

$$V_{theory} = E_{O_2/H_2O}^0 - E_{H_2/H^+}^0 + \frac{2.303 RT}{zF} \cdot \log \left(\frac{p_{O_2}^{\frac{1}{2}} p_{H_2}}{p_{H_2O}} \right) \quad \text{Eq. 4}$$

with the two standard electrode potentials at 1.0 atm and 25 °C

$$E_{H_2/H^+}^0 = 0.000 \text{ V} \quad \text{Eq. 5}$$

$$E_{O_2/H_2O}^0 = 1.229 \text{ V} \quad \text{Eq. 6}$$

Where R is the universal gas constant (8.314 J K⁻¹mol⁻¹), F the Faraday constant (96,485 C mol⁻¹), T the temperature and p the corresponding partial pressures of the reactant gases and the product water.

However, the real cell voltage, i.e. the performance of a fuel cell is affected by several significant voltage losses, which lower the power output dramatically (see Figure 4) [36]. For instance, the partial pressure of oxygen is reduced when air is supplied to the cathode.

$$V_{cell} = E_{rev} - \Delta E_{ohmic} - \eta_{ORR} - \eta_{mt} \quad \text{Eq. 7}$$

The reversible cell voltage E_{rev} describes the reduced theoretical OCV by considering the real partial pressures of the reactant gases and the operating temperature of the fuel cell. The ohmic losses E_{ohmic} result from the contact resistances between flow-fields and the gas diffusion layers as well as from proton conduction through the electrolyte membrane. The slow transport of oxygen (usually hydrogen

transportation is negligible) causes mass-transport losses η_{mt} . But the most significant loss is due to overpotential losses η_{ORR} of the slow reaction kinetics of the oxygen reduction reaction [34].

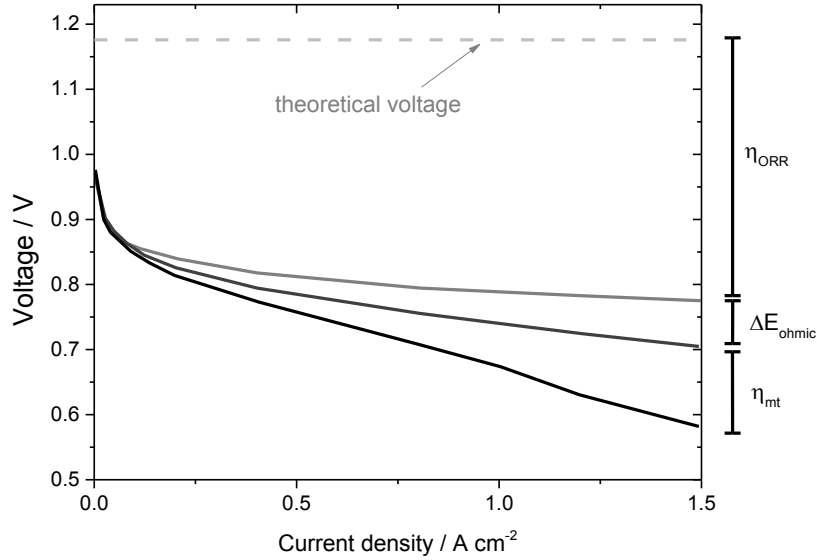


Figure 4: Influence of different loss mechanisms on the VI-characteristic of a PEM fuel cell. Figure adapted from [36].

The electrical efficiency of a PEM fuel cell can be given as the ratio of electrical energy output to energy input. However, there is no general definition of efficiency since the energy value of hydrogen varies in dependence of the aggregation state of the product water. When the product water is obtained in liquid form, the so-called higher heating value ($\Delta H^0_{HHV} = -285.6 \text{ kJ mol}^{-1}$) defines the overall reaction enthalpy (heat energy), while the so-called lower heating value ($\Delta H^0_{LHV} = -241.2 \text{ kJ mol}^{-1}$) is obtained when product water is in gaseous state [34].

Since there are also irreversible losses in form of heat ($T\Delta S$) the maximum electrical work that the fuel cell can generate (Gibbs free energy) is reduced to $\Delta G^0 = -237.4 \text{ kJ mol}^{-1}$, using Eq. 8.

$$\Delta G^0 = \Delta H^0 - T\Delta S \quad \text{Eq. 8}$$

Table 3: The theoretical cell voltage depending on the total reaction enthalpy.

	kJ mol ⁻¹	E _{th} / V
ΔH_{HHV}	-285.6	1.48 (E _{th,l})
ΔH_{LHV}	-241.2	1.25 (E _{th,g})
$\Delta G = \Delta H - T\Delta S$	-237.4	1.23 (E _{rev})

The theoretical electrical energy efficiency (η_{id}) of a fuel cell can be defined as

$$\eta_{id} = \frac{\Delta G}{\Delta H_{HHV}} = \frac{E_{rev}}{E_{th,l}} = 0.83 \quad \text{Eq. 9}$$

which results in a value of 83% in the case of HHV and liquid product water.

The electric efficiency of an operated fuel cell can be given by

$$\eta_{el} = \frac{E}{E_{rev}} \quad \text{Eq. 10}$$

and varies for a PEMFC in a range of 35 – 70%.

2.2 High temperature PEM fuel cells

Usually proton exchange membrane fuel cells operate in a temperature range below 90 °C. However, to overcome some of the problems, which are related to the low temperature (LT-) operation of PEM fuel cells, the development of high temperature (HT-) PEMFCs has been pursued. The main disadvantages of LT-operation are the slow electrode kinetics, a rather low tolerance towards

contamination of the fuel stream and a complicated water and heat management. Operating fuel cells at elevated temperatures (above 90 °C) can solve these potential problems.

2.2.1 Improved kinetics

In LT-PEMFCs the exchange current density of the oxygen reduction reaction (ORR) on Pt-based catalysts is between $10^{-9} - 10^{-8}$ A cm⁻². This exchange current density can be expressed by:

$$i_{O_2}^0 = I_{O_2}^0 \cdot e^{-\frac{E_a^0}{RT}} \quad \text{Eq. 11}$$

Where $i_{O_2}^0$ is the exchange current density for the ORR, $I_{O_2}^0$ the cathodic exchange current density at infinite temperature, E_a^0 the activation energy for the ORR, R the universal gas constant and T the operation temperature. As can be seen from Eq. 11, the ORR exchange current density will increase subsequently as the operation temperature increases [35,37–39].

2.2.2 Improved tolerance towards contamination

Usually the supplied gases, hydrogen and air, contain undesired impurities or contaminants. These contaminants in the air stream derive from industry, traffic and agriculture, and are mainly nitrogen oxides, sulphur oxides, carbon oxides and volatile organic compounds, whereas in the hydrogen stream the main contaminants are carbon oxides, hydrogen sulphide and sulphur oxides. Potentially all of these contaminants can poison the catalysts at the cathode and the

anode, respectively, and lead to a decrease in performance of the fuel cell [37–43]. In general, contamination from the air stream varies with the environmental situation, e.g. city and country side. However, contamination from the hydrogen stream derives from the hydrogen production process. Currently, hydrogen is generated by steam reforming of various organic fuels, such as methane (natural gas), methanol and gasoline [37,40,44,45]. The resulting hydrogen rich gas typically contains 40-70% H₂, 10-25% CO₂ and 1-5% CO and small quantities of inert gases, water vapour and sulphur compounds [40]. Among all listed impurities CO is the most critical with respect to catalyst activity, even trace amounts of CO as low as 10-20 ppm can lead to a significant loss in cell performance at LT operation due to blocking active Pt catalyst sites for hydrogen oxidation. CO adsorption at platinum surfaces is favoured at low temperatures; increasing the operation temperature of the fuel cell reduces the strength of CO adsorption to the Pt catalysts surface, resulting in a higher tolerance towards contamination (see Figure 5).

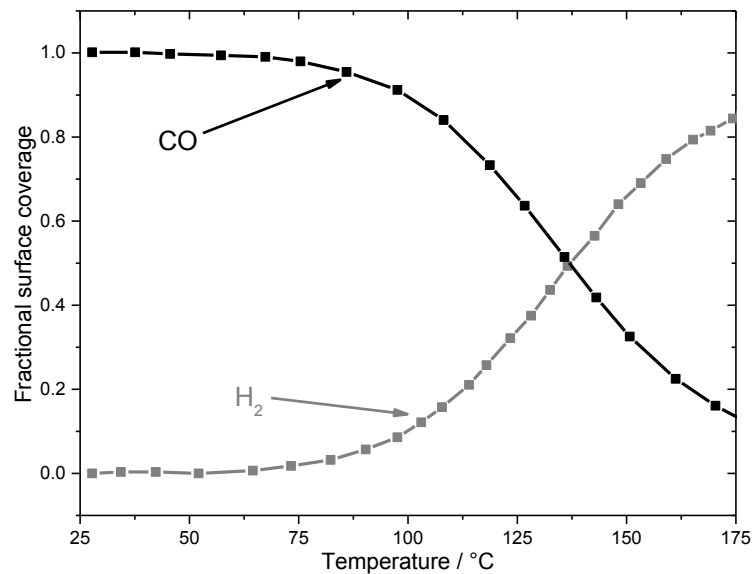


Figure 5: Langmuir-type adsorption of hydrogen and carbon monoxide on platinum as a function of the temperature. Adopted from [37].

2.2.3 Simplified water and heat management

Water management affects the overall power density and efficiency of PEM fuel cell systems and therefore its technical design is of very high importance. As described above, water is critical for low temperature operation of fuel cells to keep the PFSA membranes hydrated, thus maintaining high proton conduction. Typically, complicated humidifier systems are employed to humidify the anode and cathode feed gases, hydrogen and air, respectively, to provide high water content inside the PEMFC [29,37,38]. Nevertheless, too much water inside the fuel cell can lead to a so-called flooding event. Especially at the cathode, where the product water is formed by the electrochemical conversion of hydrogen and oxygen, excess water can fill the porous structure of the catalyst and gas diffusion layer or blocking the gas transport channels of the flow fields. Thereby the gas transport is hindered and the overall performance of the fuel cell decreases. However, in HT-PEM fuel cells usually acid-base polymer membranes, e.g. polybenzimidazole (PBI) in combination with phosphoric acid H_3PO_4 , are employed instead of perfluorosulphonic acid polymers. These acid-base polymers can operate up to 200 °C without any humidification [29,37,38,46]. At such elevated temperatures the cell and system design of a PEMFC can be significantly simplified, since flooding issues are less pronounced due to generation of gaseous product water and no humidification of the membranes is necessary. Furthermore, due to the absence of liquid water less mass-transport limitation occurs in the catalyst and gas diffusion layers and the flow field design can be simplified into parallel channels. All in all, the high temperature operation of a PEM fuel cell enables a completely simplified water management. Another benefit of HT-operation of a PEMFC arises out of the lack of liquid water in the system. During shut-down of the system less water will remain in the fuel cell, which is particularly of advantage when the environmental temperatures fall below 0 °C. Residual water will freeze at such temperatures and expand due to formation

of ice crystals, which could damage the membrane and structural integrity of the gas diffusion electrodes and catalyst layers. The less water remains in the system the less damage can occur to the electrodes and membranes [37,38].

Additionally, to the easy water management in an HT-PEMFC the heat management can also be simplified. Due to the exothermic reaction of hydrogen and oxygen towards water a fuel cell produces lots of heat during operation. This heat needs to be removed to keep the cell temperature at a reasonable value and maintain the good performance and high efficiency of the fuel cell. At low temperatures this is achieved by using a water- or oil-based cooling system. At elevated temperatures excess heat can be removed much faster. The higher the difference between environmental temperature and operation temperature, the easier and faster the removal of heat can be achieved. This means that due to HT-operation of a PEMFC the cooling system can be 3-4 times smaller than at LT-operation, which will increase the overall mass-specific and volume-specific power density of the PEM fuel cell system [37,38,47]. Furthermore, excess heat at such high temperatures can be utilised usefully for other purposes, such as warm water generation, thus increasing the overall efficiency of the PEMFC system. Nowadays, several companies have stationary heating systems based on HT-PEM fuel cell technology (e.g. elcore GmbH) in their product range [37,38,47].



Figure 6: Smart heating system for single-family households based on natural gas reforming and HT-PEM fuel cell technology. This picture has been provided by elcore and elcomax GmbH.

2.2.4 Acid-base polymer electrolytes for HT-PEM fuel cells

Due to the dependence on liquid water of perfluorosulphonic acid polymer membranes, water-content independent acid-base polymers have been developed for high temperature operation of PEMFCs. This type of polymers offers high proton conductivity without the need for a high degree of humidity inside the PEM fuel cell. In general, these polymers are made up of basic sites, such as ether-, alcohol-, imine-, amide- or imide-groups [37]. These functional groups of the polymer can react with strong acids in order to provide the necessary proton conductivity for high temperature operation of PEMFCs. However, to enhance the proton conductivity of the acid-base membrane a high acid content is needed. Unfortunately, this can decrease the mechanical strength of the polymers or even worse, degrade the membrane especially at higher temperatures [37]. Fortunately, there has been found one exception among all these possible acid-base polymers. Polybenzimidazole (PBI, see Figure 7) membranes doped with phosphoric

acid offer high thermal, chemical and mechanical stability at temperatures as high as 200 °C [29,37,38,46,48,49].

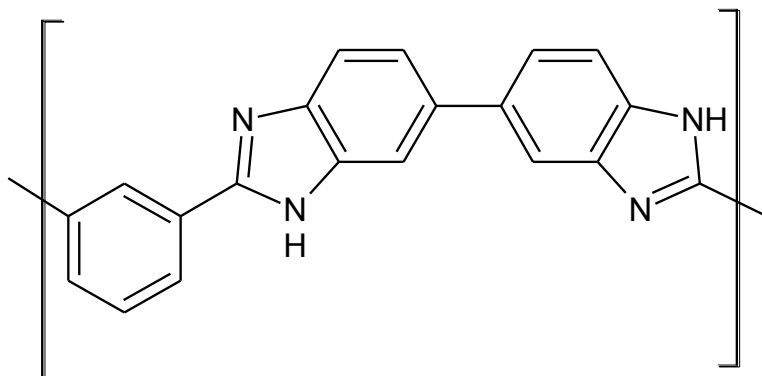


Figure 7: Chemical structure of Polybenzimidazole.

PBI is an amorphous thermoplastic polymer with a glass transition temperature above 420 °C. Doping PBI with phosphoric acid leads to the absorption of two H_3PO_4 molecules per monomeric unit of the polymer resulting in the protonation of the imine group at the imidazole ring resulting in the formation of the corresponding salt (see Figure 8).

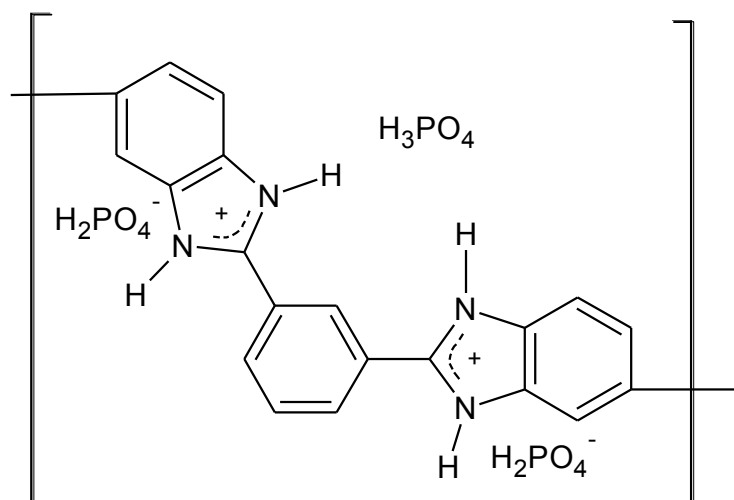


Figure 8: Structure of phosphoric acid-doped Polybenzimidazole.

For providing a high proton conductivity, free (excess) phosphoric acid is needed as the ion conductivity results from an Arrhenius law based hopping conduction mechanism [37,46,48,49].

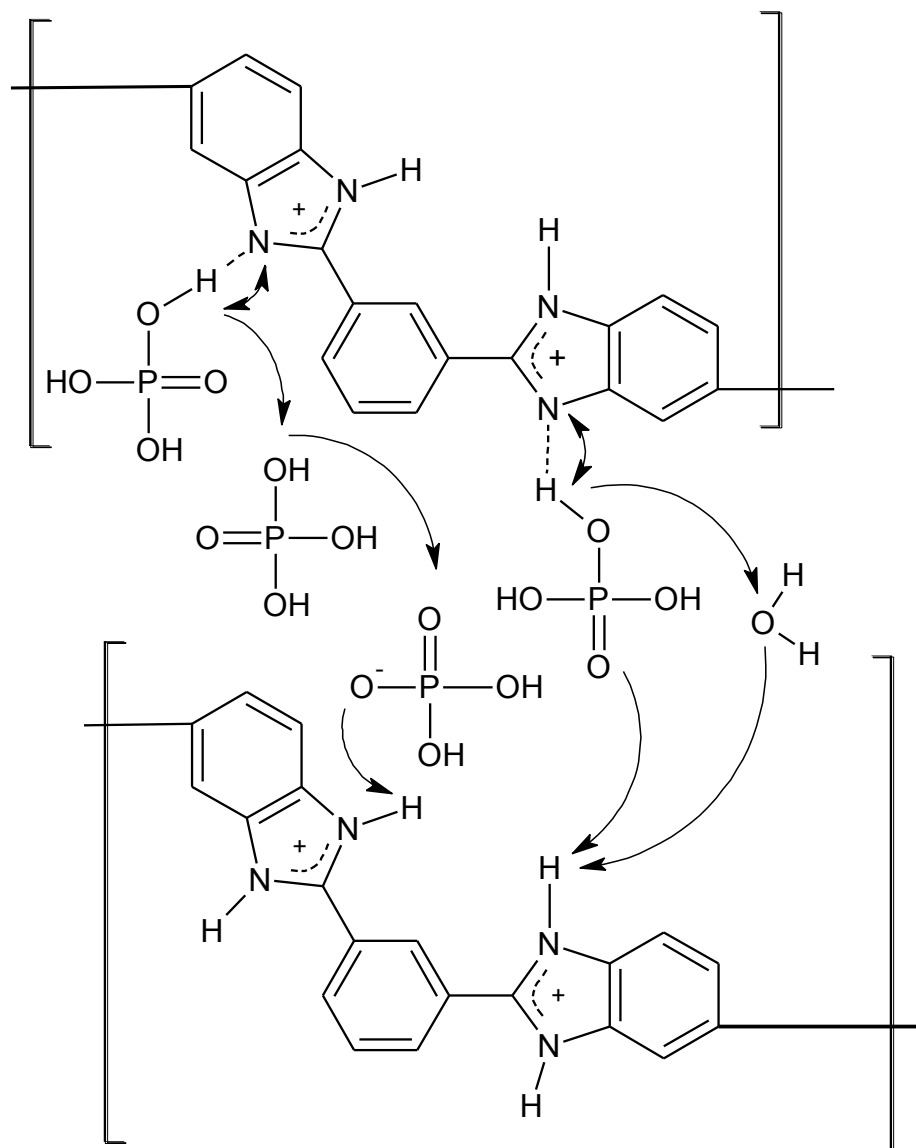


Figure 9: Proposed proton conduction mechanism (proton hopping). Figure adapted from [50-53].

The proton hopping from one N-H site to another in the PBI-polymer contributes only a little to the proton conductivity itself, but the hopping from the N-H of the imidazole ring to the phosphoric acid anions (H_2PO_4^-) significantly contributes to the conduction of the protons [37,50].

2.2.5 Catalyst development for HT-PEM fuel cells

Besides the positive effects of PEM fuel cell operation at elevated temperatures, some drawbacks or challenges are given by operating temperatures above 90 °C. With increasing temperature, not only reaction kinetics of hydrogen oxidation and oxygen reduction are speeding up and the catalyst's tolerance towards contamination is rising up, but also degradation mechanisms are accelerated. Especially the degradation of the electrocatalysts is favoured at higher operating temperatures [37].

In low temperature PEMFCs three major degradation mechanisms have been identified:

- Particle agglomeration, through Ostwald ripening or coalescence [54]
- Dissolution or detachment of platinum-based catalysts [55,56]
- Carbon corrosion [57,58]

It has been found that carbon corrosion, i.e. the oxidation of the carbon support materials in the gas diffusion electrodes and catalyst layers is more pronounced at high temperature PEM fuel cell operation [37]. By losing carbon support material through oxidation, the catalyst nanoparticles tend to agglomerate, which reduces the electrochemical active surface area. Furthermore, by losing carbon support material catalytic activity decreases through the detachment of Pt catalysts, which means the catalysts are not contacted by an electron conducting material and therefore lost for the electrochemical conversion of hydrogen and oxygen towards water [37,38,59–62].

In order to avoid the loss of catalysts and catalyst agglomeration, support material with high thermal and chemical stability, high electrical conductivity and high surface area needs to be developed. This can be achieved by substituting the carbon support material by non-carbon materials, such as metal oxides or metal carbides, or by substituting amorphous carbon through graphitised carbon [37,63,64].

Besides increasing the stability of the support material, new catalysts having a higher activity than pure platinum need to be developed in order to decrease the high platinum loading at the electrodes, especially at the cathode. A potential way to increase the activity of platinum towards oxygen reduction reaction will be discussed later in “Platinum alloys for the oxygen reduction reaction”.

2.3 Oxygen reduction reaction

The oxygen reduction reaction in fuel cells can be described by Eq. 2.



To enable this reaction usually a catalyst is used at the cathode in fuel cells. In order to find an appropriate catalyst offering the highest activity towards ORR the best way is to follow the principle of Sabatier [65]. In his work Paul Sabatier discussed that the optimum catalyst can be found by correlation of reactivity and inertness, meaning that the interactions between the catalyst and the reactant should be neither too strong nor too weak. Regarding the ORR, the catalyst needs to be sufficiently reactive to activate, i.e. bind, the oxygen molecule and at the same moment to be sufficiently noble to release oxygen and product water fast enough [33,66,67].

Graphically, the principles of Sabatier can be illustrated in so-called volcano plots by plotting the catalyst activity as a function of the oxygen binding energy (Figure 10).

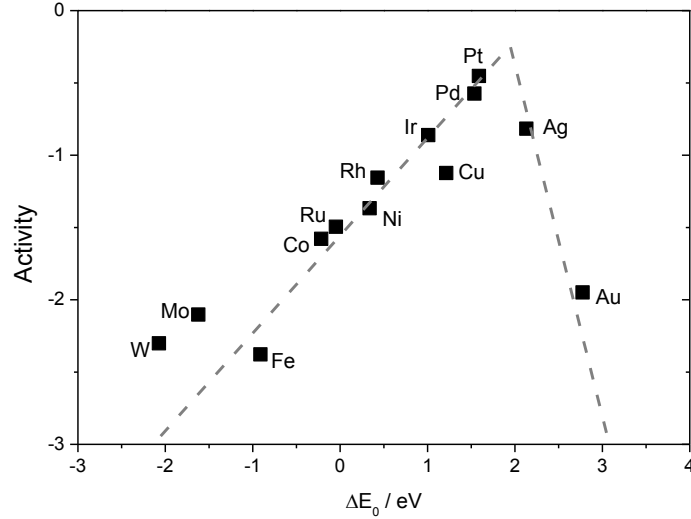


Figure 10: Activity of pure metals towards oxygen reduction reaction described in form of a volcano plot. Adapted from [68].

The most active catalyst towards ORR can be found at the top of the volcano. Among pure metals platinum offers the highest activity for reducing oxygen into water. At the left side of the volcano higher reactive metals, such as palladium or iridium, which bind oxygen too strongly, are located, whereas at the right side too noble metals, such as silver and gold, for the ORR can be found [33,68].

However, even though platinum is the most active metal towards ORR the sluggish reaction kinetics of the oxygen reduction reaction (ORR) at the platinum catalyst surface are mainly responsible for the cell voltage drop during PEMFC operation (Figure 4 and Figure 11). Approximately 75% of the efficiency loss in PEM fuel cells are assigned to the generation of heat due to the ORR overpotential [33,36].

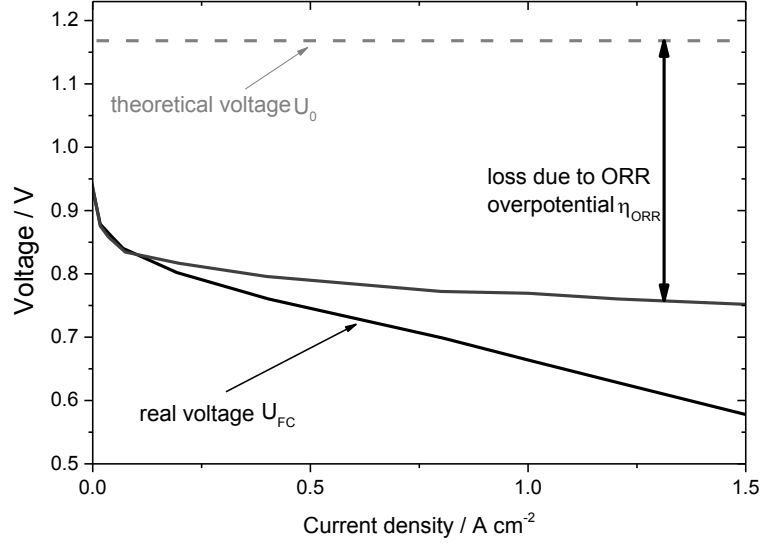
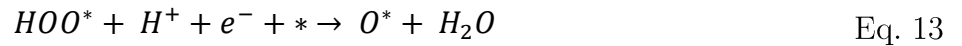


Figure 11: Description of the UI-characteristics of a state-of-the-art PEM fuel cell using a Pt/C catalyst at both electrodes. The figure is adapted from [36].

In order to understand the origin of the high overpotential for reducing oxygen into water at the surface of Pt Eq. 2 can be described by the following reaction mechanism:



The asterisk (*) symbols the active site on a catalytic surface, at which the reaction intermediates HOO^* , HO^* and O^* are adsorbed through the oxygen atom. The described first step of the reaction mechanism is usually known as associative mechanisms. In literature this step is discussed controversially, since the direct dissociation of oxygen into O^* ($O_2 \rightarrow 2O^*$) could also occur [33,68,69]. However, in the high potential region around 0.9 V, which is most relevant for the ORR, it has

been shown that the associative mechanism determines the top of the volcano [33,70].

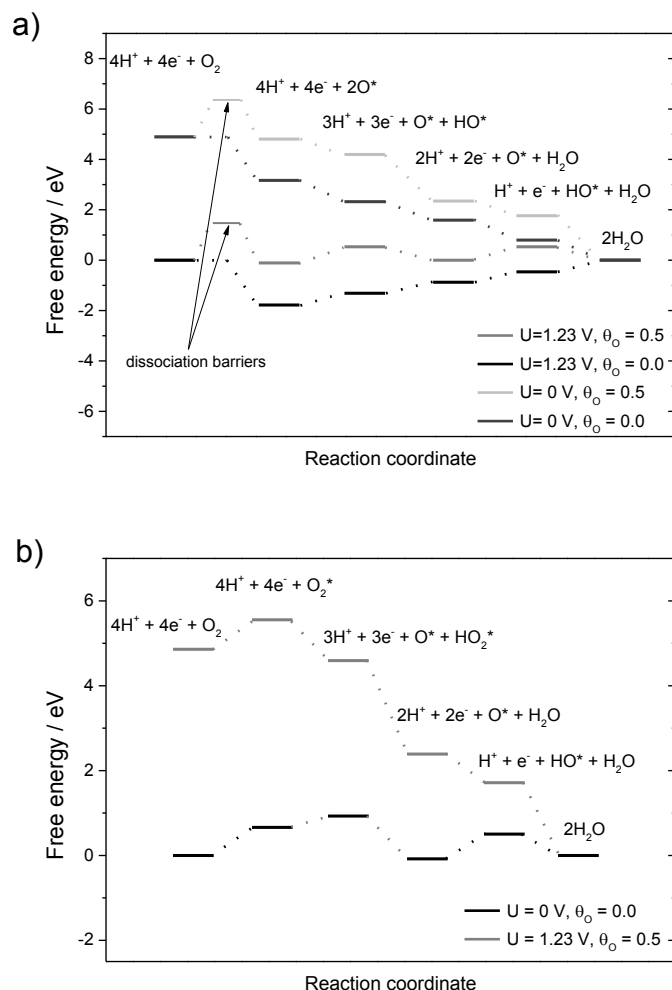


Figure 12: Reaction coordinates for the oxygen reduction reaction, a) dissociative and b) associative mechanism at different potentials and having different oxygen coverage at the Pt (111) catalyst surface. Adapted from [68].

In Figure 12 it can be seen that at low oxygen coverage ($\Theta = 0$) at a potential of 1.23 V the dissociative mechanism has the lowest barriers for the oxygen reduction, while at higher oxygen coverage of the catalyst surface ($\Theta = 0.5$), the associative mechanism is dominant [68]. Figure 13 illustrates the associative mechanism at a potential of 0.9 V versus the reversible hydrogen electrode (RHE), where typically ORR catalysts are benchmarked. The formation of HOO^* , which is given in Eq. 12,

and the desorption of the product water, which is described in Eq. 15, are uphill in free energy, which means these two reaction steps need energy in order to take place. This need in energy is usually seen through a decrease in cell voltage due to overpotentials [71].

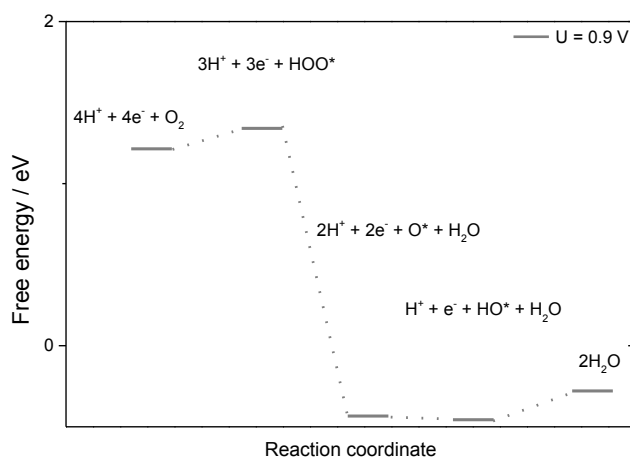


Figure 13: Reaction coordinate for the oxygen reduction reaction following the associative mechanism at a potential of 0.9 V_{RHE} at the Pt (111) catalyst surface. Adapted from [67].

Furthermore, Figure 12 and Figure 13 show that Pt is not even close to be the optimum catalyst for the ORR, otherwise Pt would exhibit a flat free energy diagram at the equilibrium potential of 1.23 V under standard conditions [33].

2.4 Platinum alloys for the oxygen reduction reaction

In order to counteract the ORR overpotential induced performance losses, usually high platinum loadings are employed at the cathode, thus increasing the overall cost of the PEM fuel cell system. *Stephens et al.* numbered the Pt-need for 100 kW PEM fuel cell stack to approx. 50 g or 0.5 g kW⁻¹ [71]. However, to facilitate

the commercialisation of PEMFC technology, especially in the automotive market, the overall Pt loading should be reduced to economically viable 3-5 g [71].

To achieve this challenging task, new catalysts having a higher activity than pure Pt need to be developed. However, the operating conditions in a PEM fuel cell require a certain stability to concentrated acid and simultaneous electrochemical potential load. Not many materials possess these properties; therefore, probably the best approach to this challenge is to increase the activity of platinum itself [36,71].

Over the last two decades substantial efforts have been dedicated to find new catalyst systems for fuel cells. Keeping in mind the free energy diagram depicted in Figure 13 it is obvious that a better catalyst than pure Pt would bind HOO^* more strongly, while binding the HO^* intermediate of the associative ORR less strongly [33,71]. However, it has been found that it is impossible to tune the binding energy of the ORR intermediates separately, leaving behind only one possible way for increasing the activity towards ORR: finding a catalyst surface, for which the needs in free energy of the two uphill reaction steps (Eq. 12 and Eq. 15) are equal [33,68,71].

It has been shown that by using an appropriate combination of platinum with other metals (e.g. Pd, Ru, V, Cr, Co, Ni, Cu etc.) it is possible to increase the activity towards ORR significantly and thereby reduce the Pt loading at the cathode [36,71–82]. According to the activity results of various Pt based ORR catalysts a new volcano emerged, using the difference in the binding energy of oxygen (intermediates) at the Pt-alloy catalyst surfaces in comparison to the oxygen binding energy of pure Pt (see Figure 14).

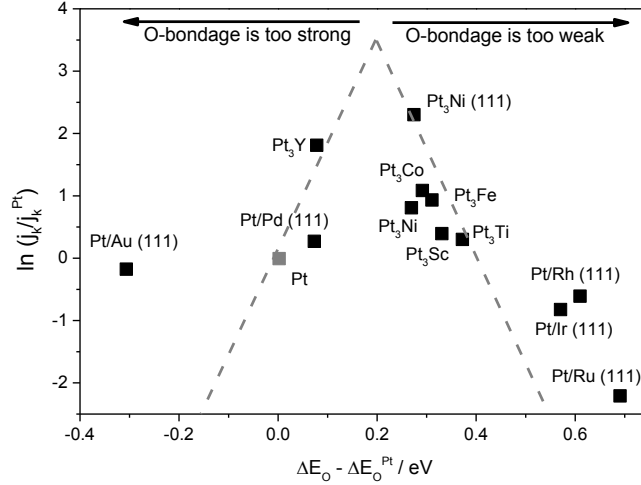


Figure 14: A combined experimental and theoretical ORR volcano described by the difference in oxygen binding energy of the Pt-alloys in comparison to pure Pt. Figure adapted from [73]

In particular, among all these possible ORR catalysts the formation of platinum alloys with late transition metals such as Co has been investigated extensively even though it is far from being at the top of the volcano [76,80–88].

2.5 Pt-Co/C catalysts

Various Pt-based alloys with late transition metals exhibit an increased activity towards ORR with respect to pure Pt. Especially Pt-Ni and Pt-Co alloys have been found to demonstrate high ORR activities. However, the gain in activity is usually lost after short operating time. The less noble transition metals within the alloys are not thermodynamically stable under the corrosive conditions of the PEM fuel cell cathode and tend to dissolve into the electrolyte [71,72,89]. This dealloying process results in Pt-enriched surface structures, i.e. a Pt-overlayer which protects the bulk from further dissolution [71,73,90,91]. Two structures of overlayers have been identified and were denoted by *Stamenkovic et al.* as *Pt-skeleton* and *Pt-skin* structures [69,71,73,87,90,91]. The dissolution of the solute (less noble) metal into

the electrolyte results in the Pt-skeleton structure. Typically this structure contains only negligible amounts of the transition metal, which has been used for alloying and exhibits a Pt-overlayer of 1-2 nm in thickness [76,90,92]. In the second case the Pt-overlayer is formed during annealing the Pt-alloy in inert or vacuum atmosphere. Due to the lower surface energy of Pt, in comparison to the transition metal, Pt migrates to the catalyst's surface, leading to a so-called Pt-skin structure [31,71,73,87,90].

Various studies aimed to find the mechanism behind the higher ORR activity of these alloys. It has been found that, if the less noble metal would be effectively present in the surface of the alloy, the oxygen dissociation or the removal of OH radicals from the Pt sites could be facilitated by bi-functional effects [33,92,93]. However, as described above all these Pt-based alloys of late transition metals are thermodynamically not stable in the acidic and oxidative environment of a PEMFC, thus in all cases the surface is constituted by Pt-overlayers. Therefore, the increase in activity towards ORR cannot be explained by the bi-functional effects, but only by modification of the electronic properties of the Pt-overlayers through the solute metal. A change in the electronic structure of the surface-Pt could result in its weakened binding of ORR intermediates. Two different ways of changing the electronic structure of the Pt-overlayers have been identified, i.e. either by *ligand* or *strain effects* [33,73,74,92,94,95]. Ligand effects derive from the electronic interaction of the Pt-surface atoms and the subsurface atoms of the less noble alloying element [74]. Strain effects are caused by the lateral compression or expansion of the Pt-overlayer. Typically, this lateral changes are a consequence of imposing the Pt-overlayer on a substrate with different lattice parameters compared to pure Pt [74]. The enhancement of the ORR activity by strain effects can be explained by a shift of the d-band centre of Pt, e.g. lateral compression would lead to a downshift of the energetic d-band centre and result in a weakening of the binding of ORR intermediates at the Pt-surface [33,74,92,96]. The increased activity of Pt-Co

towards ORR can be explained by strain effects. Pt-Co alloys offer the same fcc cubic structure as Pt does, but with a compressed lattice parameter, (induced by the smaller covalent atomic radius of Co). An imposed Pt-overlayer on top of a Pt-Co bulk structure would lead to the above described lateral compression of the Pt-overlayer [33,97].

Usually these electronic effects have been studied on extended surfaces, i.e. single- and polycrystalline samples. Even though it is known that these Pt-transition metal catalysts are thermodynamically unstable³, their transfer to nanoparticulate form is of high interest, since they allow a reduction of the Pt-loading in the membrane electrode assembly. Typically, these Pt-alloys are supported on high surface area carbon (HSAC) and are 2-4 times more active than pure Pt [33,98]. In order to reproduce the superior properties, to stabilise the active Pt-overlayer on the Pt-transition metal (Pt-M) nanoparticles and to protect the polymer electrolyte membrane from dissolved metal ions, the Pt-M/C catalysts are pre-leached in acidic solutions and annealed [31,36,87].

³ It should be noted, that even pure Pt exhibits a considerable degradation in nanoparticulate form under PEMFC operating conditions [54,92].

Chapter 3

3 Results and discussion

*“I was bold in the pursuit of knowledge,
never fearing to follow truth and reason
to whatever results they led.”*

–Thomas Jefferson

Every single step of the herein presented catalysts manufacturing has been designed to fit into a continuous MEA production process, such as roll-to-roll production. In collaboration with the industrial partner elcomax GmbH the following production steps, deriving from their standard catalyst deposition, were chosen as outline for the development of a large-scale Pt-M based membrane electrode assembly preparation:

- i) deposition of high surface area carbon (HSAC) on carbon paper,
- ii) impregnation with metal salt containing solutions,
- iii) reduction of the precursor salts to metallic nanoparticles,
- iv) stabilisation of the Pt-M nanoparticles,
- v) doping of the active electrode layer with phosphoric acid and
- vi) assembling of the MEA.

The idea behind the continuous deposition of the catalysts directly on the, for HT-PEMFC usage optimised, porous layer of the gas diffusion electrode lies in the better utilisation of platinum. The scrap, which could be produced during the manufacturing of the porous layer, contains no expensive catalyst which means higher scrap rates can be accepted without affecting the price of the final product. In contrast, conventional impregnation of catalysts onto HSAC and casting it afterwards onto the gas diffusion layer leads to a higher loss of Pt during the production and therefore to a more expensive process. Furthermore, Pt can be enclosed in carbon aggregates during conventional deposition and is therefore lost for the electrocatalytic reactions. Moreover, the herein presented continuous MEA fabrication is much more time and cost saving, since batch processes, such as conventional loading of the HSAC, filtering or centrifugation, multiple washing, drying and annealing steps in tube furnaces, are eliminated [31].

3.1 Catalyst preparation

In the early stage of this work, pure Pt catalysts have been prepared in order to find suitable impregnation methods, solvents and reduction processes. Based on this preliminary work, together with Christoph Grimmer many an effort was

devoted to find the optimal impregnation solution and reduction method for implementing platinum-cobalt based catalysts into the above described continuous membrane electrode assembly production process. In this context, platinum and cobalt salts in various ratios, different reducing agents, different temperatures for the thermal initiation of the precursor salts reduction to nanocrystalline catalyst particles were tested, and several stabilising procedures, e.g. acid leaching, additional platinum layers, annealing steps and adding surfactants into the catalyst production process were employed. The experimental process of finding the right composition of the impregnation solution and the variation of reduction and post-preparation treatment parameters is already described in detail in the master thesis of Christoph Grimmer [99] and will not be further discussed in this thesis.

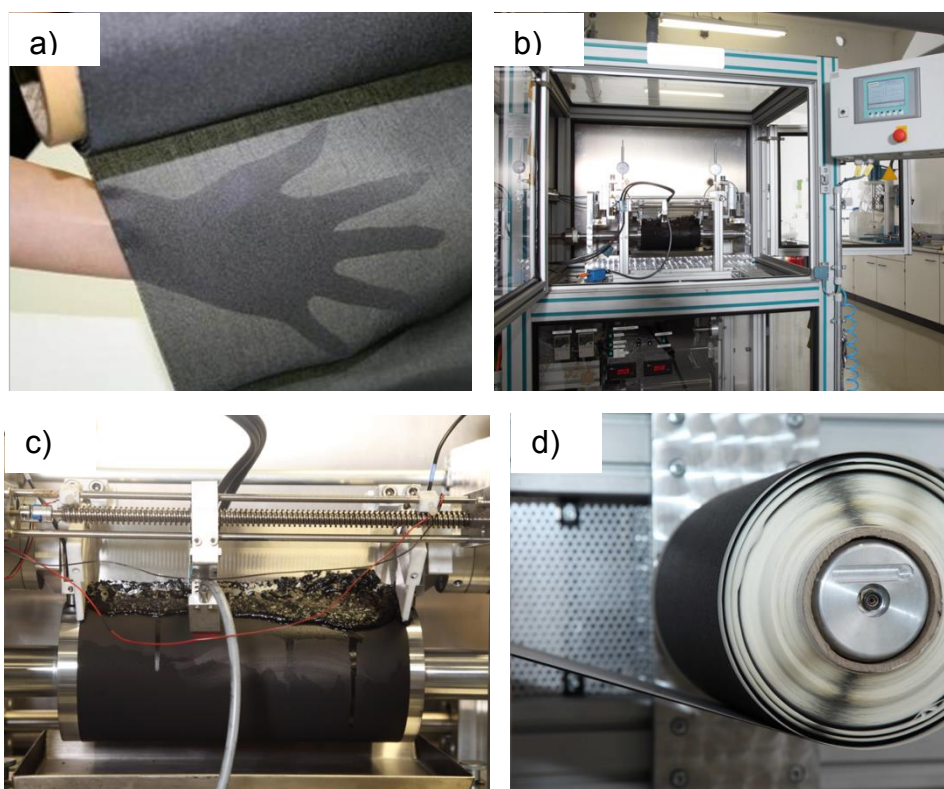


Figure 15: Preparation of the gas diffusion electrodes in a roll-to-roll production process at elcomax GmbH. a) Carbon cloth, b) applying of HSAC slurry, c) doctor blading of the HSAC slurry and d) final gas diffusion electrodes after drying. All pictures are provided by elcomax GmbH.

An optimised deposition of the nanocrystalline platinum cobalt catalysts supported on high surface area carbon (Pt-Co/C) was obtained by adjusting the composition of

the precursor solution, the reducing atmosphere, the temperature and the atomic ratio of platinum and cobalt salts as a function of each other, respectively. The impregnation solution was carefully drop-coated on previously fabricated gas diffusion electrode (GDE) sheets (see Figure 15), resulting in a platinum loading of 1.00 mg cm^{-2} [31]. The used GDEs were provided by elcomax GmbH and consisted of a doctor-bladed high surface area carbon layer on a wetproof, gas-permeable carbon-based cloth (Figure 15a).

In order to achieve an inexpensive and easy deposition of the catalysts, best results were obtained with an impregnation solution, having a Pt:Co ratio of 1:5. The solution contained hexachloroplatinic acid ($\text{H}_2\text{PtCl}_6 \cdot 6\text{H}_2\text{O}$), cobalt nitrate ($\text{Co}(\text{NO}_3)_2 \cdot 6\text{H}_2\text{O}$), ethylene glycol (EG) as reducing agent and 2-propanol/ultrapure water ($18.1 \text{ M}\Omega \text{ cm}$) in a ratio of 1:1 as solvent [31].

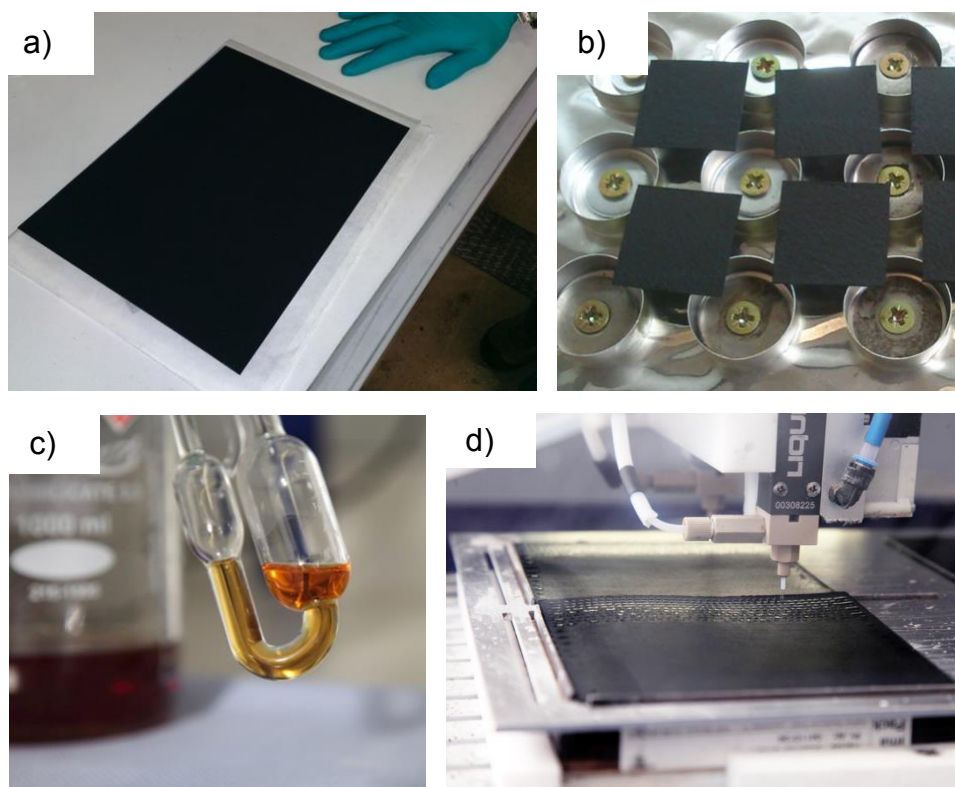


Figure 16: Preparation of the Pt-Co/C catalysts. a) GDE sheet, b) GDE pads for optimisation of the catalyst preparation, c) impregnation solution and d) impregnation of larger electrode sheets at elcomax GmbH. Figures c) and d) are provided by elcomax GmbH.

Furthermore, activity and stability enhancing treatment of the active catalyst layer includes the addition of the non-ionic surfactant Brij-30 to the precursor solution in order to prevent the nanoparticles from agglomeration during the reduction step, acid leaching and annealing steps after reduction [100]. The reduction of the deposited metal salts was initiated by a mild thermal treatment in nitrogen atmosphere [31]. Generally, the manufacturing process was restricted to temperatures below 300 °C due to the limited thermal stability of the HSAC layer of the GDEs.

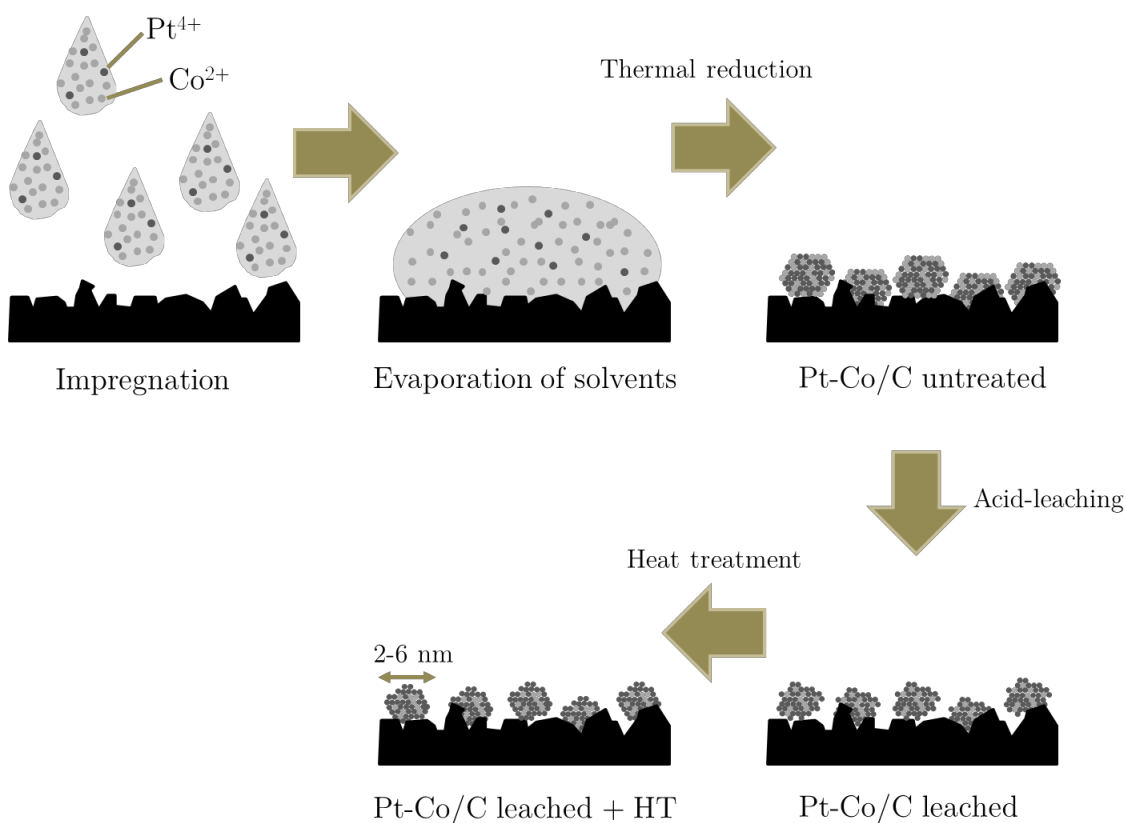


Figure 17: Schematic drawing of the nanoparticle synthesis.

Figure 17 depicts a schematic drawing of the above described Pt-Co/C nanoparticle synthesis. During impregnation it was taken care not to lose any of the impregnation solution by drop-coating over the edge of the GDEs or by wetting through the sheet. After impregnation of GDE pads/sheets the samples were pre-dried for 30 min at

100 °C to remove the solvents, leaving behind the platinum and cobalt precursor salts dissolved in the reducing agent EG. For larger GDE samples it was necessary to assure a uniform vaporisation of the excess solvents by manual distribution of the solution during the drying step. Afterwards the thermal reduction of the precursor salts was carried out at temperatures between 180 and 300 °C, whereby best results were obtained at 240 °C in nitrogen-saturated atmosphere for 10 min, resulting in Pt-Co/C nanoparticles. This untreated nanoparticles usually exhibited rather low activities towards oxygen reduction reaction and a poor stability, as will be discussed later. Therefore, post-preparation treatments were applied in order to increase the properties of the electrocatalysts towards ORR and long term stability. Firstly, the as-prepared catalysts were leached in 10 vol.% acidic solution of H₂SO₄ or HCl for 30 min to remove the inactive transition metal from the catalysts surface, leading to a so-called *Pt-skeleton surface* with a very high electrochemical active surface area (ECSA) [31,71,73,87,90]. And finally an additional heat treatment of the Pt-Co/C catalysts was used to decompose any undesired organic residues of the reducing agent and the surfactant, respectively, and to rearrange the positioning of Pt and Co within the catalysts [31,87,101]. Due to the lower surface energy of Pt, in comparison to the transition metal in inert atmosphere, platinum migrates to the catalysts surface, leading to a so-called *Pt-skin structure* [31,69,71,73,87,90,91]. Both processes, leaching and heat treatment, form a Pt overlayer at the surface of the Pt-Co catalysts and induce through *strain* and *ligand effects* a weakening of the binding of ORR intermediates at the Pt surface, hence leading to a higher activity towards ORR [31,69,71,73,87,90,91]. Furthermore, the Pt overlayer renders the Pt-Co catalysts kinetically more stable against dissolution of the solute transition metal under the acidic and oxidizing environment of the HT-PEM fuel cell cathode [31,71,90].

Consequently, during all steps of the Pt-Co/C electrocatalysts synthesis samples were taken and characterised by means of cyclic voltammetry (CV) in thin-film rotating disc electrode (RDE) measurements and X-ray diffraction measurements (XRD). The catalysts were also examined by transmission electron microscopy (TEM) before and after post-preparation treatments. The obtained results are discussed in the following chapters.

3.2 Structural and chemical analysis

In order to obtain information about the size of the catalysts particles as well as their distribution on the carbon electrode TEM measurements were performed. These measurements and the analysis thereof were executed by MSc. Christoph Heinzl as part of his PhD thesis under supervision of Prof. Christina Scheu at the Department of Chemistry of the Ludwig-Maximilians-University Munich. The high-resolution TEM images in Figure 18 were provided by Christoph Heinzl and show the crystalline catalysts Pt-Co nanoparticles on the turbostratic carbon electrode before leaching and heat treatment (a) and afterwards (b).

Usually, separated spherical nanoparticles which were randomly distributed across the HSAC were observed in TEM measurements. Before acid-leaching the Pt-Co/C catalyst particles possessed a mean size of 4.6 ± 1.1 nm with a minimum value of about 2.2 nm and a maximum of 7.3 nm in diameter. The average size of the nanoparticles after leaching was 4.5 ± 0.9 nm with a minimum value of about 2.4 nm and a maximum of 7.0 nm in diameter. In general, neither morphology nor size of the catalyst nanoparticles changed significantly during leaching and heat treatment [31].

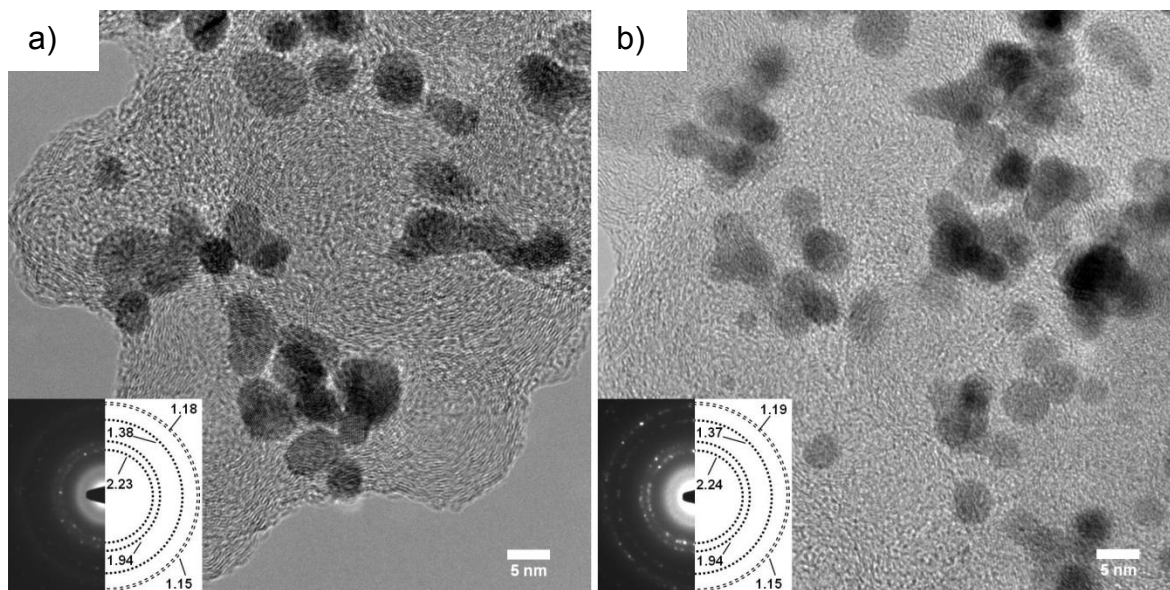


Figure 18: High-Resolution TEM images of the prepared Pt-Co/C catalysts before leaching and heat treatment (a) and afterwards (b). The insets show the electron diffraction patterns of the crystalline catalysts particles. The indicated d-values are given in Å. Both images have been published in Ref. [31].

Furthermore, electron diffraction measurements were performed in order to investigate the crystalline nature or crystal structure of the prepared metallic nanoparticles. The corresponding electron diffraction patterns are shown in the inserts of Figure 18 and reveal a quasi polycrystallinity of the prepared Pt-Co/C samples. The depicted diffraction rings were obtained by averaging over several randomly oriented platinum crystals. When comparing the measured d-values with literature values for cubic platinum [102] a maximum deviation of 1.3% can be detected after leaching. Neither cubic nor hexagonal diffraction intensities of crystalline cobalt were observed. Nevertheless, the presence of cobalt was verified via energy dispersive X-ray spectroscopy (EDX) measurements (Figure 19).

Therefore the X-ray spectrum was recorded over an area of several hundred nanometers in dimension. The atomic percentages of Pt and Co within the samples were determined using the *Cliff-Lorimer equation* for thin specimen [103]. For quantitative analysis of the Pt-Co/C samples the Pt L_{α} and Co K_{α} lines at 9.441 keV and 6.924 keV, respectively, were used.

The EDX spectra of the untreated and the leached Pt-Co/C electrocatalysts show only slight differences, see Figure 19. Both spectra show only EDX lines of carbon, oxygen, platinum, chloride, cobalt and nickel. The oxygen derives either from surface oxides of the metals or from surface oxidation of the HSAC support, or both. Nickel is detected due to the usage of holey carbon coated Ni grids as substrate for the TEM-EDX measurements.

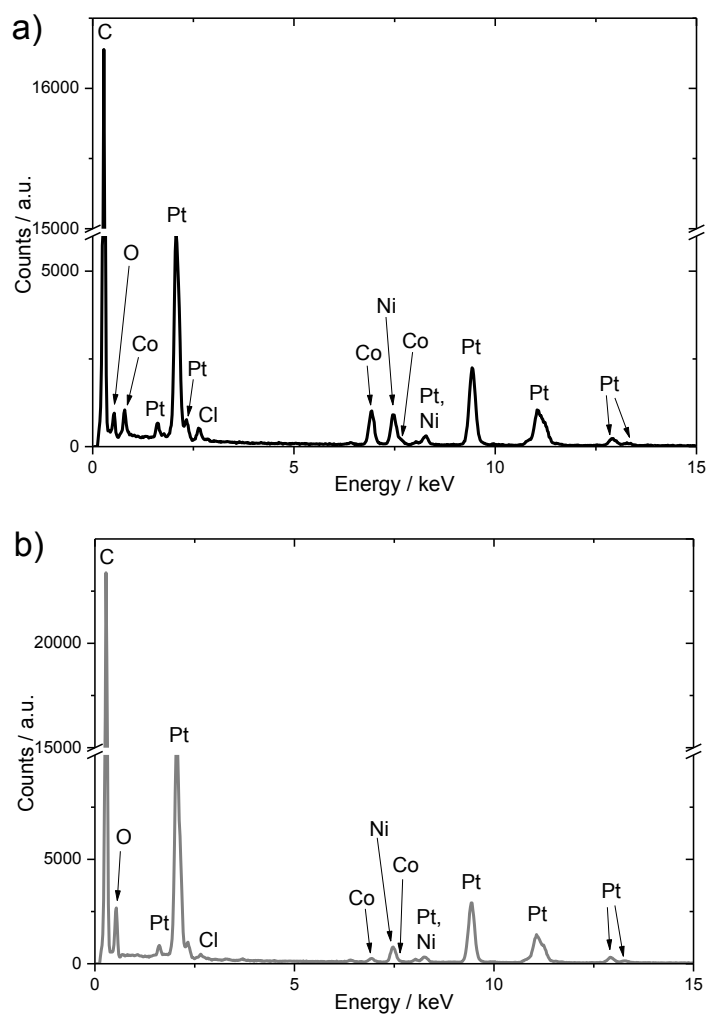


Figure 19: EDX spectra from Pt-Co/C catalyst samples before (a) and after leaching (b).

EDX measurements before leaching (Figure 19a) show a significant higher ratio of cobalt (28.0 ± 6.0 at.%) to platinum (72.0 ± 6.0 at.%). Whereas, the ratio of cobalt to platinum after leaching (Figure 19b) shows that the amount of platinum with

96.5 ± 1.3 at.% highly outweighs the contained amount of cobalt with 3.5 ± 1.3 at.%. The analysis of the elemental distribution within an individual nanoparticle was not successful due to the weak signal. Given this small quantity of cobalt, a supposed alloy of platinum and cobalt would result in only slightly modified lattice plane distances. Therefore, the detection of such an alloy regarding the experimental error could not be achieved via electron diffraction or high-resolution (HR-)TEM. The electron diffraction experiments before and after leaching show only intensities originating from crystalline cubic platinum. The deviation from literature d-values for platinum of 1.5% is in the same range for both Pt-Co/C samples and represented the measuring error. This finding and the fact that about 88% of the initial amount of cobalt is removed during the leaching process, led to the assumption that most of the cobalt on the electrode was present in amorphous state [31].

In order to obtain more information about the Pt-Co/C catalysts samples at different stages of production and for comparison issues a commercial obtained Pt/C sample from elcomax GmbH was further analysed using X-ray diffraction technique. X-ray diffraction is a powerful tool to gather information about the crystalline structure of metals, alloys and solid solutions. Representative XRD patterns of the untreated, the leached and the leached and heat treated Pt-Co/C samples as well as the Pt/C reference are given in Figure 20. The observed 2θ Bragg peaks at ca. 39.8° , 46.3° , 67.7° , 81.4° , 85.5° , 103.6° , 118.1° and 123.2° correspond to the face-centered cubic (fcc) reflections of Pt(111), Pt(200), Pt(220), Pt(311), Pt(222), Pt(400), Pt(331) and Pt(420), respectively [31,104].

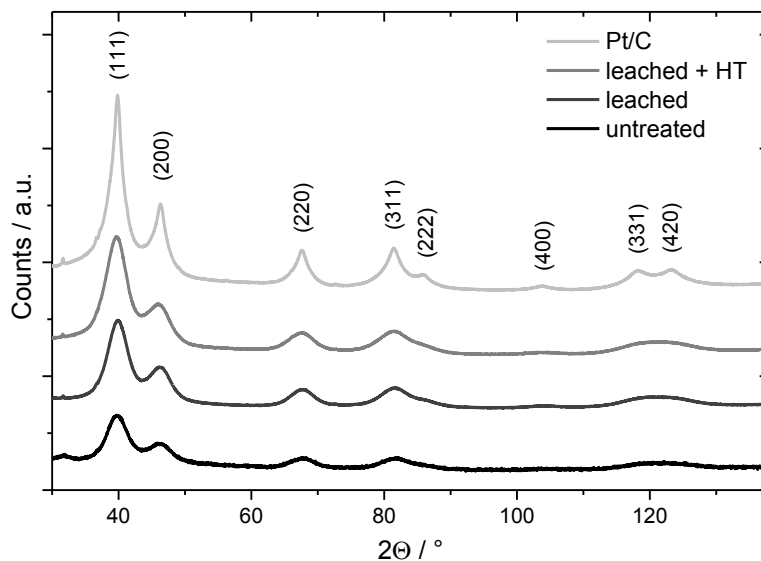


Figure 20: X-ray diffraction patterns of the untreated, leached, the leached and heat treated Pt-Co/C catalysts and the Pt/C catalysts [31].

Furthermore, the average particle size of the catalysts was determined by using the *Scherrer relationship* [105]. The obtained crystallite sizes of the Pt-Co/C catalysts were within a range of 2.6 - 2.9 nm, whereas the particle size of the Pt/C sample was 4.1 nm. The calculated crystallite sizes of the as-prepared Pt-Co/C catalysts are, in comparison, smaller than those determined from HR-TEM images. The reason for this small deviation is due to the fact that XRD and the *Scherrer relation* only provide the average size of the diffracting crystals rather than the particle size. According to the *Vegard's law* [106,107] the Co contents within the Pt-Co/C samples were calculated by comparing the lattice parameters (a) obtained from the measured 2θ Bragg peaks with those of the commercial Pt/C catalyst ($a = 0.39147(7)$ nm), metallic Pt ($a = 0.39231$ nm) [104] and metallic Co ($a = 0.35441$ nm), respectively [108]. The measured lattice parameter of the commercial Pt/C sample was in accordance with previously published values of around 0.39158 nm [106]. The lattice parameters of the nanocrystalline Pt-Co/C catalyst samples, the contents of Co in the Pt-Co/C catalysts and the crystallite sizes are given in Table 4.

Table 4: Summary of the properties of the differently treated Pt-Co/C catalysts and the commercial Pt/C catalyst obtained from XRD measurements. The amounts (at.%) of Co refer to lattice parameter of the Pt/C sample of 0.39147(7) nm and metallic Pt [104], respectively [31].

	a / nm	at.% Co a _{Pt/C} =0.39147(7) nm	at.% Co a _{Pt} =0.39231 nm	size / nm
Pt-Co/C untreated	0.39013(8)	3.6	5.9	2.9
Pt-Co/C leached	0.39079(8)	1.8	4.1	2.6
Pt-Co/C leached + HT	0.39060(7)	2.4	4.7	2.6
Pt/C	0.39147(7)	-	-	4.1

The atomic percentages (at.%) of Co refer either to the lattice parameter of the Pt/C sample of 0.39147(7) nm or to the lattice parameter of metallic Pt [104]. By using the lattice parameter of metallic Pt of 0.39231 nm [104] as reference for *Vegard's law*, the Co content of the Pt-Co solid solutions is increased by 2.3 at.%. In both cases, the results obtained from the XRD measurements are in accordance to the EDX analysis [31].

3.3 Ex-situ electrochemical studies

3.3.1 Measurement set-up and data treatment

All prepared catalyst samples were by default characterised at all stages during manufacture. Ex-situ electrochemical studies were the obvious choice to investigate the catalytic properties of the Pt-Co/C catalysts before testing them in fuel cells, as these experiments provide lots of useful information while being fast and simple at the same time.

The ex-situ electrochemical studies were carried out by using the thin-film method on a rotating disk electrode (RDE) in a standard electrochemical 3-electrode glass cell set-up (see Figure 21).



Figure 21: 3-electrode set-up for ex-situ electrochemical studies of the Pt-Co/C catalysts.

In order to prepare the RDE working electrode, 2 cm² of the prepared gas diffusion electrodes were immersed in 2-propanol and treated in an ultrasonic bath until a homogeneous dispersion of the Pt-Co/C catalysts was obtained. A sonication time of less than 30 min was sufficient, since too long sonication resulted in agglomeration of the carbon support material and an inhomogeneous dispersion [109].

A 10 μ l aliquot of the dispersion was then pipetted onto the glassy carbon disk of the working electrode tip without wetting the surrounding polytetrafluoroethylene (PTFE) part (Figure 22).

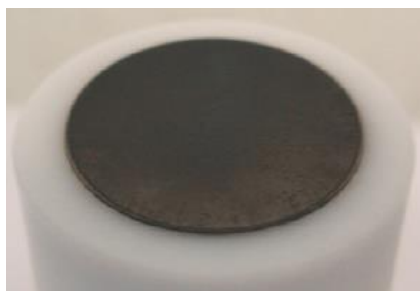


Figure 22: A homogeneous catalyst film after pipetting the catalyst dispersion onto the RDE tip. The image was provided by elcomax GmbH.

A clean preparation of the Pt-Co/C catalyst thin-film on the glassy carbon disc was rather difficult, due to the additives that were added to the HSAC slurry while preparing the GDE. The gas diffusion electrodes were produced for direct application in fuel cells and therefore needed hydrophobic additives. These PTFE additives in the carbon support materials made the usage of water in the catalyst dispersion impossible. Usually water is added to catalyst dispersions because it forms a defined droplet on the glassy carbon and does not wet the PTFE part of the electrode tip.

Since the quality of the catalyst thin-film on the glassy carbon is of crucial importance in order to obtain reliable and good quality measurements many an effort was devoted in the beginning of the thesis to find the most reliable method of depositing the as-prepared Pt-Co/C dispersion on the RDE tip. *Garsany* and co-workers demonstrated the thickness and homogeneity of the catalyst thin-film has negligible impact on cyclic voltammograms (CVs) in N_2 saturated electrolyte, however, both properties of the thin-film influence the O_2 diffusion and thus the oxygen reduction reaction (ORR) polarisation curves (see Figure 23). In general, the quality of the thin-film can be “controlled” by the usage of different alcohols as dispersion solvents, the content (e.g. addition of surfactants) of the solution, the quality of the catalyst dispersion itself, the temperature and humidity [110,111].

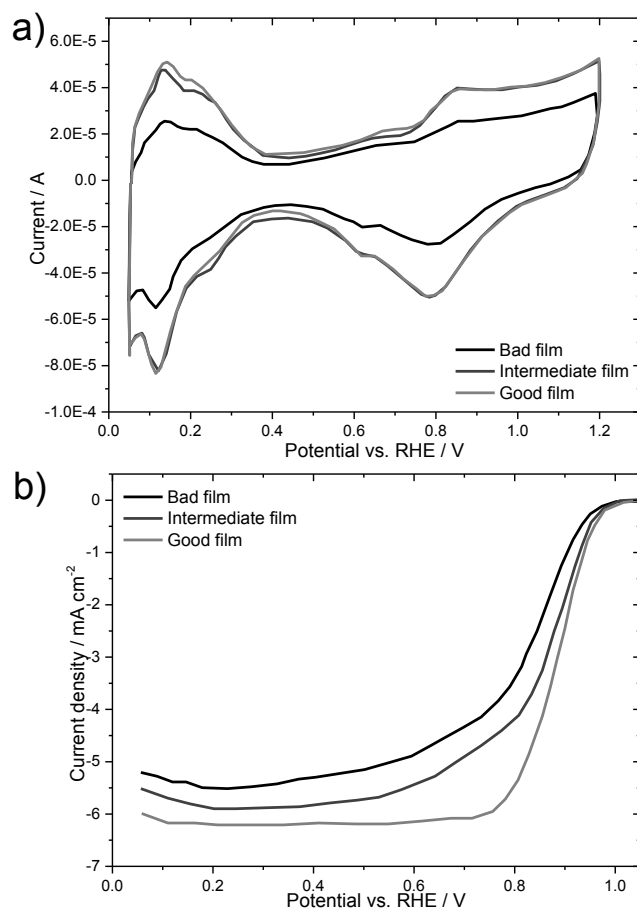


Figure 23: Effect of catalyst thin-film quality on cyclic voltammetry in inert electrolyte (a) and oxygen reduction reaction polarisation (b). Adapted from *Garsany et al.* [110].

As mentioned above a 10 μl aliquot of the prepared Pt-Co/C electrocatalyst dispersion was applied onto the glassy carbon disk. This was performed in two 5 μl portions. After the first application the thin-film of the catalyst dispersion was allowed to dry completely before applying the second portion. In many cases the deposition of the catalyst dispersion on the RDE tip, while rotating it at several hundred rpm is recommended [111]. In contrast, we had to use a stationary drying due to the lack of water in the Pt-Co/C dispersion. Nevertheless, this stationary two-step drying did not lead to a so-called "coffee-ring" appearance of the thin-film [111]. Due to the usage of pure 2-propanol as solvent for preparing the Pt-Co/C dispersion, the drying of the thin-film was faster and disabled the formation of carbon agglomerates on the GC disc. Furthermore, the catalyst dispersion contained

residues of the surfactant Brij-30 from the reduction step of the catalyst production, which stabilised the Pt-Co/C particles during the working electrode preparation. After realisation of the post-preparation treatments, like acid-leaching and heat treatment, it became more difficult to obtain homogeneous catalyst dispersions, hence to obtain good quality thin-films on the glassy carbon disc, due to removal of the organic residues in the catalyst film.

In order to obtain consistent and reliable values of the electrochemical active surface area (ECSA), the specific current density (SCD) and the mass activity (MA) of all raw data were corrected for the ohmic resistance of the used set-up and the real zero potential point ($0 V_{\text{RHE}}$) of the reversible hydrogen electrode (RHE). Therefore, $0 V_{\text{RHE}}$ was controlled subsequently after each measurement by performing the hydrogen evolution reaction on Pt in the same electrolyte which was used for the electrochemical ORR experiments. The internal resistance drop was determined by carrying out impedance spectroscopy with a peak-to-peak amplitude of 10 mV in the range from 100 kHz to 1 Hz. The ohmic drop was evaluated afterwards from the high frequency intercept point on the real axis of the Nyquist plot. Since all experiments were carried out at room temperature, typically the uncompensated resistance came to 25-30 Ω in 0.1 M HClO₄ [31].

The determination of the ECSA can be either done by integrating the area of the Pt-H oxidation peak in the H_{upd} area of a cyclic voltammogram (CV) in N₂ saturated electrolyte or by performing a so-called “carbon monoxide (CO)-stripping” and integrating the CO oxidation peak instead. Both methods offer advantages but also disadvantages. In both cases the obtained CV must be corrected by all currents related to the double layer formation on the working electrode surface. Calculating the ECSA from the H_{upd} area is fast since no additional experiments need to be performed. However, the results are only reliable for pure Pt catalysts. Since the coverage of adsorbed H* is dependent on surface structure and composition of the

catalyst particles, in general, the obtained ECSA for Pt alloy surfaces is lower due to its weaker interaction with reactant species in the electrolyte [92]. CO-stripping offers more accurate values of ECSA of Pt alloys, but as it involves the introduction of toxic carbon monoxide gas into the electrolyte, this experiment needs to be done with precaution and has more infrastructural requirements on the lab facility [92]. Considering the analysis of the ORR data of the anodic scan, it was necessary, besides correction for the ohmic drop and $0 V_{\text{RHE}}$, to deduct all currents which did not contribute to the oxygen reduction itself. Thus, the ORR polarisation curve was also corrected by the CV curve recorded in N_2 -saturated electrolyte. Figure 24 depicts the importance of these corrections on the evaluation of the specific current density (SCD) and the mass activity (MA). The dotted line at $0.9 V_{\text{RHE}}$ marks the potential at which both, the SCD and the MA, were calculated [112].

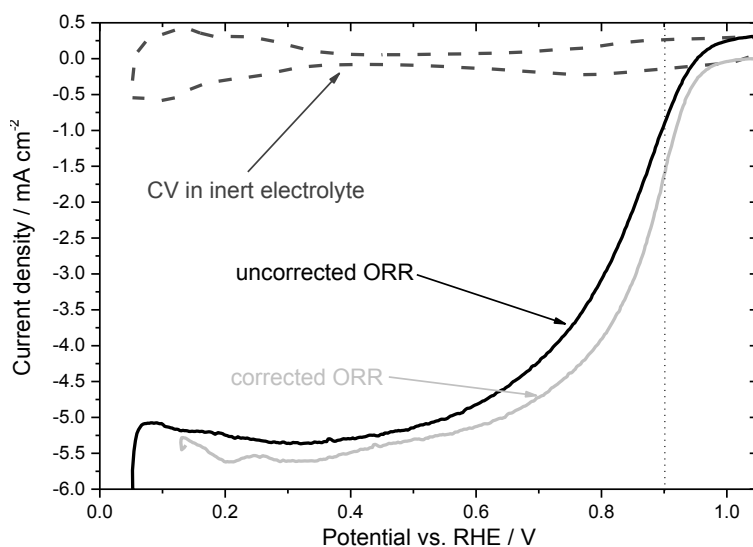


Figure 24: Influence of the applied corrections on the oxygen reduction reaction.

3.3.2 Catalytic activity and degradation tests

After having discussed the structural and chemical properties of the prepared catalysts, in “Structural and chemical analysis”, this chapter will focus on their electrochemical and catalytic characteristics. Therefore, the catalytic properties of the Pt-Co/C electrocatalysts during all different stages of production will be discussed in detail.

As mentioned before together with Christoph Grimmer many an effort was devoted to find the optimal impregnation solution and reduction method for implementing the Pt-Co/C catalyst system into a continuous membrane electrode assembly manufacturing. The experimental variations of the composition of the impregnation solution and the reduction and post-preparation treatment parameters are described in detail in the master thesis of Christoph Grimmer [99] and will not be further discussed in this thesis. As *Joseph Schumpeter* already said *innovation is an act of creative destruction* [113]. Further development of the production process and its changes to the synthesis set-up, which will be described in the following, made another investigation of the influence of all synthesis parameters, like the platinum and cobalt ratios, the temperature for the thermal reduction of the precursor salts, the acids for the leaching process and the temperature of the annealing step, on the activity and stability of the Pt-Co/C catalysts necessary.

The major changes in the synthesis set-up during this thesis involved the employment of a different high surface area carbon support material in the manufacturing of the gas diffusion electrodes. In Christoph Grimmer’s master thesis the GDEs had a HSAC loading of 4.2 mg cm^{-2} on the gas diffusion layer and consisted of crystalline carbon. During the progress of this thesis the HSAC loading as well as the type of carbon material was changed. The herein used GDEs had a

HSAC loading of 2.8 mg cm^{-2} and consisted of turbostratic carbon, a type of disordered graphite. Furthermore, the heat treatment, which was developed in preliminary work as part of the post-preparation treatment, was improved by applying a heating ramp instead of applying immediately the targeted temperature on the Pt-Co/C catalysts. In both cases, these changes did not affect activity and stability, or the composition of the impregnation solution and the optimum temperature for the thermal reduction of the metal salt precursors. Therefore the testing of these parameters will not be described further in this chapter.

3.3.2.1 Influence of post-preparation treatments

Directly after impregnation of the gas diffusion sheets and thermal initiated reduction of the Pt and Co precursor salts, the prepared Pt-Co catalysts (further termed “*untreated*”) showed the typical features of Pt based alloys in cyclic voltammetry experiments, including a H_{upd} region, a double layer and an oxide formation region, as can be seen in Figure 25. The H_{upd} region reflects the catalysts’ electrochemical active surface area (ECSA).

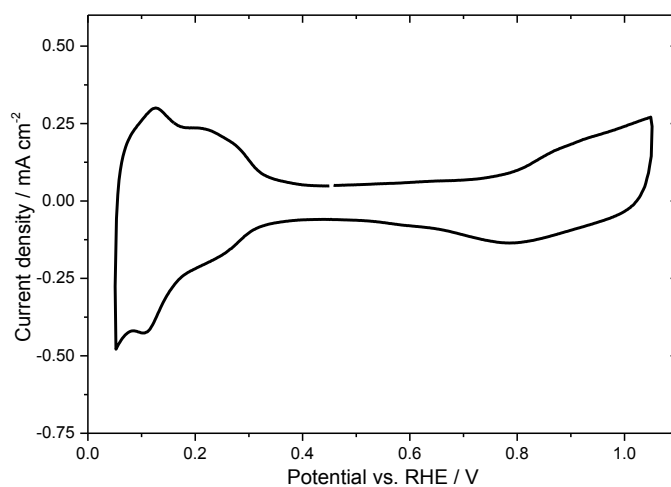


Figure 25: Cyclic voltammogram of the Pt-Co/C catalyst directly after reduction of the precursor metal salts.

However, the untreated Pt-Co/C electrocatalysts exhibited in fact very poor activities towards oxygen reduction reaction in comparison to the standard Pt/C reference sample (Figure 26). There is a huge difference of the ORR onset potential, the measured current at 0.9 V_{RHE} and the diffusion limited current between these two samples. The difference of the diffusion limited current might be due to slight variations of the catalysts film or the Pt-loading on the RDE working electrode tips. Nevertheless, the important factors for determining the SCD and the MA towards ORR are differences of the kinetic properties of the catalysts, which are not influenced by the Pt-loading. This can especially be seen in the mass transport corrected Tafel plots in Figure 26b. Clearly, the Pt/C reference exhibited a higher kinetic current density at 0.9 V_{RHE} than the untreated Pt-Co/C catalyst.

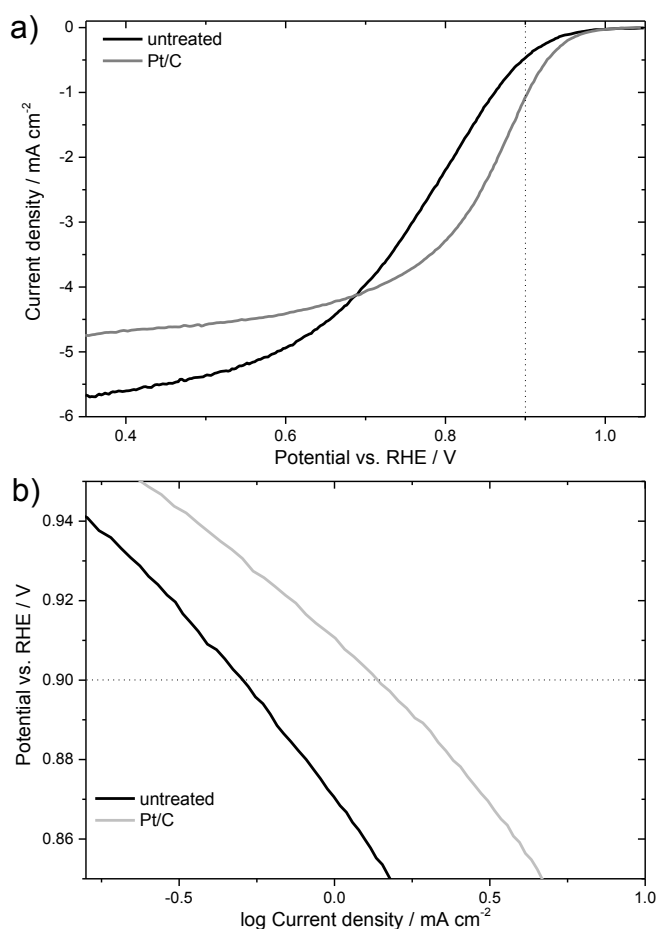


Figure 26: ORR polarisation curves and corresponding Tafel plots of the untreated Pt-Co/C and the commercial Pt/C catalyst recorded at a scan rate of 50 mV s⁻¹ in 0.1 M HClO₄ electrolyte.

Due to the highly acidic and oxidising environment of a HT-PEMFC cathode, Pt-M catalysts are prone to gradual degradation, which limits the lifetime of the PEMFC significantly. Especially high potentials (> 1.2 V) lead to the corrosion of the carbon support material, the detachment of the Pt nanoparticles, their agglomeration and/or loss of electrical contact [71]. In order to determine the stability and durability of the as-prepared Pt-Co/C catalyst samples accelerated stress tests (ASTs) were conducted. For this purpose, the electrodes were cycled 1665 times between 0.5 and 1.4 V_{RHE} in deaerated 0.1 M HClO_4 at a scan rate of 500 mV s^{-1} . Every 555th cycle the ECSA was determined. The loss of ECSA gives information on the stability of the synthesised Pt-Co electrocatalysts [31].

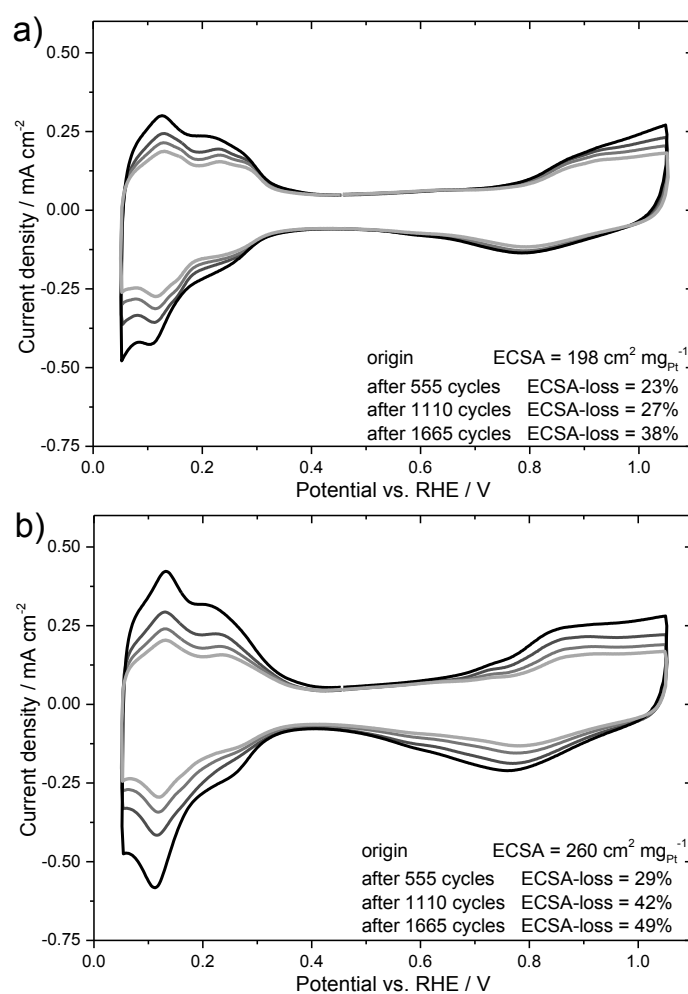


Figure 27: Cyclic voltammograms of the untreated Pt-Co/C catalyst (a), and the Pt/C catalyst (b) recorded at a scan rate of 50 mV s^{-1} in nitrogen saturated 0.1 M HClO_4 electrolyte. The gradual degradation of the catalysts during AST cycling is given after 555, 1110 and 1665 cycles in form of the loss of ECSA [31].

While the kinetic properties of the untreated Pt-Co/C catalyst were disappointing, their stability during accelerated stress test was superior to that of the Pt/C reference catalyst. After 1665 cycles between 0.5 and 1.4 V_{RHE} the loss of electrochemical active surface area of the untreated Pt-Co/C catalyst was limited to 38%, whereas the degradation of the ECSA of the reference catalyst was 49% (see Figure 27).

In order to improve the sluggish performance of the untreated Pt-Co/C catalysts, the catalysts were leached in acidic solutions to remove the inactive material from the catalyst surface. This was done by immersing the untreated Pt-Co/C catalyst GDE sheets in 10 vol.% sulphuric acid in water/2-propanol 1:1 for 30 min and washing them afterwards in water/2-propanol 1:1.

As can be seen, this leaching process resulted in an increased ECSA in comparison to the untreated Pt-Co/C catalysts.

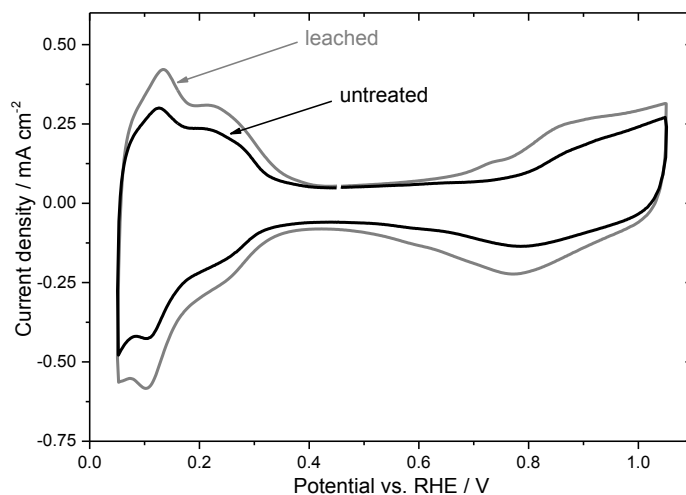


Figure 28: Comparison of the cyclic voltammograms of the untreated and the leached Pt-Co/C catalysts recorded at a scan rate of 50 mV s⁻¹ in nitrogen saturated 0.1 M HClO₄ electrolyte.

In general, this leaching treatment improved the overall performance of the Pt-Co/C catalysts in comparison to the untreated Pt-Co/C and the Pt/C reference catalyst, respectively. This positive effect of acid-leaching on the performance of the prepared

Pt-transition metal catalysts in comparison to the Pt/C catalyst is ascribed to the dissolution of the inactive transition metal components and the segregation of Pt at the surface of the catalysts, resulting in a roughening of the surface and leaving behind a Pt-skeleton structure with a negligible amount of the solute metal [71,73,87,90]. This roughening can be seen by the area under the H_{upd} peak in Figure 28, which was increased by 30% due to the removal of the inactive Co from the catalyst surface (see also chapter “Structural and chemical analysis”). Furthermore, treating the carbon supported Pt-Co catalysts in 10 vol.% H_2SO_4 for 30 min led to a 1.7-fold increase of the specific current density (SCD) and a 1.6-fold increase of the mass activity (MA) in comparison to the Pt/C sample (Figure 29) [31].

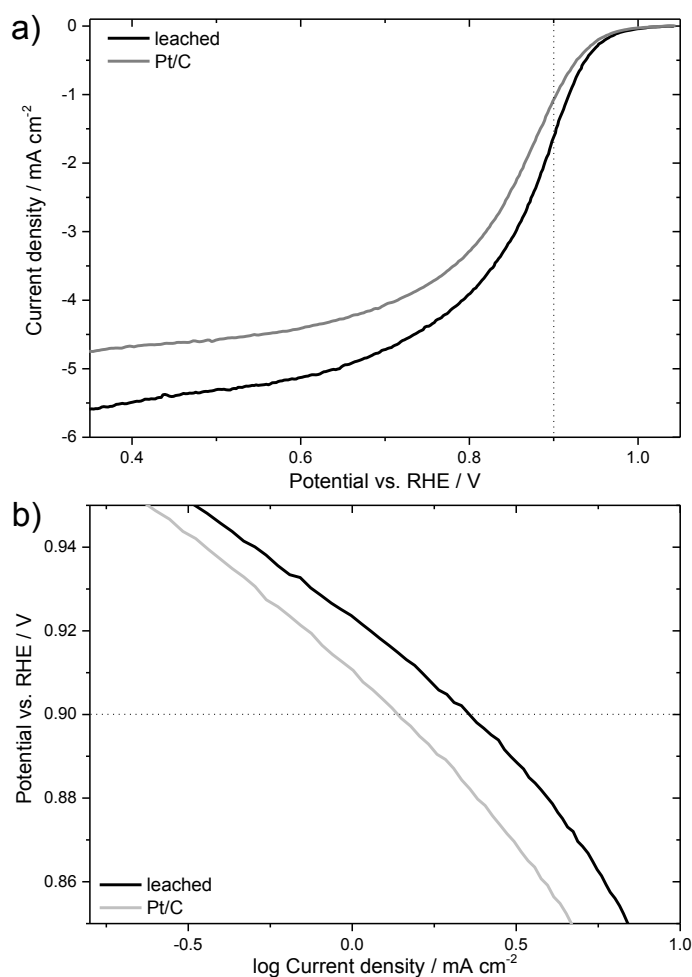


Figure 29 ORR polarisation curves and corresponding Tafel plots of the leached Pt-Co/C and the commercial Pt/C catalyst recorded at a scan rate of 50 mV s⁻¹ in 0.1 M $HClO_4$ electrolyte.

The Pt overlayer, which is formed due to the segregation of the Pt to the surface of the catalyst during the leaching process, is considered to render the Pt-Co/C catalysts kinetically more stable against dissolution of the solute transition metal under the acidic and oxidising environment of the HT-PEM fuel cell cathode [31,71,90]. This can be clearly seen in Figure 30.

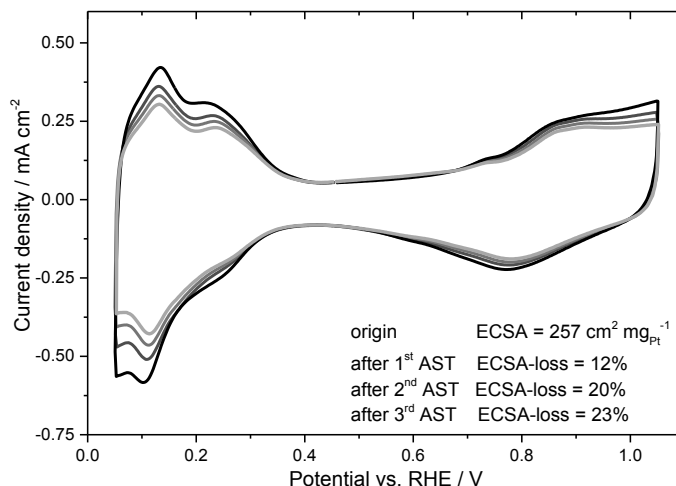


Figure 30: Cyclic voltammogram of the leached Pt-Co/C catalyst recorded at a scan rate of 50 mV s⁻¹ in nitrogen saturated 0.1 M HClO₄ electrolyte. The gradual degradation of the catalyst during AST cycling is given after 555, 1110 and 1665 cycles in form of the loss of ECSA [31]

Although the untreated Pt-Co/C catalysts already exhibited an improvement in terms of stability over the Pt/C reference catalyst, the leaching process led to further advances in durability of the Pt-Co/C catalysts. The leached Pt-Co/C catalysts showed only a degradation of 23% after 1665 AST cycles, which was an improvement of 60% and 113% over the untreated Pt-Co/C catalyst and the Pt/C reference, respectively.

In literature, usually Pt-Co/C catalysts with a Pt₃Co structure exhibit a 2-fold improvement over Pt/C catalysts in terms of MA. Pt_xCo/C catalyst with a much lower content of Co also showed this activity improvement [87]. Since the prepared leached Pt-Co/C catalysts yielded a MA increase slightly lower than the reported average value, a second post-preparation treatment, a heat treatment, was

performed. Typically, reported annealing steps for carbon supported Pt-M catalysts were executed at temperatures above 450 °C in inert or reducing atmosphere or in vacuum [69,71,87,90]. This thermal treatment was used to obtain a higher degree of alloying within the catalysts, hence a further improvement of the initial ORR activity. In contrast to this previously reported procedures a mild heat treatment at 220 °C in nitrogen atmosphere was performed within this work, due to the lack of thermal stability of the Pt-Co/C based gas diffusion electrodes [31,101,114]. The applied heat treatment step was initiated with a temperature ramp of 5 °C min⁻¹ starting at 30 °C. The final temperature of 220 °C was held for 45 min; afterwards the catalyst samples were removed from the oven and cooled down to room temperature immediately [31].

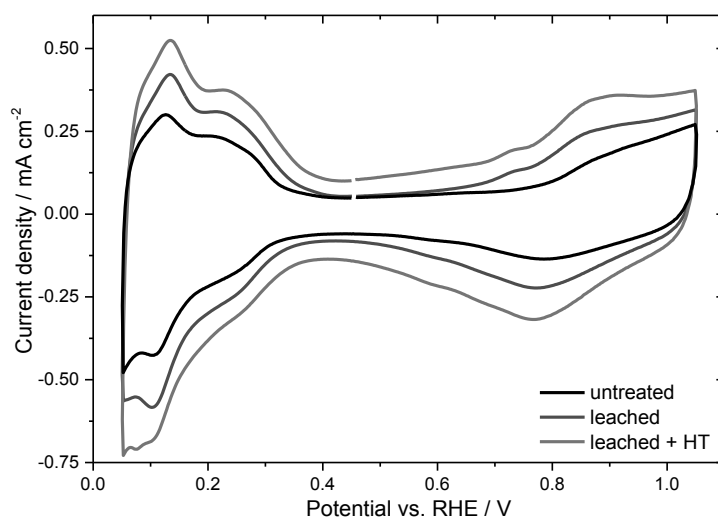


Figure 31: Cyclic voltammograms of the as-prepared Pt-Co/C catalysts recorded at a scan rate of 50 mV s⁻¹ in nitrogen saturated 0.1 M HClO₄ electrolyte [31].

The cyclic voltammograms (CVs) in Figure 31 reveal that the catalysts possess a higher ECSA after post-preparation treatment. As discussed above, the increase in ECSA is mainly due to the dissolution of the electrocatalytic inactive Co at the catalysts surface by applying an acid-leaching process. Furthermore, the heat treatment of the Pt-Co/C catalysts led to the removal of ethylene glycol, its decomposition products and the non-ionic surfactant from the catalysts surface. The

ECSA was increased by 56% and 21% in comparison to the untreated and to the leached Pt-Co/C catalysts, respectively. One would actually anticipate a decrease of ECSA during heat treatment due to Ostwald ripening at elevated temperatures, but using rather low temperatures, the cleaning of the catalysts surface from organic residues showed a higher impact on the active surface area than the increase of the mean particle size [101,114]. However, since the annealing step is part of a continuous process, oxygen impurities in the N₂ atmosphere are almost unavoidable. Thus, the CV of the leached and heat treated catalyst exhibits an increased double layer capacitance compared to the other catalyst samples due to partial surface oxidation of the HSAC [31].

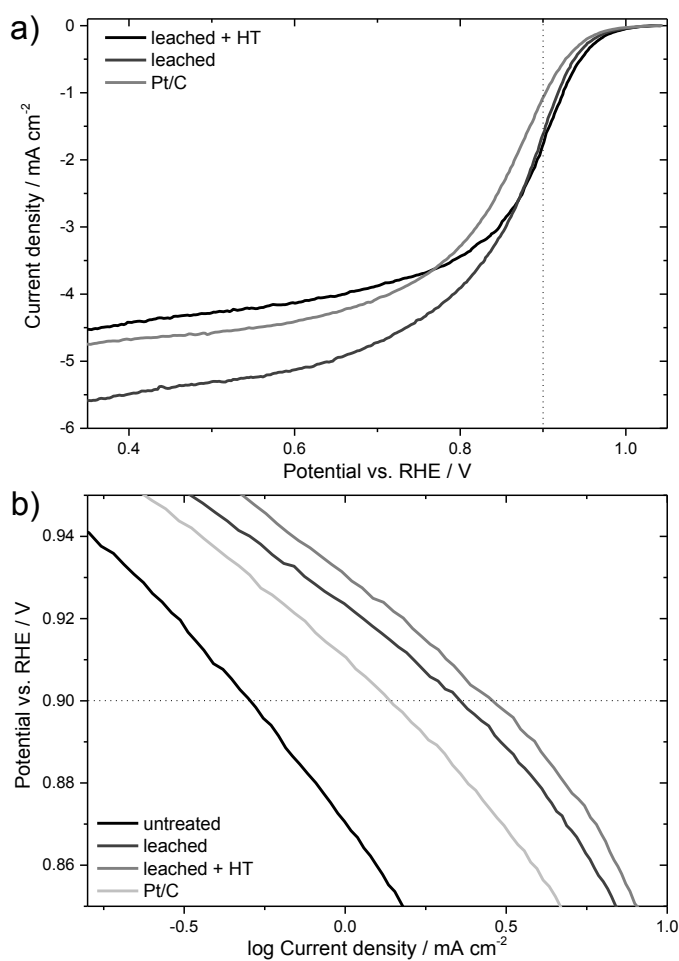


Figure 32: (a) Comparison of the ORR polarisation curves of the as-prepared Pt-Co/C catalysts and the Pt/C catalyst, recorded at a scan rate of 50 mV s⁻¹ in oxygen saturated 0.1 M HClO₄ electrolyte with a rotation speed of 1600 rpm. (b) Corresponding Tafel plots [31].

Figure 32 depicts the beneficial effects of the performed post-preparation treatments on the electrocatalytic properties of the Pt-Co/C catalyst. Figure 32a shows the ORR polarisation curves of the leached, the leached and heat treated Pt-Co/C catalyst and the Pt/C catalyst. Clearly, the leached and heat treated Pt-Co/C catalyst shows a more positive onset potential than the Pt/C catalyst and a higher current in the mixed-kinetic-diffusion region. The difference between the leached and the leached and heat treated Pt-Co/C catalysts is rather small, but the improvement can be seen more clearly in the Tafel plots in Figure 32b, where the kinetic current density at 0.9 V_{RHE} of all catalysts is compared. The additional heat treatment induced the desired further increase of the MA of the catalysts toward ORR in comparison to the leached samples, resulting in a 2-fold activity improvement over the Pt/C catalyst, whereas, the SCD was not affected.

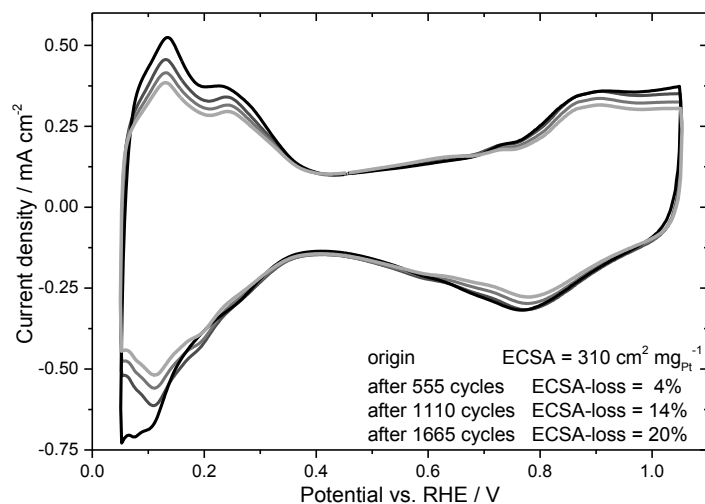


Figure 33: Cyclic voltammograms of the leached and heat treated Pt-Co/C catalyst recorded at a scan rate of 50 mV s⁻¹ in nitrogen saturated 0.1 M HClO₄ electrolyte. The gradual degradation of the catalysts during AST cycling is given after 555, 1110 and 1665 cycles in form of the loss of ECSA [31].

By treating the prepared Pt-Co/C catalysts according to the post-preparation procedures mentioned above, the initial ECSA as well as the stability are increased significantly (see Figure 33). In comparison to the untreated Pt-Co/C catalysts the leaching and heat treatment led to a stability increase of 90%, whereas a 2.5-fold

stability improvement over the Pt/C reference catalyst sample was obtained. In accordance to the results obtained from XRD and TEM analysis and due to the increased ECSA after leaching and heat treatment, this increase of stability cannot be attributed to an enlargement of the average particle size. We support the speculation of *Stephens et al.* that the annealing procedure smoothed out the surface of the catalysts and/or removes defects of undercoordinated sites, which are most susceptible to corrosion [31,71].

3.4 In-situ electrochemical studies

To enhance the knowledge of the interactions of the as-prepared leached and heat treated Pt-Co/C catalyst with other components inside an HT-PEM MEA, e.g. phosphoric acid, HT-PEM single cell and stack tests were carried out. Furthermore, the operation in fuel cells should give information on the performance of the synthesised nanoparticles and their long term stability towards corrosion and/or de-alloying [31].

In order to compare the results and the performance of the Pt-Co/C based HT-MEA a reference HT-PEM MEA based on pure Pt, which was also obtained from elcomax GmbH, was tested with the same experimental protocols.

3.4.1 Preparation of the PBI membrane

For the manufacturing of the HT-PEM membrane electrode assemblies (MEAs) membranes based on the basic polymer polybenzimidazole (PBI) were fabricated.

Therefore meta-PBI powder was dissolved in dimethylacetamide (N,N-DMAc) under stirring for 3 h at 200 °C under a pressure of 6 bar. The membranes were casted from this solution by solvent evaporation at a temperature range of 70-100 °C on a carrier foil. Afterwards, a thermal treatment of the membranes at 250 °C for 20 min was performed to remove DMAc residues [31].

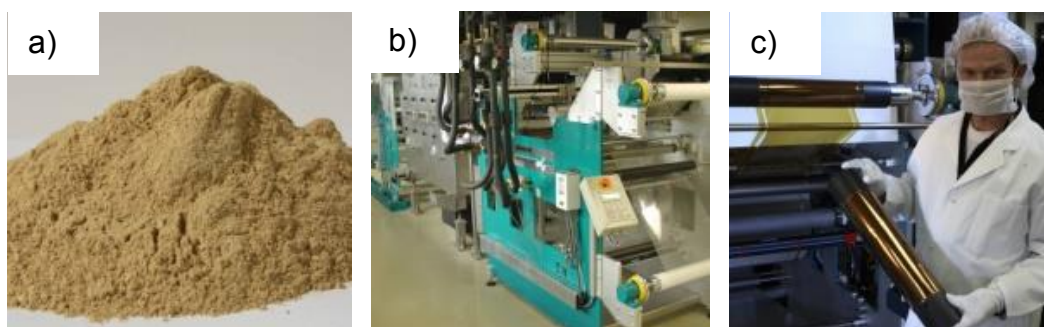


Figure 34: Membrane fabrication: a) m-PBI powder, b) casting machine and c) final membrane. Pictures were provided by elcomax GmbH.

3.4.2 Preparation of the membrane electrode assembly

After the deposition of the cathode catalysts on the gas diffusion electrode (GDE) sheets as described in “Catalyst preparation”, the HT-PEM membrane electrode assemblies (MEAs) were manufactured by doping the anode and cathode catalyst layers with 25 mg cm⁻² of a mixture of 85 wt.% phosphoric acid and 1-pentanol. After evaporation of 1-pentanol at 230 °C, the electrodes were hot pressed with a membrane based on polybenzimidazole (PBI) at 150 °C to form the membrane electrode assembly. For the anode a standard Pt based GDE from elcomax GmbH with a Pt-loading of 0.8 mg cm⁻² was used.

In order to compare the results and the performance of the Pt-Co/C based HT-MEA a reference HT-PEM MEA, which had an equal anode Pt-loading, but the cathode

Pt-loading was 20% (1.2 mg cm^{-2} instead of 1.0 mg cm^{-2}) higher than that of the Pt-Co/C based MEA, was tested with the same experimental protocols.

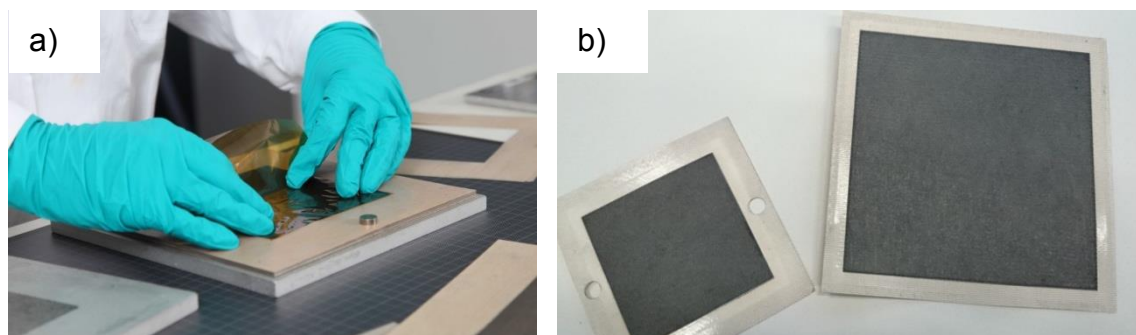


Figure 35: a) Manual assembling of the MEA, placing the membrane on the anode catalyst layer, b) final MEAs in different sizes, small for single cell measurements only, big for single cell and stack test. Pictures were provided by elcomax GmbH.

Figure 35a shows how the membrane electrode assembly is manually assembled before applying the hot pressing procedure. The final HT-MEA can be seen in Figure 35b. Due to the flexible gas diffusion electrode and catalyst preparation different sizes of MEAs are easily achieved. Usually the smaller sizes (50 cm^2) are used for single cell testing, whereas the larger MEAs (153 cm^2) are used for single cell tests as well as stack tests.

Prior to electrochemical in-situ testing of the Pt-Co/C catalysts, every membrane electrode assembly was controlled to be gastight. Therefore, on one electrode side, either the anode or the cathode, a pressure of 50 mbar was applied. On the other electrode pressure-sensitive sensors detected the pressure. If this pressure was higher than 2-3 mbar, the HT-MEA was rejected for further testing.

3.4.3 Measurement set-up and data treatment

As mentioned above three different experimental set-ups have been used for in-situ HT-PEM fuel cell testing of the Pt-Co/C catalysts. These three set-ups

differed in the size of the active area of the membrane electrode assembly and in the employed flow field channel structure. The first set-up was a single cell set-up with an active area of 50 cm² and a serpentine channel flow field structure on anode and cathode sides (see Figure 36).

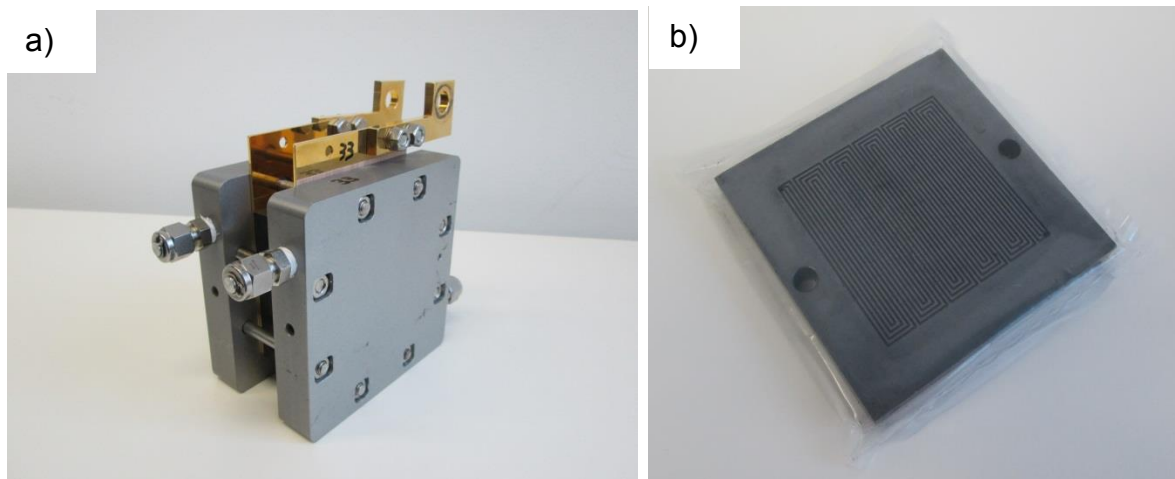


Figure 36: Small HT-PEM fuel cell set-up: a) assembled fuel cell, b) serpentine flow field. Pictures were provided by elcomax GmbH.

The second HT-PEM set-up was also a single cell set-up but having an active area of 153 cm² and a parallel channel flow field structure on anode and cathode sides, which was operated in cross-flow.

The last HT-PEM fuel cell measurement set-up, which was used for in-situ characterisation and catalyst testing, was a stack set-up (Figure 37). The fuel cell stack consisted of 20 cells, each with an active area of 153 cm². The flow field structure of the stack was the same as for the large HT-PEM single cell set-up.

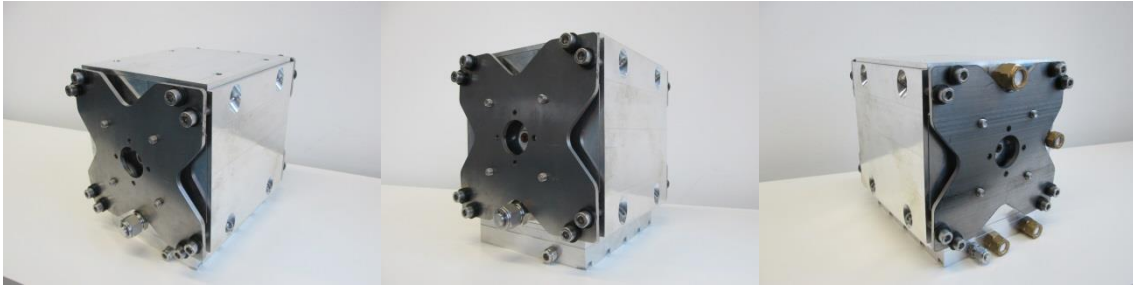


Figure 37: HT-PEM fuel cell stack from elcomax GmbH photographed from different angles and perspectives. Pictures were provided by elcomax GmbH.

After the hot-pressing procedure and passing the gas-tightness test all membrane electrode assemblies were subjected to a begin-of-life (BoL) characterisation. This BoL consisted of recording of the current-voltage characteristics (VI- or polarisation curve), of the power density and of the electrochemical impedance (EIS) characteristics.

For all measurements the reactant (hydrogen H_2 , synthetic reformat and oxygen O_2) flow rates were measured and controlled using mass flow controllers. The stoichiometries were kept constant at 1.2 for hydrogen (3.0) or synthetic reformat (76.0% H_2 , 1.2% CO and 22.8% CO_2) and 2.0 for air, respectively. The operational cell temperature was controlled by electrical heating cartridges and set to 160 °C [31].

Cyclic voltammograms were recorded feeding the MEAs with dry hydrogen on the anode (which was also used as pseudo-reference electrode) and humidified nitrogen on the cathode. The ECSA was determined by cycling the cathode between 0.095 and 1.100 V with 100 $mV s^{-1}$ 100 times, followed by an analysis scan with 50 $mV s^{-1}$. Electrochemical impedance spectra (EIS) were recorded in a pseudo-galvanostatic mode with a Zahner power potentiostat (PP241) and fuelling the anode with synthetic reformat. Afterwards equivalent circuit (EC) analysis was performed to quantify the different losses occurring in the as-prepared HT-PEM MEA.

After BoL characterisation a long term operation under constant load was conducted at a current density of 0.2 A cm^{-2} . The HT-PEM fuel cell was supplied with hydrogen on the anode and air at the cathode.

3.4.4 HT-PEM single cell measurements

3.4.4.1 Polarisation and power density

After manufacturing, the MEA was characterised by investigation of polarisation, power density and electrochemical impedance properties, using hydrogen and synthetic reformat as anode feedstock, respectively [31].

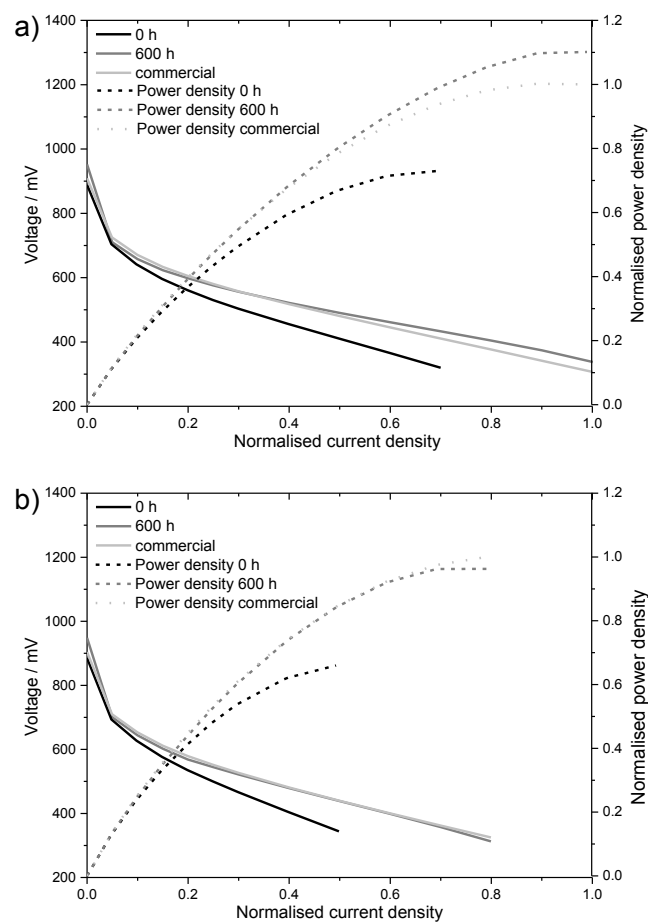


Figure 38: Polarisation curves and power densities of the leached and heat treated Pt-Co/C based HT-PEM MEA before and after 600 h long term operation and the commercial HT-PEM MEA under constant load of 0.2 A cm^{-2} at $160 \text{ }^\circ\text{C}$, fuelled with hydrogen (a) and synthetic reformat (b) at the anode and air at the cathode [31].

In Figure 38 the polarisation of the leached and heat treated Pt-Co/C based MEA and the commercial Pt/C based HT-PEM MEA are shown. The first polarisation curve of the leached and heat treated Pt-Co/C based MEA was recorded immediately after the MEA hot pressing step; the second was taken after 600 h long term operation under constant load of 0.2 A cm^{-1} at $160 \text{ }^\circ\text{C}$ [31].

In both cases, applying pure hydrogen and synthetic reformat at the anode, the performance of the in-house prepared HT-PEM MEA was enhanced during operation. The open cell voltage (OCV) value as well as the ohmic resistance improved during the long term test. Contrary, the polarisation and power density of the commercial Pt/C MEA showed no change during the 600 h long term operation. While being fuelled with hydrogen, the in-house prepared Pt-Co/C based HT-PEM MEA, having approximately a 20% lower Pt loading at the cathode, shows an enhanced performance over the commercial MEA after 600 h of operation, especially at higher current densities (Figure 38a). However, when fed with synthetic reformat on the anode, the performance improvements are diminished and both MEAs exhibit an equal performance (Figure 38b) [31].

3.4.4.2 Long term operation under constant load

As mentioned above, the Pt-Co/C based HT-PEM membrane electrode assembly was subject to a long term fuel cell operation at 0.2 A cm^{-2} at an operating temperature of $160 \text{ }^\circ\text{C}$. The fuel cell was supplied with pure hydrogen at the anode and air at the cathode.

Figure 39 shows the cell voltages and the 1kHz AC resistance of the Pt-Co/C based HT-PEM MEA and the commercial Pt/C based HT-PEM MEA during the 600 h long term single cell testing.

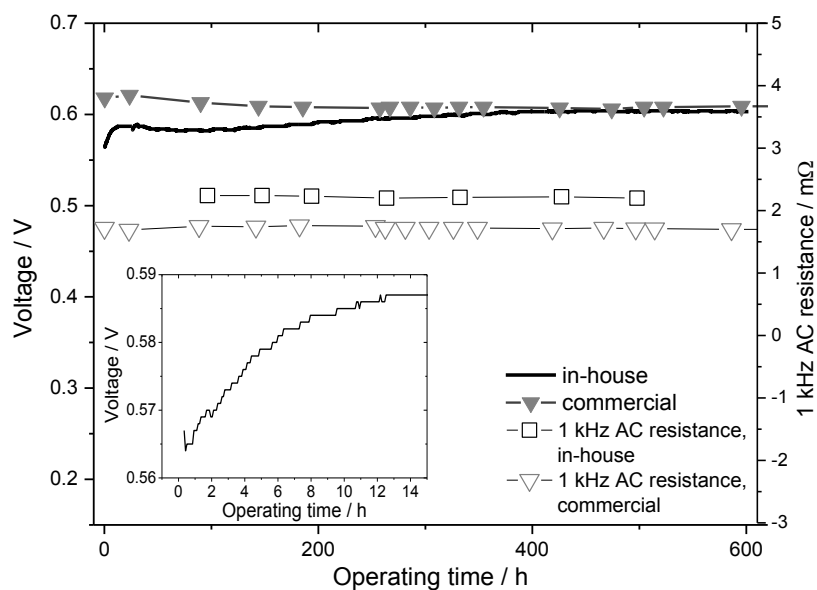


Figure 39: Comparison of cell voltages and the corresponding 1 kHz AC resistances of the leached and heat treated Pt-Co/C based HT-PEM MEA and a commercial HT-PEM MEA during durability testing at 160 °C. The insert shows the first 14 h of the long term operation of the in-house prepared MEA [31].

In general, the prepared Pt-Co/C based MEA demonstrated a very good durability in single cell operation. The average degradation rate of the leached and heat treated Pt-Co/C based HT-PEM MEA during the 600 h test under steady state conditions at 160 °C was $0 \mu\text{V h}^{-1}$. However, the MEA showed a voltage increase of more than 30 mV during the progress of operation. This increase corresponds to a cell voltage increase of $80 \mu\text{V h}^{-1}$. Especially during the first 14 hours of long term operation a very steep increase in cell voltage was observed, followed by a constant increase up to 500 h runtime. This long conditioning process is assigned to a redistribution of electrolyte within the catalyst layers. Afterwards, the cell voltage stabilised at a value of 604 mV [31].

In contrast, the commercial Pt/C based HT-PEM MEA, which resembles the state-of-the-art membrane electrode assembly of elcomax GmbH, showed a better performance at the beginning of the durability test, but lost cell voltage continually over the first 400 h of operation. Afterwards the cell voltage stabilised at 608 mV.

The 1 kHz AC resistances of both MEAs were at a constant value of 2.4 mΩ for the leached and heat treated Pt-Co/C based HT-PEM MEA and 1.7 mΩ for the

commercial one, respectively. Both values indicate a good distribution and retention of H_3PO_4 electrolyte within the catalyst layer of the cathode electrode [31].

By comparison, both MEAs showed an equal performance during 600 h of operation under constant load, although the commercial HT-PEM MEA had 20% more Pt at the cathode. Therefore, the results of the durability test confirm the higher activity of the as-prepared leached and heat treated Pt-Co/C catalyst compared to the commercial Pt/C catalyst, as observed in ex-situ analysis, due to the equal performance while having less Pt [31].

3.4.4.3 Electrochemical impedance spectroscopy

In order to investigate the electrochemical changes and losses within the cathode catalyst layer, which might have occurred during long term operation, electrochemical impedance spectroscopy (EIS) was performed.

EIS is a commonly applied tool in electrochemistry to investigate corrosion processes and to quantify losses occurring in electrochemical devices, such as batteries. In fuel cell research it is a reliable method, providing information on catalyst and membrane materials [115]. In general, the information on the catalyst and membrane materials derives either from a process model based on physicochemical relations, kinetics, mechanisms and consequently analytic equations or from a measurement model by means of equivalent circuit (EC) analogues. Both evaluation approaches offer advantages, but have insufficiencies as well. For example a good numerical complex nonlinear least square fit of a measurement model to experimental data does not necessarily mean the correct EC is applied. On the other hand a process model approach is often too complex to be applied on multipart systems like fuel cells. *Rezaei Niya et al.* gives a very concise comparison of these two approaches with respect to fuel cell applications [116] and *Macdonald* makes a very detailed distinction between models and analogues [117]. Due to the increasing complexity of

process models with the increasing number of components in a fuel cell a measurement model based analysis is the more straight-forward approach for the herein presented HT-PEMFC investigation. Although the physical meaning of the applied EC elements may be under discussion, at least correlations can be drawn between the described equivalent circuit and the analysis as follows [31].

Herein, equivalent circuit analysis was performed by Stephan Weinberger, due to his extraordinary expertise within this field of science, and used to simulate the entire frequency range of the given impedance spectra. Therefore, electric components, such as resistors and capacitors, were used for the simulation and fitting process (see Table 5 and Table 6). The applied EC (Figure 40) is based on the modified Randles cell equivalent circuit suggested by *Zhang et al.* [46] and its further modification as described in reference [118].

Table 5: Common electrical elements in EC analysis and their corresponding impedances [119]





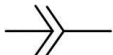

Element	Impedance Z	Symbol
Resistance	R	
inductor	$j\omega L$	
Capacitor	$\frac{1}{j\omega C}$	

Table 6: Electrical elements for electrochemical impedance spectroscopy and their description [119]

Element	Impedance Z	Symbol	Description
Resistance (Faraday Impedance)	R		Hindrance of electron passage through matter
Constant phase element (CPE)	$\frac{1}{T(j\omega)^P}$		Distribution of capacitances
Warburg	$R \frac{\tanh[(jT\omega)^P]}{(jT\omega)^P}$		Charge transfer reaction in porous material

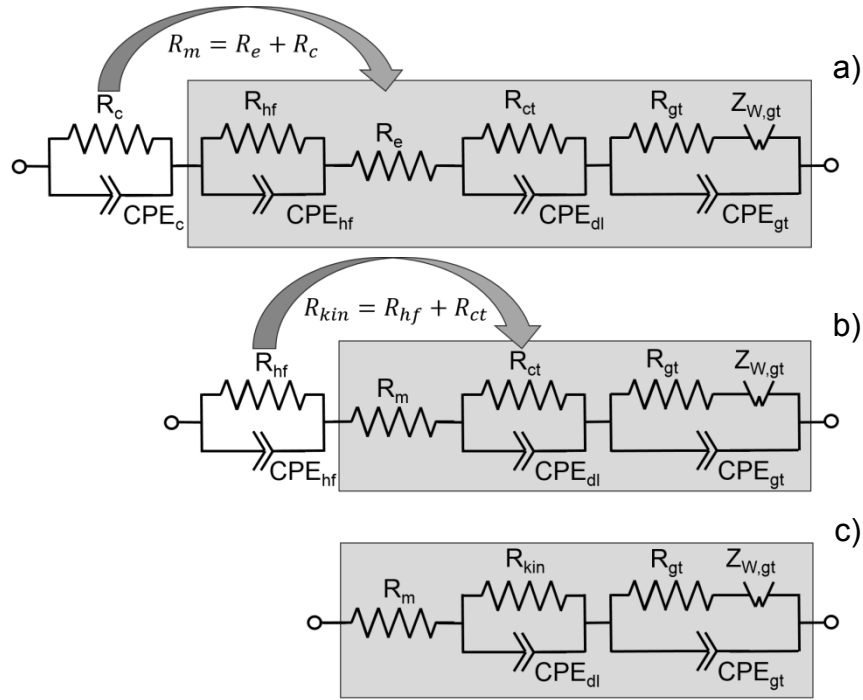


Figure 40: a) Applied equivalent circuit for fitting procedure, b) and c) the corresponding ECs after both simplification steps [31].

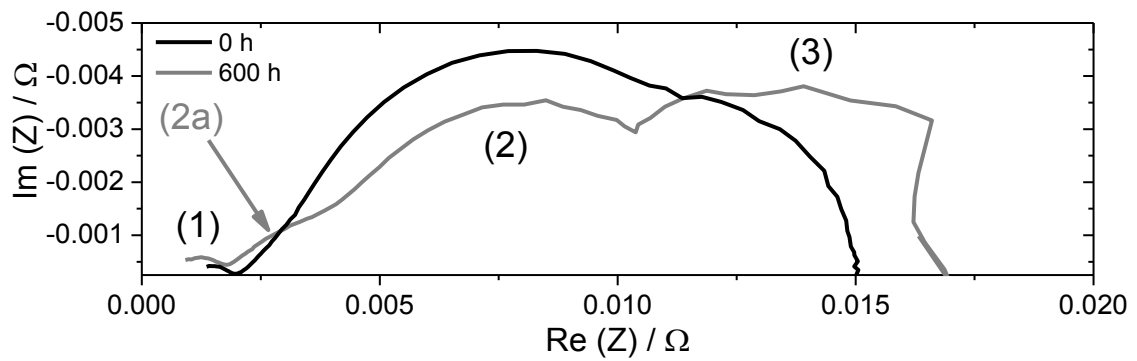


Figure 41: Nyquist plots of the EIS measurements of the leached and heat treated Pt-Co/C based HT-PEM MEA at BoL and after 600 h of operation.

In Figure 41 the recorded EIS spectra of the leached and heat treated Pt-Co/C based MEA are presented in form of their Nyquist plots. The measurement at the beginning of the long term operation shows three depressed semicircles, while after 600 h of operation a fourth arising semicircle (2a) may be observed additionally.

Both impedance spectra show the same frequency dependence and are interpreted as follows.

The beginning semicircle (in Figure 41 indicated with (1)), which was observed in the very high frequency area may not be attributed to an anode charge transfer reaction since the characteristic frequency (23208 Hz) was too high to be formed by a chemical reaction. The origin of this rc element was due to contact resistance between the flowfield plates and the membrane electrode assembly, while the capacitance was attributed to small amounts of H_3PO_4 at the interface between the two layers. Other explanations for such a behaviour refer these potential independent high frequency semicircles to the distribution of resistance effects within the electrolyte in the catalysts layer [120,121]. This phenomenon led to the fact that the high frequency intercept, which is commonly ascribed to the electrolyte resistance (R_e), was not seen directly within the observed frequency range. Therefore, the membrane resistance was obtained by calculating the sum of these distributed ohmic contact resistances (R_c) and the electrolyte resistance (R_e) and is in accordance with references [118,122] denoted by membrane resistance (R_m).

In the mid frequency area (indicated as (2) in Figure 41, 0 h) at least one depressed semicircle was observed and was attributed mainly to the ORR charge transfer reaction. The corresponding anode impedance semicircle or anode loop is masked by the more significant ORR semicircle. Especially at the beginning of the long term operation the characteristic frequencies are too close together to be seen as separate semicircles. After 600 h of operation at constant load the characteristic frequencies separated leading to two semicircles in the Nyquist plot and the anode reaction semicircle (2a) was observed. Since the origin of this loop is still under discussion the corresponding equivalent circuit element is denoted herein by high frequency loop ($R_{hf}||CPE_{hf}$) instead of anode loop [123].

In the low frequency area (3) mass transport limitations were observed in both spectra, but were more significant after 600 h of operation. Additionally, the

fluctuations in the low frequency arc (see Figure 42) indicated a slight flooding event. According to this interpretation the equivalent circuit shown in Figure 40 was applied for our fitting procedure and simplified for the discussion.

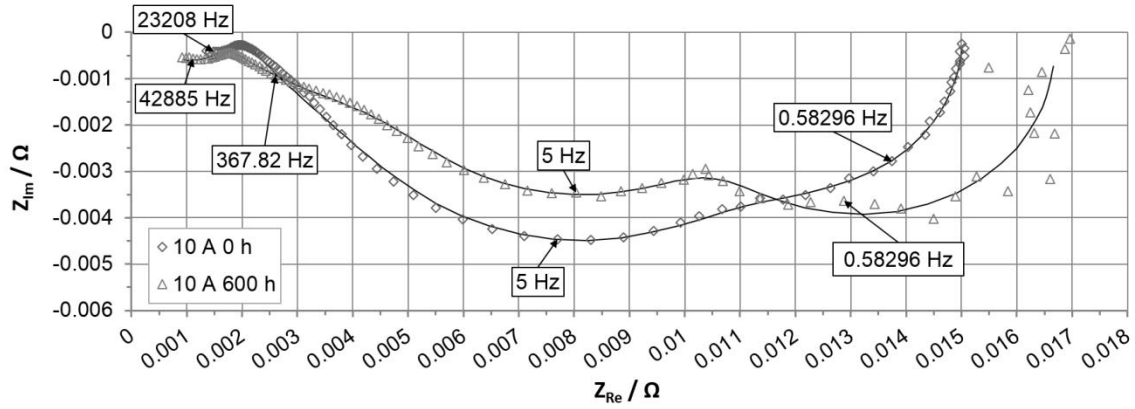


Figure 42: Nyquist plots of the EIS measurements of the leached and heat treated Pt-Co/C based HT-PEM MEA at BoL and after 600 h of operation and the corresponding fits [31].

The formulas applied for the fitting procedure as well as the obtained parameters are shown in Table 7. The kinetic resistance R_{kin} is the sum of the charge transfer and high frequency resistances ($R_{ct} + R_{hf}$). The membrane resistance R_m is, as described above, the sum of the ohmic contact resistances (R_c) and the electrolyte resistance (R_e). R_{gt} specifies the resistance occurring by the transport of the reactant gases through the porous layer of the GDE. The overall Warburg impedance Z_W was calculated from the Warburg diffusion interpretation parameter T_W , the finite length Warburg resistance R_W and the Warburg exponent P_W . The second column of Table 7 specifies the different coefficients T_{ct} , T_{hf} , T_c and T_{gt} and their corresponding exponents P_{ct} , P_{hf} , P_c and P_{gt} of the constant phase elements (CPEs) given in Figure 40 [31].

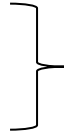
Table 7: Parameters obtained by the EC fitting procedure (*: fixed parameters) [31].

		0 h	600 h			0 h	600 h
${}^0R_{kin}$	R_{ct} / Ω	5.01E-03	4.99E-03	${}^2T_{dl} / A V^{-1}$	$\dim[(j\omega)^{-P}]$	1.17E+01	7.91E+00
	R_{hf} / Ω	4.81E-03	4.61E-03	${}^2T_{hf} / A V^{-1}$	$\dim[(j\omega)^{-P}]$	5.10E+00	6.29E+00
0R_m	R_c / Ω	1.48E-03	1.21E-03	${}^2T_c / A V^{-1}$	$\dim[(j\omega)^{-P}]$	1.00E-02	1.00E-02
	R_e / Ω	4.70E-04	3.18E-04	${}^2T_{gt} / A V^{-1}$	$\dim[(j\omega)^{-P}]$	50.4E+00	57.4E+00
R_{gt}	R_{gt} / Ω	3.08E-05	1.17E-03	${}^2P_{dl}$		6.43E-01	5.59E-01
	T_w	3.77E-04	3.77E-04	${}^2P_{hf}$		1.09E+00	1.02E+00
1Z_w	R_w / Ω	3.27E-03	4.41E-03	2P_c		8.58E-01	9.00E-01
	$*P_w$	0.5	0.5	${}^2P_{gt}$		1.10E+00	1.10E+00

$${}^0R_{kin} = R_{ct} + R_{hf}$$

$${}^1Z_w = R_w \frac{\tanh[(j\omega T_w)^{P_w}]}{(j\omega T_w)^{P_w}}$$

$${}^2Z_{CPE} = \frac{1}{T_x(j\omega)^{P_x}}$$



Applied formulas

j = square root of -1; ω = angular frequency / rad s⁻¹

All of these parameters exhibited changes during the long term operation experiment. After the first step of simplification the membrane resistance R_m ($= R_c + R_e$, see Table 7) decreased from 1.95 m Ω to 1.53 m Ω which is slightly lower than the obtained 1 kHz AC resistance (Figure 39) recorded throughout the long term experiment. This decrease indicated an improved electrolyte distribution within the active layer, which led to a decrease of R_c and R_m , respectively. Furthermore, it indicates that the main part of the membrane resistance rather originated from an insufficient electrolyte distribution in the active layer than from the electrolyte resistance itself [31].

The decrease in the diameter of the mid frequency semicircle ($R_{\text{kin}} = R_{\text{ct}} + R_{\text{hf}}$, see region (2) in Figure 41) was also due to the improved electrolyte distribution within the catalysts layer. During the operation the exponent (P_{dl}) of the constant phase element ascribed to the double layer (CPE_{dl}) decreased as well, which generally indicates a broader distribution of time constants and a better distribution of H_3PO_4 . Both tendencies, the decreased R_{kin} as well as the decreased P_{dl} , indicated an increased active catalyst surface area due to an improved H_3PO_4 distribution. But nevertheless, the fractional increase of the obtained ECSA by CV analysis (see Figure 43) goes beyond the fractional increase of the kinetic conductance (Table 8). This difference may be explained by the surface roughening effect of the catalysts particles, which increases the accessible inner surface of the catalysts particles and consequently the obtained ECSA.

Table 8: The ECSA increase vs. the increase of the kinetic conductance ($S_{\text{kin}} = 1/R_{\text{kin}}$) [31]

	ECSA / $\text{cm}^2 \text{mg}_{\text{Pt}}^{-1}$	R_{kin} / Ω	$S_{\text{kin}} / \Omega^{-1}$
0 h	104	9.82E-03	102
600 h	113	9.60E-03	104
Ratio	1.09		1.02

According to the obtained parameters (Table 7) the diameter of the low frequency semicircle, which was observed more clearly after 600 h of long term operation under constant load increased. This may be attributed to an increased wetting of the active layer and consequently longer diffusion pathways when thinking of a flooded agglomerate model [124]. The fluctuations in the low frequency arc also indicated a slight flooding of the active cathode catalyst layer although the polarisation curve did not indicate such an issue [31].

3.4.4.4 Cyclic voltammetry

Cyclic voltammetry was performed to investigate the in-situ ECSA of the cathode. Therefore, voltammograms were recorded by fuelling the MEAs with dry hydrogen on the anode and using it as pseudo-reference electrode and supplying the cathode side with humidified nitrogen.

In Figure 43 the cyclic voltammograms of the leached and heat treated Pt-Co/C based HT-PEM MEA before and after the durability test are shown. During operation the in-situ electrochemical active surface area of the cathode catalysts layer increased slightly from 104 to 113 $\text{cm}^2 \text{mg}_{\text{Pt}}^{-1}$. This enlargement of the active surface area can be attributed either to the redistribution of the H_3PO_4 electrolyte in the doped catalysts layer, resulting in an improved membrane resistance ($R_m = R_e + R_c$) as well as improved kinetic conductance ($S_{\text{kin}} = 1/R_{\text{kin}}$), as observed in EIS measurements, or to an additional removal of impurities and inactive Co sites at the surface of the GDE [31].

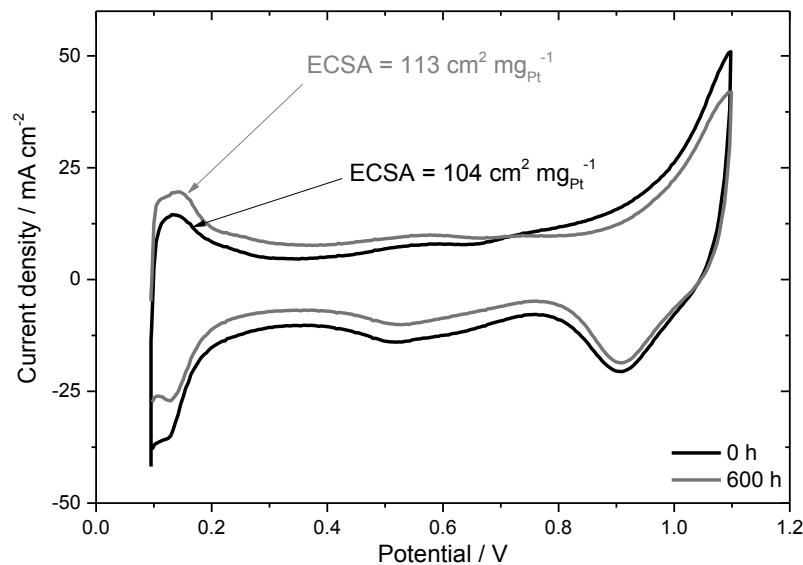


Figure 43: Cyclic voltammograms of the cathode layer of the leached and heat treated Pt-Co/C based HT-PEM MEA before and after long term operation test, recorded at a scan rate of 50 mV s^{-1} . The anode (fed with dry hydrogen) was used as pseudo-reference electrode. The cathode was supplied with humidified nitrogen [31].

3.4.4.5 Accelerated stress test

Since the leached and heat treated Pt-Co/C catalysts showed an improved stability over the standard Pt/C catalysts in ex-situ accelerated stress tests and in long term operation, further investigations concerning the durability of the Pt-Co/C electrocatalysts were executed. In order to investigate this durability and lifetime behaviour of the catalysts in situ accelerated stress tests (ASTs), which mimic the HT-PEMFC operation of one year, were established. These in-situ ASTs were carried out by fuelling hydrogen on the anode with a stoichiometry of 1.2 and air at the cathode with a stoichiometry of 2.0, using the following protocol (see also Figure 44):

- Phase 1: operation under constant load of 0.2 A cm^{-2}
- Phase 2: fast change between open circuit voltage (OCV) and operation under 0.2 A cm^{-2} every 30 seconds and followed by operation under constant load of 0.2 A cm^{-2}
- Phase 3: fast change between open circuit voltage (OCV) and operation under 1.0 A cm^{-2} every 30 seconds and followed by operation under constant load of 0.2 A cm^{-2}
- Phase 4: 10 start-stop cycles without flushing the anode with inert gas (nitrogen):
 - immediate shut down of electrical load
 - immediate shut down of gas-supply
 - cooling of the cell temperature down to $30 \text{ }^\circ\text{C}$
 - heating of the cell to operating temperature of $160 \text{ }^\circ\text{C}$
 - operation under constant load of 0.2 A cm^{-2}
- Phase 5: operation under constant load of 0.2 A cm^{-2}

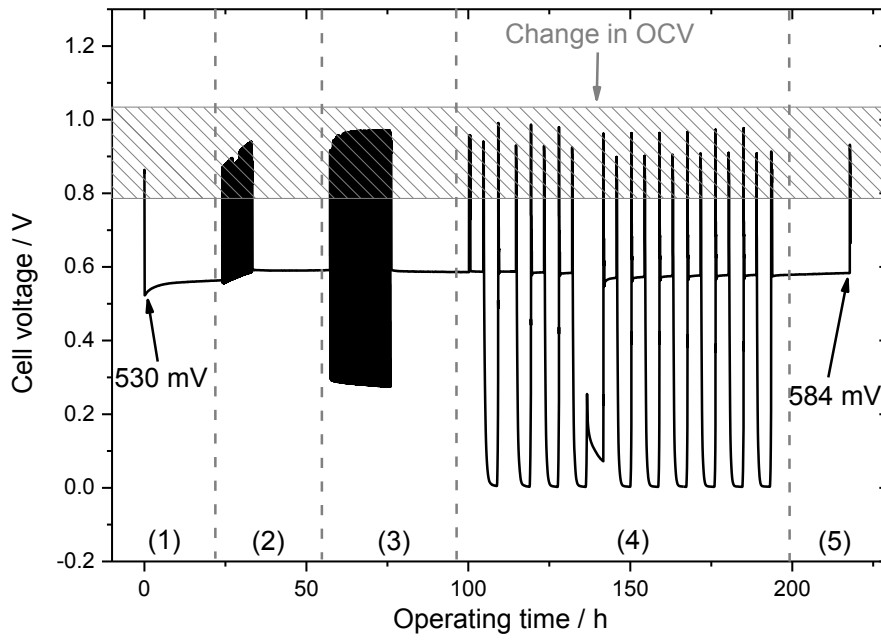


Figure 44: In-situ HT-PEM fuel cell accelerated stress test of the Pt-Co/C catalysts.

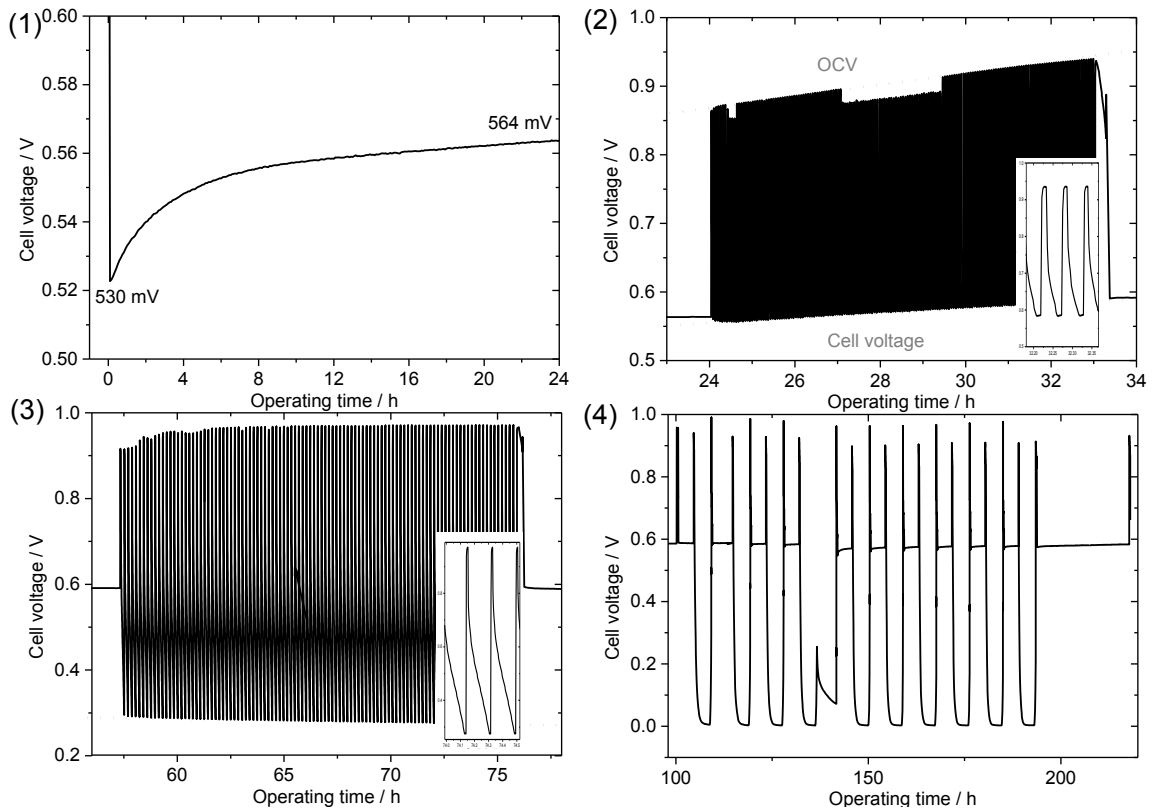


Figure 45: Zoom of the different phases of the in-situ AST.

Figure 44 depicts the overall in-situ AST of a Pt-Co/C based HT-PEM membrane electrode assembly. Clearly, the performance of the HT-PEM MEA improved during the AST procedure. This can be observed from the initial cell voltage of 530 mV and the final cell voltage of 584 mV. As described earlier the Pt-Co/C catalyst based MEA reveals a strong conditioning behaviour after doping with phosphoric acid and hot-pressing. Therefore, within the first 24 h an increase of the cell voltage of 34 mV, which corresponds to a voltage gain of 1.42 mV h^{-1} was obtained (Figure 45, Phase 1). The voltage gain is attributed as described above to a redistribution of the electrolyte phosphoric acid and the more accessible electrochemically active catalyst surface area (ESCA). In Phase 2 (Figure 45(2)) the cycling between the open circuit voltage (OCV) and the operating voltage at a load of 0.2 A cm^{-2} is given. The performance improvement of the HT-PEM MEA continued in this phase. The dotted grey lines indicate the improvement of the OCV as well as of the cell voltage. Figure 45(3) offers a zoom into the 3rd phase of the in-situ accelerated stress test. Within this phase the fast change between OCV and operation at a load of 1.0 A cm^{-2} , which is 5 times higher than the usual load, was performed. Typically during this operation the performance of MEAs starts to decrease and the catalysts start to degrade. This can be seen by the grey dotted lines. During the duration of phase 3 (20 hours) the cell voltage decreased slowly, resulting in a voltage loss of 2-3 mV. Phase 4 (Figure 45(4)) consisted of 10 “hard” start-stop cycles, which reflect a shut-down of the HT-PEM fuel cell, due to failure conditions, e.g. loss of gas supply. In contrast to a controlled shut-down procedure, here the gas supply is stopped as well as the load is removed immediately. Normally, the anode would be flushed with an inert gas to remove residues of hydrogen from the fuel cell, in order to prevent carbon corrosion [58]. Ideally, to maintain a highly active HT-PEM fuel cell system such hard shut-downs must not occur. Nevertheless, due to possible failure and insecurities in the gas supply chain or grid, these worst-case scenarios need to be tested and their influences on the lifetime of the system need to be

determined. As can be seen in Figure 45(4) the Pt-Co/C based MEA revealed a good performance during the hard start and shut-down cycles. During these 10 cycles only 8 mV of cell voltage were lost, whereby afterwards the cell voltage rose again.

Overall the Pt-Co/C based membrane electrode assembly demonstrated a good performance and a high stability. Due to the conditioning effect at the beginning of the in-situ AST, the degradation rate was negative, which means the cell voltage increased during the stress test procedure by $363 \mu\text{V h}^{-1}$ or 54 mV in total.

Despite these promising stability properties of the Pt-Co/C catalysts in in-situ ASTs the targeted cell voltage of 0.6 V at a current density of 0.2 A cm^{-2} was not reached. Maybe the manual impregnation of large GDEs led to a non-optimal distribution of catalysts on the surface of the GDE and low ECSA. Therefore, the manual impregnation was refined and further in-situ ASTs of Pt-Co/C based MEAs were performed (Figure 46).

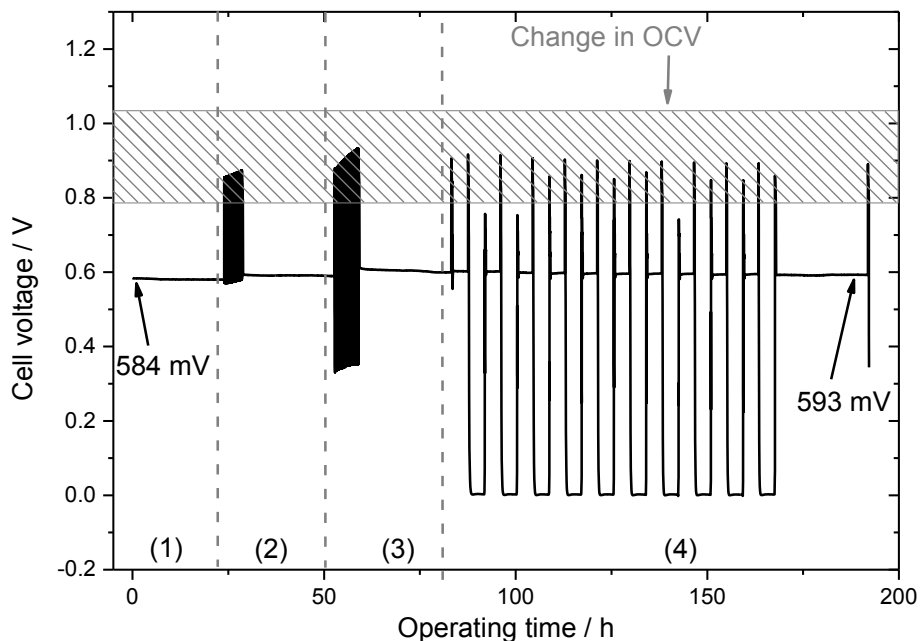


Figure 46: In-situ HT-PEM fuel cell accelerated stress test of the Pt-Co/C catalysts after refined preparation.

After refinement of the manual impregnation the HT-PEM MEAs showed an improved performance. Already after hot-pressing of the MEA a cell voltage of 584 mV was obtained. This cell voltage equals the cell voltage which was obtained with previous fabricated Pt-Co/C based MEAs after conditioning and AST cycling. The “new” Pt-Co/C based MEAs showed only a slight conditioning during phase 2 and 3 of the AST. As can be seen in Figure 46 during these two phases the OCV increased from 850 to 932 mV. However, in contrast to previous MEAs the cell voltage of the refined Pt-Co/C based MEAs did not increase. Over the complete in-situ AST the cell voltage was maintained at the same level. Only a slight increase of 9 mV was observed. Overall, the refinement process of the manual impregnation and preparation of the Pt-Co/C based HT-PEM MEAs led to an improved performance, which attributed to a better distribution of active catalysts on the surface of the GDE and a reduction of impurities, which could influence the performance of the MEA. The “new” MEA showed a very stable performance and a further improvement of the catalyst durability.

3.4.5 HT-PEM stack measurements

After testing and characterising the Pt-Co/C catalysts in-situ in single HT-PEM fuel cells, the next step was to test the Pt-Co/C based membrane electrode assemblies in fuel cell stack operation. For this the Pt-loading at anode and cathode were kept at 0.8 mg cm^{-2} and 1.0 mg cm^{-2} , respectively. As described earlier, for stack testing the size of the MEAs needed to be enlarged from 50 to 153 cm^2 . This enlargement was also performed by manual impregnation of larger GDE sheets. The results obtained from the stack test are based on the very first electrodes, which were fabricated with this size. Due to long testing time it was not possible to perform a second stack test after refinement of the manual impregnation.

The in-situ stack testing of the Pt-Co/C electrocatalyst based HT-PEM MEAs slightly differs from the testing procedure which was used for single cell characterisation. At the beginning a long term operation at a constant load of 0.2 A cm^{-2} was performed while fuelling the anode with reformat from methanol instead of hydrogen (see Figure 47). The cathode was supplied with air. In both cases the stoichiometries were kept at the same level as in single cell testing. For the stack test three Pt-Co/C based HT-PEM MEAs were tested in a 20 cell stack. The other cells contained different electrodes for testing and three standard Pt/C based MEAs for referencing purpose.

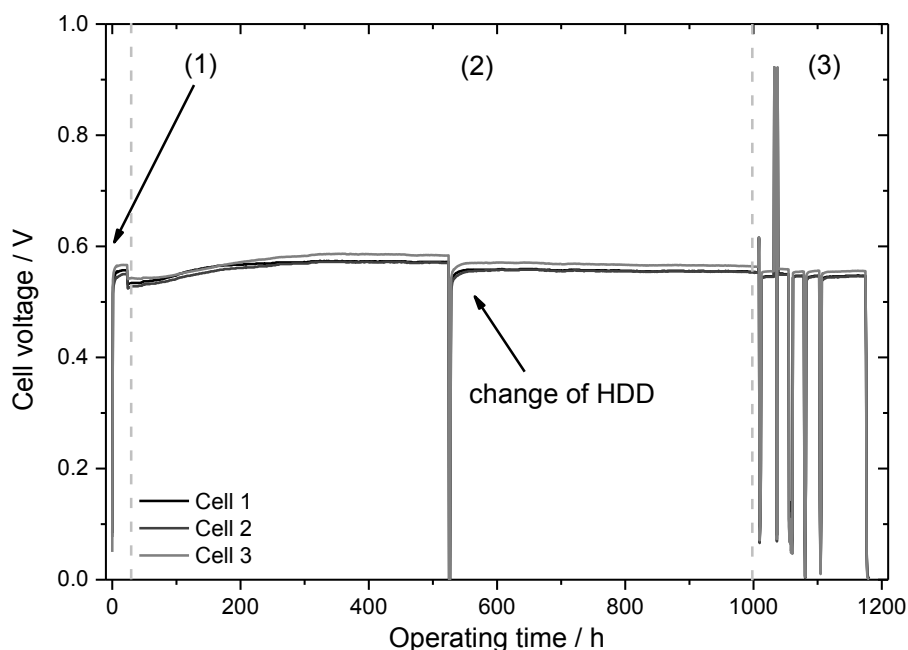


Figure 47: Long term operation of 3 Pt-Co/C based HT-PEM MEAs in a HT-PEM fuel cell stack test.

The HT-PEM fuel cell stack test was divided into 3 different phases. Phase (1) was considered to be a conditioning phase. Therefore, for the first 24 hours the electrical load during this phase was 0.16 A cm^{-2} , slightly lower than at normal operation. Phase (2) was the standard operation at 0.2 A cm^{-2} . The spike at approx. 508 h was due to change of the hard drive disk (HDD) and a hard shut-down. After 1000 h of long term operation a small in-situ AST was performed. This AST consisted of the

same testing elements, which are described above in single cell ASTs. Additionally, a change between reformate and hydrogen was performed, in order to investigate if operation with hydrogen could recover some cell voltage.

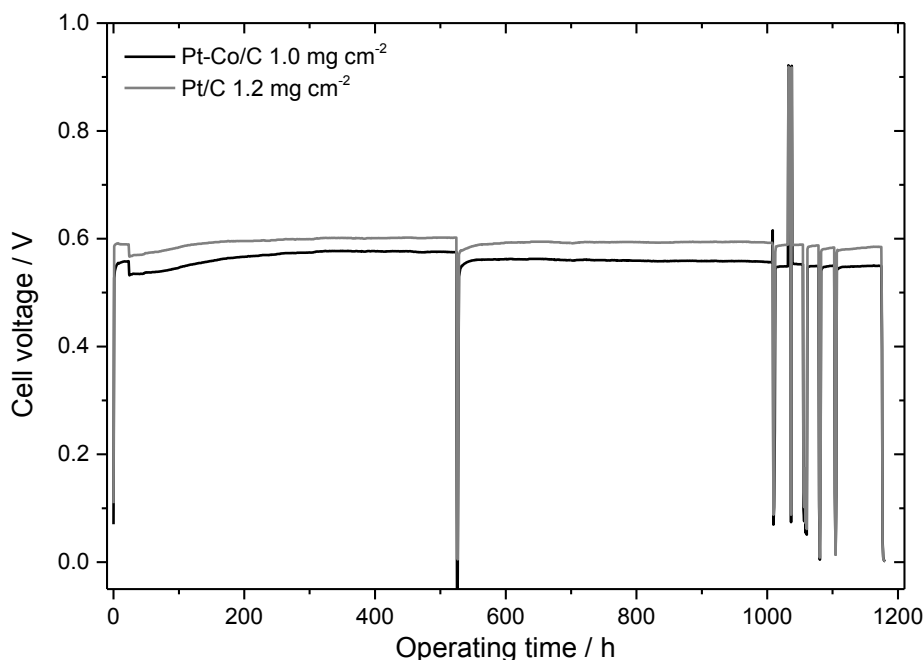


Figure 48: Comparison of the standard Pt/C and the Pt-Co/C based MEAs during long term HT-PEM stack operation. The mean cell voltages of 3 Pt-Co/C and 3 Pt/C MEAs are depicted.

Figure 48 depicts the mean cell voltage of the three Pt-Co/C based HT-PEM MEAs in comparison to the mean cell voltage of the standard Pt/C based MEAs. It is obvious that the Pt/C based MEAs exhibited a higher cell voltage during the long term operation with reformate at the anode. The difference in cell voltage is ascribed to the better fabrication environment of the Pt/C electrodes. These electrodes were fabricated in an automated process, which was optimised for this catalyst deposition, whereas the Pt-Co/C based MEAs were fabricated manually without optimisation. Furthermore, the approx. 20% higher Pt loading at the cathode of the standard MEAs also helped to maintain a higher cell voltage while operating on reformate.

Nevertheless, both catalysts were further tested in long term in-situ AST cycling, which is depicted in Figure 49.

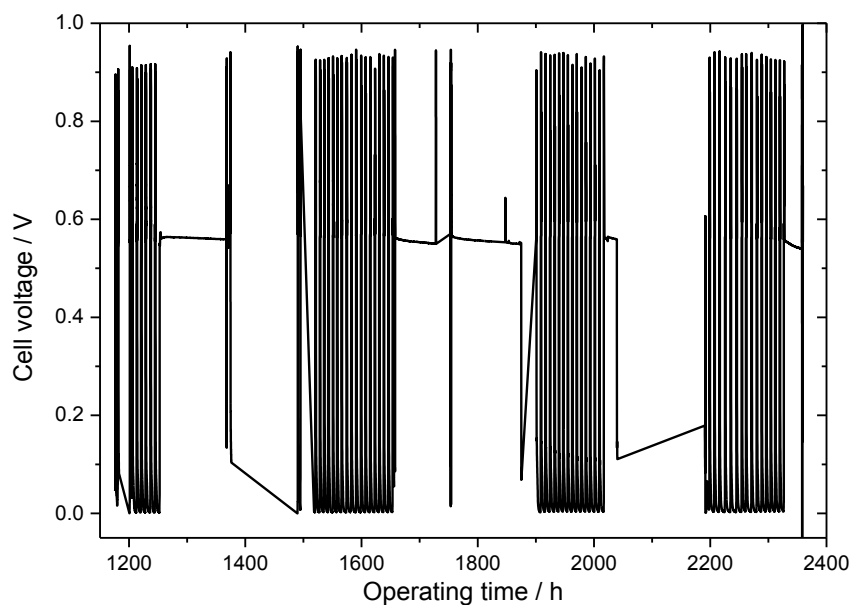


Figure 49: Long term HT-PEM in-situ AST of the Pt-Co/C based MEA in stack operation.

For this long term in-situ AST the anodes of the stack were supplied with hydrogen instead of methanol reformat. Over a time-span of almost 1200 hours the stack was subjected to standard operation at 0.2 A cm^{-2} and hard shut-down cycling. During this in-situ AST test the Pt-Co/C based MEAs, even though they were fabricated manually, showed good durability and only lost 23 mV of cell voltage.

Chapter 4

4 Summary and outlook

*“The important thing is do not stop questioning.
Curiosity has its own reason for existence. One
cannot help but be in awe when he contemplates
the mysteries of eternity, of life, of the marvellous
structure of reality. It is enough if one tries merely
to comprehend a little of this mystery every day.
Never lose a holy curiosity.”*

—Albert Einstein

The aim of this thesis was to integrate an economic, flexible and continuous platinum-transition metal (Pt-M/C) catalyst preparation into a large scale membrane electrode assembly manufacturing for high temperature PEMFCs. The main objective of the work lay in the establishment of an active and stable catalyst system, which enabled a reduction of the precious metal loading and the costs of a state-of-the-art membrane electrode assembly [31].

In order to obtain an inexpensive catalyst system for PEM fuel cells, an alternative to platinum, which is the state-of-the-art catalyst at the cathode, needs to be identified. This means platinum must be replaced either completely or partially by catalysts made of abundant elements. By an appropriate combination of platinum with other metals (e.g. Pd, Ru, V, Cr, Co, Ni, Cu etc.) it is possible to increase the activity toward ORR significantly and hence reduce the Pt loading at the cathode [36,71–82]. In particular, the formation of platinum alloys with late transition metals such as Co has been investigated extensively [76,80–88]. The reported Pt-Co catalysts show an increased activity toward ORR compared to pure Pt. However, the laborious synthesis protocols of these Pt-Co catalysts disable an efficient and economic production of membrane electrode assemblies [31].

In this thesis Pt-Co/C catalysts for the oxygen reduction reaction in high temperature PEM fuel cells were synthesised, electrochemically characterised and evaluated in fuel cells. Thereby, an easily up-scalable synthesis process and post-preparation treatment steps were developed. Subsequently, the synthesis parameters of the Pt-Co/C catalysts were adjusted and optimised in order to obtain best catalytic activity and highest stability. To obtain a higher Pt utilisation the continuous deposition of the catalysts was achieved directly in the optimised porous layer of the gas diffusion electrode. In contrast to conventional casting of catalyst loaded high surface area carbon onto the GDL, the loss of Pt during production is reduced by the presented process, rendering it more economical. Furthermore, Pt enclosures in carbon aggregates are eliminated and due to the absence of batch processes, such as filtering, centrifugation, multiple washing, drying and annealing in tube furnaces, the herein presented continuous MEA fabrication is much more time and cost saving [31].

More detailed, HT-PEM cathodes were prepared by impregnating gas diffusion electrodes with precursor solutions containing dissolved Pt and Co salts in a molar ratio of 1:5 and ethylene glycol as reducing agent. The salts were reduced into the corresponding metallic nanoparticles by applying a heat treatment at 240 °C. In order to improve sluggish catalytic properties of the Pt-Co/C catalysts post-preparation treatments were identified and introduced into the manufacturing process. Firstly, the Pt-Co/C catalyst containing GDE sheets were leached in 10% sulphuric solution. This leaching process led to an increased electrochemical surface area, due to dissolution of inactive Co atoms and other impurities at the surface of the catalysts, leaving behind a so called Pt-skeleton surface structure. This skeleton structure exhibited improved catalytic properties and a higher stability than the untreated Pt-Co/C catalysts. The catalytic improvement was assigned to leaching induced strain-effects rather than to electronic ligand effects. The latter are less pronounced due to the very low Co content after the leaching (see Structural and chemical analysis). The second post-preparation treatment was a heat treatment of the catalysts at temperatures between 200-220 °C in nitrogen-saturated atmosphere. The heat treatment was performed by applying a heating ramp of 5 °C min⁻¹ and holding the final temperature for 45 min. Thereby the nominal composition of the nanoparticles was not altered. However due to the lower surface energy of Pt in comparison to the transition metal the surface of the leached Pt-Co/C catalysts was rearranged. Platinum segregated to the surface within the catalyst alloy resulting in a Pt overlayer (Pt-skin) which rendered the catalysts more stable against the corrosive environment of a HT-PEM fuel cell. Furthermore, a slightly higher Pt surface area was obtained due to the cleaning effect of the elevated temperature, which decomposed organic residues of the impregnation solution, such as the surfactant, ethylene glycol and its oxidation products [31].

Due to the promising results from the electrochemical ex-situ characterisation the leached and heat-treated Pt-Co/C catalysts were tested at the cathode of HT-

PEMFC single cells and in an HT-PEMFC stack. To evaluate the activity and stability under in-situ conditions a commercially available HT-PEM MEA was tested in the same protocols. The leached and heat-treated Pt-Co/C catalysts showed a very high stability in HT-PEM fuel cell operation under constant load and during start-stop cycling. Both the commercial HT-PEM MEA and the herein described Pt-Co based HT-PEM MEA performed equally and the same cell voltages and performance were obtained. Nevertheless, due to the 20% higher Pt-loading at the cathode of the commercial MEA, the leached and heat-treated Pt-Co/C catalyst system outperformed the commercial sample in terms of Pt-utilisation and activity.

Future projects would need to further investigate the influence of heat-treatment on the Pt-Co/C catalysts by varying time, temperature and the ambient atmosphere. Also, all presented manufacturing steps, from preparation of the GDE to the assembling of the MEA, need to be automated. With this, the synthesis of the Pt-Co/C catalysts would become more reproducible and more reliable, and a further reduction of the Pt-loading at the cathode could be achieved.

*“Insanity:
doing the same thing over and over again
and expecting different results.”*

—Albert Einstein

5.1 Materials and methods

5.1.1 Chemicals

All chemicals were used as purchased without further purification.

- High surface area carbon gas diffusion electrodes (GDE) provided by elcomax GmbH Munich; turbostratic carbon with a loading of 2.8 mg cm^{-2}
- 3M Dyneon, TF 5035 PTFE
- $\text{H}_2\text{PtCl}_6 \cdot 6\text{H}_2\text{O}$ ACS grade $\geq 37.5\%$ Pt basis (Sigma-Aldrich)
- $\text{Co}(\text{NO}_3)_2 \cdot 6\text{H}_2\text{O}$ ACS $\geq 98\%$ (Sigma-Aldrich)

- Ethylene Glycol $\geq 99.5\%$ (Fluka Analytical)
- 2-propanol ACS grade $\geq 99.8\%$ (Sigma-Aldrich)
- Ultrapure H₂O 18.2 M Ω (Barnstead Nanopure)
- Brij-30® M_n ~ 362 (Sigma-Aldrich)
- Dimethylacetamide (N,N-DMAc), synthesis grade (Merck)
- H₂SO₄ ACS grade 95-98% (Sigma-Aldrich)
- HCl p.a. $\geq 32\%$ (Fluka Analytical)
- 0.1 M HClO₄ acid concentrate for 1l standard solution (Fixanal®, Fluka Analytical)
- Nitrogen (5.0, Messer Group GmbH)
- Oxygen (5.0, Messer Group GmbH)
- Alumina Suspension 0.05 μm (MasterPrep, Bühler)
- Hydrogen (3.0, Westfalen AG)
- Synthetic reformat (76.0% H₂, 1.2% CO and 22.8% CO₂, Westfalen AG)
- 1-pentanol ACS grade $\geq 99\%$ (Sigma-Aldrich)

5.1.2 Instruments and equipment

- Bi-potentiostat/galvanostat by Metrohm Autolab B.V., type PGSTAT302N
- Ring-Disk Electrode System by Pine Instruments (Model 636)
- Ring disk electrode (glassy carbon area 0.196 cm²) by Pine Instruments (Model AFE5T050GC)
- Hydrogen Reference Electrode (Gaskatel HydroFlex) by Gaskatel Gesellschaft für Gassysteme durch Katalyse und Elektrochemie mbH
- Platinized titanium rod counter electrode by Bank Elektronik - Intelligent Controls GmbH
- Electrical laboratory furnace by Elsklo, type LNT15G/1320 °C/5.5kW/Dicon

- Ultrasonic bath Bandelin Sonorex by Bandelin electronic, type RK31
- Zahner Elektrik electrochemical workstation type IM6ex
- Zahner Elektrik power potentiostat, type PP241

5.1.3 Data treatment

- NOVA 1.7.8 by Metrohm Autoalab B.V.
- Microsoft Office Excel by Microsoft
- OriginPro 9.0 by OriginLab

5.2 Catalyst preparation

5.2.1 Preparation of gas diffusion electrodes

The gas diffusion electrodes (GDE) were prepared by applying high surface area carbon (HSAC) on a wet proofed carbon based gas diffusion cloth via doctor blading. The applied catalyst support slurry consisted of turbostratic HSAC (t-carbon or disordered graphite) HSAC, with a BET area of 250-300 m² g⁻¹, a PTFE dispersion, deionised water and 2-propanol. The gap of the doctor blade was adjusted to 610 μm to get a loading of 2.8 mg cm⁻² carbon/PTFE on the final gas diffusion electrode. The prepared GDE was dried at 170 °C under constant air flow.

5.2.2 Impregnation solution

The detailed experimental process of finding the right composition of the impregnation solution is described in detail in the master thesis of Christoph Grimmer [99].

For impregnating the GDE sheets an impregnation solution containing platinum and cobalt precursor salts, ethylene glycol as reducing agent, ultra-pure water and 2-propanol as solvents and Brij-30, a surface-active agent, was prepared. Due to the hygroscopic nature of $\text{H}_2\text{PtCl}_6 \cdot 6\text{H}_2\text{O}$, the salt was weighed in a glove box under inert atmosphere and dissolved in a known quantity of a mixture of ultra-pure water and 2-propanol in a volumetric ratio of 1:1 in order to obtain a Pt stock solution for further usage. The Co salt was dissolved in ultra-pure water, 2-propanol, ethylene glycol and Brij-30, whereby water, 2-propanol and ethylene glycol were added in following ratios 1:1:1.3. The non-ionic surfactant Brij-30 was added with a concentration of 0.034 mg ml^{-1} . Mixing together the appropriate amounts of the Pt stock solution and Co solution, respectively, yielded an impregnation solution having a stoichiometric ratio of Pt:Co of 1:5 and led to a Pt concentration of 19.4 mg ml^{-1} . Drop coating the impregnation solution on the prepared gas diffusion electrode sheets gave a Pt loading of 1.00 mg cm^{-2} and a Co loading of 1.52 mg cm^{-2} on the GDE, respectively.

5.2.3 Reduction of the precursor salts

The high surface carbon gas diffusion layer sheets (2.2 x 2.2 cm for small standard catalysts samples) were pre-dried in the drying oven for 30 min at $100 \text{ }^\circ\text{C}$ and then impregnated all-over with 250 μl of the prepared impregnation solution. For fuel cell testing, larger sized GDE sheets were impregnated by using the corresponding volume of the precursor solution to obtain a Pt loading of

1.00 mg cm⁻². After impregnation the GDE sheets were dried evenly at 100 °C in the drying oven to remove all solvents, leaving ultimately behind the metal salts and the reducing agent ethylene glycol at the surface of the electrodes. The reduction of the precursor salts itself was then executed in an electrical laboratory furnace at 240 °C for 10 min in nitrogen saturated atmosphere (N₂-flow = 100 l h⁻¹).

5.2.4 Post-preparation treatments

After reduction of the impregnated catalyst samples different post-preparation treatments were performed.

- **No treatment:** The samples were washed in water/2-propanol 1:1 for 30 min to remove organic and inorganic residues of the reduction process and dried overnight at room temperature.
- **Acid leaching:** The samples were acid-leached in 10 vol.% solutions of either H₂SO₄ or HCl in water/2-propanol 1:1 for 30 min, washed in water/2-propanol 1:1 for 30 min and dried overnight at room temperature.
- **Heat-treatment:** The samples were washed in water/2-propanol 1:1 for 30 min and dried overnight. Afterwards a heat-treatment in the lab furnace in N₂-saturated atmosphere was carried out by applying different temperature programs⁴.
- **Acid leaching and heat treatment:** First the samples were acid-leached in 10 vol.% H₂SO₄ or HCl solution, washed in water/2-propanol 1:1 for 30 min, dried overnight and finally heat-treated in the lab furnace.
- **Heat treatment and acid leaching:** The samples were washed in water/2-propanol 1:1 for 30 min, dried, heat-treated in the lab furnace and afterwards

⁴ Figuratively an uncountable number of different heating programs has been tested during the course of this PhD thesis. Different heating temperatures, different heating time spans, different heating ramps, and various combinations of these parameters have been tested.

leached in 10 vol.% H₂SO₄ or HCl solution, washed in water/2-propanol 1:1 for 30 min again and dried overnight.

5.3 Electrochemical characterisation of the catalyst samples and data treatment

Before performing any electrochemical measurement, all glassware was cleaned in hot sulphuric acid solution, followed by heating and rinsing with ultrapure water to remove sulphate residues. The electrochemical ex-situ experiments were carried out using an Autolab PGSTAT302N potentiostat from Metrohm Autolab B.V. The rotating disc electrode (RDE) assembly was a combination of a rotator and an electrode from Pine Instruments Company. A standard 3-electrode electrochemical set-up was used, whereby the working electrode was a commercial glassy carbon disc electrode of 5 mm fixed diameter (area 0.196 cm²), a platinised titanium rod was used as counter electrode and as reference electrode a reversible hydrogen electrode (RHE) was employed. For enabling measurement under different conditions, the electrochemical set-up was complemented with gas inlets for N₂, O₂ and H₂. While introducing gas into the electrolyte it has been assured that any gas bubbles could not interfere with the catalyst surface on the RDE.

The electrolyte, 0.1 M perchloric acid (HClO₄) was prepared with ultrapure water. Since it was impossible to apply the catalyst samples directly onto to the working electrode, a defined 2 cm² portion of the prepared and differently treated catalyst containing GDE sheets was taken in order to prepare a catalyst ink. The 2 cm² portion of the GDE was therefore sonicated in 3.64 ml of 2-propanol until a homogeneous catalyst dispersion was formed. A 10 µl aliquot (2 x 5 µl) of the

dispersion was then dispensed onto the working electrode resulting in a loading of 28 $\mu\text{g}_{\text{Pt}} \text{cm}^{-2}$ geometric surface area. Prior to electrode preparation, the glassy carbon rotating electrode disc was polished to a mirror finish using a 0.05 μm alumina suspension.

RDE measurements were conducted in a nitrogen saturated electrolyte, whereas, the oxygen reduction reaction (ORR) activity measurements were performed in an electrolyte saturated with oxygen. During all measurements the gas supply was sustained.

After immersing the working electrode into the electrolyte solution the internal resistance drop was determined by carrying out an impedance spectrum with a peak-to-peak amplitude of 10 mV in the range from 100 kHz to 1 Hz. The ohmic drop was evaluated from the high frequency intercept point on the real axis of the Nyquist plot. Typically the uncompensated resistance came to 25-30 Ω . Afterwards the electrocatalysts were pre-treated using 250 cyclic voltammetry scans between 0.050 and 1.255 V_{RHE} at a scan rate of 500 mV s^{-1} in order to remove undesired contaminations from the catalyst surface. After this cleaning procedure, three analysis cycles were performed from 0.050 to 1.055 V_{RHE} at 50 mV s^{-1} for data treatment. To investigate the ORR activity potential sweeps between 0.050 and 1.055 V with a scan rate of 50 mV s^{-1} were carried out. In contrast to standard CV scans, these ORR measurements were conducted at a rotating speed of the working electrode tip of 1600 rpm. Subsequently, after each measurement the potential of the reference electrode was controlled by performing the hydrogen evolution reaction on Pt in the same electrolyte.

In order to determine the stability and durability of the as-prepared catalyst samples accelerated stress tests (AST) were conducted. Therefor the electrodes were cycled 1665 times between 0.5 and 1.4 V_{RHE} in nitrogen saturated rated 0.1 M HClO_4 at a scan rate of 500 mV s^{-1} . Every 555th cycle three analysis cycles were performed.

Table 9: Summary of performed electrochemical measurement procedures

	Upper vertex vs. RHE / V	Lower vertex vs. RHE / V	Start/Stop potential / V_{RHE}	Scan speed / mV s^{-1}	No. of cycles
Warm-up	1.055	0.050	0.455	100	5
Cleaning	1.255	0.050	0.455	500	250
Analysis	1.055	0.050	0.455	50	3
ORR	1.055	0.050	0.455	50	Until stable
AST	1.400	0.500	0.500	500	3 x 555

5.3.1 Data treatment

The data derived from the cyclic voltammetry measurements were used to calculate the electrochemical active surface area (ECSA) of the catalyst samples. Therefore, the ECSA was determined from the mean integral charge Q_{Hupd} of the hydrogen adsorption/desorption area (H_{upd}) after double-layer correction, considering $210 \mu\text{C cm}_{\text{Pt}}^{-2}$ as conversion factor [36,110] according to Eq. 16.

$$ECSA = \frac{Q_{\text{Hupd}}}{Q_{\text{Pt}} \cdot L_{\text{Pt}} \cdot A_{\text{geo}}} \quad \text{Eq. 16}$$

Q_{Pt} is the electrical charge generally associated with the adsorption of a monolayer of hydrogen on a pure Pt surface with a literature value of $210 \cdot 10^{-6} \text{ C cm}^{-2}$, L_{Pt} is the Pt loading on the working electrode in $\text{mg}_{\text{Pt}} \text{ cm}^{-2}$, and A_{geo} (cm^2) is the geometric surface area of the glassy carbon electrode.

The software Nova, from Metrohm Autolab B.V., was used for determining the charge of the H_{upd} peak of the third CV analysis scan. Therefore, all currents were

corrected for the double layer formation at the electrode surface by defining a baseline under the peak area (as can be seen in Figure 50).

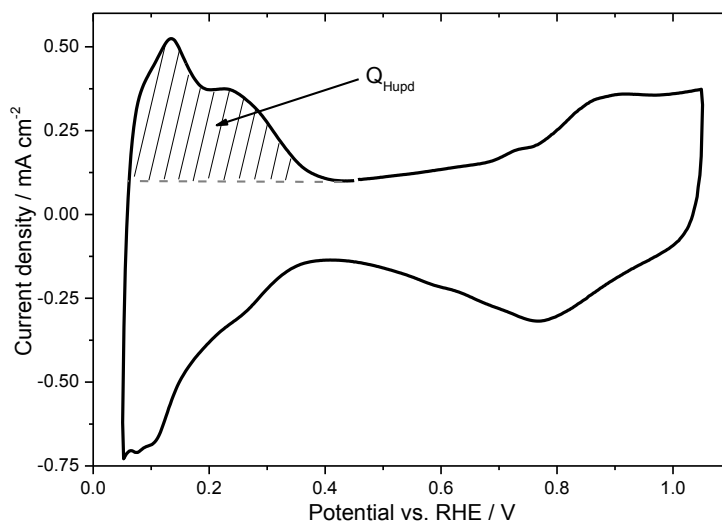


Figure 50: Determination the charge of the H_{upd} peak.

Afterwards the peak area was integrated using the software mentioned above. The value of the integrated area in $W (= VA)$ was divided by the scan rate in $V s^{-1}$ in order to obtain the charge Q_{Hupd} in $C (= A s^{-1})$.

All CV analysis cycles of the different catalyst samples were corrected for the reference potential and the currents were normalised to the geometrical area of the RDE ($= mA cm^{-2}$).

For the analysis of the ORR measurements, the second stable cycle was used for calculating the specific current density (SCD) of the catalyst in $mA cm^{-2}$ and the mass activity (MA) in $A mg_{\text{Pt}}^{-1}$. Before calculating SCD and MA, the CV analysis cycle measured in N_2 -saturated electrolyte was deducted from the ORR polarisation curve, in other words the contribution of the (background) currents related to the Pt-H, Pt-O or Pt-OH formation and decomposition were excluded from the ORR analysis. After background correction, only the positive (anodic) sweep of the ORR

experiment was used for determining the SCD and MA at 0.9 V_{RHE} according to Eq. 18 and Eq. 19, respectively.

$$\frac{1}{i} = \frac{1}{i_k} \cdot \frac{1}{i_{diff}}$$

Eq. 17

$$i_k = \frac{i_{diff} \cdot i}{i_{diff} - i}$$

i is the observed current of the polarisation curve at 0.9 V_{RHE}. i_{diff} is the diffusion limited current at 1600 rpm, which is the lowest observable current of the ORR polarisation curve in the plateau between 0.0 and 0.7 V_{RHE}. The kinetic current i_k was calculated according to the Koutecky-Levich equation (Eq. 17). The kinetic current was further used to estimate the specific current density (SCD), i.e. the Pt area-specific activity of the catalysts, by normalisation to the Pt electrochemical active surface area (ECSA), see Eq. 18.

$$SCD = \frac{i_k}{\frac{Q_{Hupd}}{Q_{Pt}}}$$

Eq. 18

For a better comparison to other catalysts in terms of activity per amount of used platinum, usually the mass activity (MA) of the catalyst in A mg_{Pt}⁻¹ is calculated. Therefor the kinetic current i_k is divided by the total platinum mass on the RDE, see Eq. 19.

$$MA = \frac{i_k}{L_{Pt} \cdot A_{geo}}$$

Eq. 19

An easy comparison of the activity of different catalysts can be obtained by preparing so-called Tafel plots. Tafel plots are, in general, obtained by using the RDE area normalised kinetic current density j_k instead of i_k and plotting it in a logarithmic scale versus a potential range typically close to 0.9 V_{RHE} (e.g. 0.8-1.0 V_{RHE}).

The stability and durability of the catalyst samples was estimated by the relative loss of electrochemical active surface area, derived from the CV analysis scans taken in between the accelerated stress test cycles (Eq. 20).

$$\text{Degradation} / \% = \frac{ECSA_{initial} - ECSA_{AST}}{ECSA_{initial}} \cdot 100 \quad \text{Eq. 20}$$

5.4 Structural and chemical analysis

For structural and chemical analysis of the prepared catalyst samples scanning transmission electron microscopy (S-TEM), energy dispersive X-ray spectroscopy (EDX) and X-ray diffraction analysis (XRD) were carried out.

5.4.1 Scanning transmission electron microscopy

A FEI Titan 80 - 300 scanning transmission electron microscope equipped with an EDAX energy dispersive X-ray spectroscopy detector for analytical measurements was used for the investigation of the catalysts nanoparticles. The measurements were performed at 300 kV.

In order to prepare the catalyst samples for TEM characterisation, the impregnated GDE material was suspended in 2-propanol/water (1:1), sonicated for 10 minutes and one droplet of the catalyst dispersion was applied on a holey carbon coated nickel grid.

The crystal structure was determined via electron diffraction patterns measured over several nanoparticles and by analysing high resolution TEM micrographs. In addition, the size and distribution of the catalyst particles was determined by TEM. The overall composition of the prepared catalyst samples before and after acid-leaching and heat-treatment was investigated via energy dispersive X-ray spectroscopy. The quantification of the at.% of the elements of the samples was done by using the Cliff-Lorimer equation for thin specimen [103], whereby the Pt L_{α} line at 9.441 keV and the Co K_{α} line at 6.924 keV were used for determining the atomic percentages of Pt and Co, respectively. The used software for the quantitative analysis was FEI's "TEM Imaging & Analysis".

5.4.2 X-ray diffraction analysis

X-ray powder diffraction profiles were obtained on a Bruker AXS D8 Advance powder diffractometer in Bragg-Brentano Θ - Θ geometry operated at 40 kV and 40 mA, using Cu K_{α} radiation ($\lambda = 1.54178 \text{ \AA}$). The 2Θ diffraction angles were measured by scanning the goniometer from 30-138 $^{\circ}2\Theta$ having a step size of 0.025 $^{\circ}2\Theta$. The profile-fit was performed using PANalytical X'Pert High Score Plus software using the crystal structure data of metallic Pt [104] and Co [108]. Calculations using Vegard's law (Eq. 21) [106,125] have been performed in order to investigate the formation of a Pt-Co solid solution.

The Vegard's law is an empirical rule of very importance in metallurgy. It predicts a linear variation in alloy lattice constants with composition, i.e. the lattice constant of the alloy decreases the higher the amount of solute metal gets within the solid

solution [74,106]. The only requirement for this assumption is that the metals constituting the solid solution show the same type of crystal structure.

$$a_{exp} = a_{Pt} \cdot (1 - x_{Co}) + a_{Co} \cdot x_{Co}$$

Eq. 21

$$x_{Co} = \frac{a_{exp} - a_{Pt}}{a_{Co} - a_{Pt}}$$

x_{Co} is the percentage of Co in the Pt-Co solid solution, a_{exp} the experimental observed lattice constant of the solid solution, a_{Pt} and a_{Co} are the lattice constants of pure platinum and cobalt, respectively.

The average primary crystallite sizes of the samples (d_{XRD}) were determined according to the broadening of the diffraction peaks using the Scherrer relationship [105] (Eq. 22), where d is the mean crystallite dimension, K is the shape factor (0.9), λ is the X-ray wavelength in nm, $\Delta(2\theta)$ is the peak broadening at full width at half-maximum in radians and θ is the Bragg angle.

$$d_{XRD} = \frac{K \cdot \lambda}{\Delta(2\theta) \cdot \cos \theta}$$

Eq. 22

5.5 Fuel cell testing and characterisation

Various fuel cell testing protocols have been performed. Several tests, including the record of polarisation curves, electrochemical impedance spectra and in-situ cyclic voltammetry have been executed in single cell set-up; whereas long

term operation under constant load and in-situ accelerated stress tests have been performed in single fuel cell set-up as well as in fuel cell stack tests.

All fuel cell measurements were carried out using the laboratory facilities of elcomax GmbH in Munich. In order to compare the Pt-Co catalysts to the standard Pt-based HT-PEM membrane electrode assemblies of elcomax, all single cell and stack tests with Pt-Co/C and Pt/C only based MEAs were carried out in parallel.

5.5.1 Membrane electrode assembly preparation

The Pt-Co electrocatalysts have been prepared on gas diffusion electrode sheets the same way as described above. After the deposition of the cathode catalysts the GDE sheets were sent to elcomax GmbH in order to prepare the membrane electrode assemblies (MEAs). The HT-PEM MEAs were manufactured by doping the catalyst layer with a mixture of phosphoric acid (85 wt.%) and 1-pentanol. After evaporation of 1-pentanol at 230 °C, the electrodes were hot pressed with a membrane based on polybenzimidazole (PBI) at 150 °C to form the membrane electrode assembly.

The PBI membranes were obtained from elcomax GmbH. In order to prepare the membranes meta-PBI powder was dissolved in dimethylacetamide (DMAc) under stirring for 3 h at 200 °C and under pressure. The resulting PBI solution was then casted onto a carrier foil by solvent evaporation in a temperature range of 70 to 100 °C. Afterwards, a thermal treatment of the membranes was performed to remove DMAc residues.

For the anode a standard Pt/C based GDE with a Pt loading of 0.8 mg cm⁻² from elcomax GmbH was used.

Before in-situ testing, every MEA was controlled to be gastight. Therefore, on one electrode side, either the anode or the cathode, a pressure of 50 mbar of compressed

air was applied. On the other electrode sensors detected the pressure. If this pressure was higher than 2-3 mbar, the HT-MEA was rejected for further testing.

5.5.2 In-situ characterisation

For single fuel cell testing membrane electrode assemblies with an active area of 50 cm² and 153 cm², were used and mounted in fuel cells having a serpentine channel flow field and parallel channel structure on anode and cathode, respectively. Whereas fuel cell stack tests were carried out only with MEAs having an active area of 153 cm² and the parallel gas flow channel flow fields.

Cell temperature was set to 160 °C controlled by electrical heating cartridges. The reactant flow rates were measured and controlled by mass flow controllers, and their stoichiometries were kept constant at 1.2 for hydrogen or synthetic reformat and 2.0 for air, respectively.

Long term operation under constant load was conducted at a current density of 0.2 A cm⁻² and at a temperature of 160 °C. The single cell was fuelled with hydrogen on the anode with a stoichiometry of 1.2 and air at the cathode with a stoichiometry of 2.0.

In-situ cyclic voltammetry was performed by using a Zahner power potentiostat (PP241) and a Zahner electrochemical workstation (IM6ex). Therefor the single fuel cells were fed with dry hydrogen on the anode, which was also used as pseudo-reference electrode, and humidified nitrogen on the cathode. The electrochemical active surface area of the Pt-Co electrocatalysts on the cathode was determined in an analysis scan with 50 mV s⁻¹ after prior cycling the cathode between 0.095 and

1.100 V with 100 mV s⁻¹ for 100 times. The ECSA was calculated according to Eq. 16.

Electrochemical impedance spectra (EIS) were recorded in a pseudo-galvanostatic mode with a Zahner power potentiostat (PP241) and the results are presented in Nyquist plots. The peak-to-peak amplitude was set to 5 mV at 0.2 A cm⁻². At the anode synthetic reformat was supplied.

Equivalent circuit (EC) analysis was used to quantify the different losses occurring in the as-prepared HT-PEM MEA.

In-situ accelerated stress tests (ASTs) were carried out by fuelling hydrogen on the anode with a stoichiometry of 1.2 and air at the cathode with a stoichiometry of 2.0, using the following protocol:

- Phase 1: operation under constant load of 0.2 A cm⁻²
- Phase 2: fast change between open circuit voltage (OCV) and operation under 0.2 A cm⁻² every 30 seconds
- Phase 3: operation under constant load of 0.2 A cm⁻²
- Phase 4: fast change between open circuit voltage (OCV) and operation under 1.0 A cm⁻² every 30 seconds
- Phase 5: operation under constant load of 0.2 A cm⁻²
- Phase 6: 10 start-stop cycles without flushing the anode with inert gas (nitrogen):
 - immediate shut down of electrical load
 - immediate shut down of gas-supply
 - cooling of the cell temperature down to 30 °C
 - heating of the cell to operating temperature of 160 °C
 - operation under constant load of 0.2 A cm⁻²
- Phase 7: operation under constant load of 0.2 A cm⁻²

6 References

- [1] NASA - Goddard Institute for Space Studies (GISS), GISS Surface Temperature Analysis (GISTEMP), 2014.
- [2] T.A. Boden, G. Marland, R.J. Andres, Global, Regional, and National Fossil-Fuel CO₂ Emissions, 2010.
- [3] United Nations - Department of Economic and Social Affairs - Population Division, World Population Prospects 2012, 2013.
- [4] United States Census Bureau, Historical Estimates of World Population, 2013.
- [5] IEA, Key World Energy Statistics 2010, 2010.
- [6] BP, BP Statistical Review of World Energy, 2011.
- [7] P.C.K. Vesborg, T.F. Jaramillo, RSC Adv. 2 (2012) 7933.
- [8] R. Smalley, MRS Bull. 30 (2005) 412.
- [9] N. Lewis, D. Nocera, Proc. Natl. Acad. Sci. U. S. A. 103 (2006) 15729.
- [10] IPCC - Core Writing Team, Climate Change 2007: Synthesis Report. Contribution of Working Groups I, II and III to the Fourth Assessment Report of the Intergovernmental Panel on Climate Change., Intergovernmental Panel on Climate Change, Geneva, Switzerland, 2008.
- [11] R. Quadrelli, S. Peterson, Energy Policy 35 (2007) 5938.
- [12] M.R. Raupach, G. Marland, P. Ciais, C. Le Quéré, J.G. Canadell, G. Klepper, C.B. Field, Proc. Natl. Acad. Sci. U. S. A. 104 (2007) 10288.
- [13] J. Hansen, M. Sato, R. Ruedy, a Lacis, V. Oinas, Proc. Natl. Acad. Sci. U. S. A. 97 (2000) 9875.
- [14] A. Gore, An Inconvenient Truth, Rodale, New York, 2006.

- [15] B. Jongman, S. Hochrainer-Stigler, L. Feyen, J.C.J.H. Aerts, R. Mechler, W.J.W. Botzen, L.M. Bouwer, G. Pflug, R. Rojas, P.J. Ward, *Nat. Clim. Chang.* advance on (2014).
- [16] F. Rizzi, N.J. van Eck, M. Frey, *Renew. Energy* 62 (2014) 657.
- [17] IEA, *Renewables in Global Energy Supply*, 2007.
- [18] K. Kaygusuz, *Energy Sources* 26 (2004) 215.
- [19] K. Marvel, B. Kravitz, K. Caldeira, *Nat. Clim. Chang.* 3 (2012) 118.
- [20] N.L. Panwar, S.C. Kaushik, S. Kothari, *Renew. Sustain. Energy Rev.* 15 (2011) 1513.
- [21] P.P. Edwards, V.L. Kuznetsov, W.I.F. David, N.P. Brandon, *Energy Policy* 36 (2008) 4356.
- [22] M. Zerta, P. Schmidt, C. Stiller, H. Landinger, *Int. J. Hydrogen Energy* 33 (2008) 3021.
- [23] J. Brouwer, *Curr. Appl. Phys.* 10 (2010) S9.
- [24] L. Howes, *Chem. World* 8 (2011) 44.
- [25] W.R. Grove, *London Edinburgh Philos. Mag. J. Sci.* 13 (1938) 430.
- [26] W.R. Grove, *London Edinburgh Philos. Mag. J. Sci.* 14 (1939) 127.
- [27] C.F. Schönbein, *London Edinburgh Philos. Mag. J. Sci.* 14 (1939) 43.
- [28] M. Pehnt, P. Mellwig, F. Steinborn, U. Lehr, C. Lutz, C. Pellingner, M. Steck, *Ökologische Und Ökonomische Analyse von Brennstoffzellen- Heizgeräten*, 2012.
- [29] J. Garche, *Encyclopedia of Electrochemical Power Sources*, Elsevier, Amsterdam, 2009.
- [30] A. Rabis, P. Rodriguez, T.J. Schmidt, *ACS Catal.* 2 (2012) 864.
- [31] A. Schenk, C. Grimmer, M. Perchthaler, S. Weinberger, B. Pichler, C. Heinzl, C. Scheu, F.-A. Mautner, B. Bitschnau, V. Hacker, *J. Power Sources* 266 (2014) 313.
- [32] A.B. Stambouli, *Renew. Sustain. Energy Rev.* 15 (2011) 4507.

- [33] P. Malacrida, Alloys of Pt and Rare Earths for the Oxygen Electroreduction Reaction, 2014.
- [34] J. Zhang, H. Zhang, J. Wu, J. Zhang, in: Pem Fuel Cell Test. Diagnosis, Elsevier B.V., Amsterdam, 2013, pp. 1–42.
- [35] C.H. Hamann, W. Vielstich, Elektrochemie, Wiley-VCH, Weinheim, 2005.
- [36] H.A. Gasteiger, S.S. Kocha, B. Sompalli, F.T. Wagner, Appl. Catal. B Environ. 56 (2005) 9.
- [37] J. Zhang, H. Zhang, J. Wu, J. Zhang, in: Pem Fuel Cell Test. Diagnosis, Elsevier B.V., Amsterdam, 2013, pp. 243–282.
- [38] J. Zhang, Z. Xie, J. Zhang, Y. Tang, C. Song, T. Navessin, Z. Shi, D. Song, H. Wang, D.P. Wilkinson, Z.-S. Liu, S. Holdcroft, J. Power Sources 160 (2006) 872.
- [39] J. Zhang, H. Zhang, J. Wu, J. Zhang, in: Pem Fuel Cell Test. Diagnosis, Elsevier B.V., Amsterdam, 2013, pp. 121–141.
- [40] X. Cheng, Z. Shi, N. Glass, L. Zhang, J. Zhang, D. Song, Z.-S. Liu, H. Wang, J. Shen, J. Power Sources 165 (2007) 739.
- [41] F. Jing, M. Hou, W. Shi, J. Fu, H. Yu, P. Ming, B. Yi, J. Power Sources 166 (2007) 172.
- [42] Y. Nagahara, S. Sugawara, K. Shinohara, J. Power Sources 182 (2008) 422.
- [43] R. Borup, E. Brosha, F. Garzon, B. Pivovar, T. Rockward, T. Springer, E. Al., Effects of Fuel and Air Impurities on PEM Fuel Cell Performance, 2007.
- [44] U. Izquierdo, V.L. Barrio, J.F. Cambra, J. Requies, M.B. Güemez, P.L. Arias, G. Kolb, R. Zapf, a. M. Gutiérrez, J.R. Arraibi, Int. J. Hydrogen Energy (2011) 1.
- [45] I.E.A.H.C.-O. Group, Hydrogen Production and Storage, Paris Cedex, 2006.
- [46] J. Zhang, Y. Tang, C. Song, J. Zhang, J. Power Sources 172 (2007) 163.
- [47] J. Jensen, Q. Li, C. Pan, A. Vestbo, K. Mortensen, H. Nybopetersen, C. Lausorensen, T. Nedergaardclausen, J. Schramm, N. Bjerrum, Int. J. Hydrogen Energy 32 (2007) 1567.

- [48] O.E. Kongstein, T. Berning, B. Børresen, F. Seland, R. Tunold, *Energy* 32 (2007) 418.
- [49] Q. Li, *Solid State Ionics* 168 (2004) 177.
- [50] H. Löhn, *Leistungsvergleich von Nieder- Und Hochtemperatur-Polymerelektrolytmembran-Brennstoffzellen - Experimentelle Untersuchungen, Modellierung Und Numerische Simulation*, 2010.
- [51] R. Bouchet, E. Siebert, *Solid State Ionics* 118 (1999) 287.
- [52] R. He, *J. Memb. Sci.* 226 (2003) 169.
- [53] R. He, Q. Li, *J. Polym. Sci. Part A Polym. Chem.* 45 (2007) 2989.
- [54] Y. Shao-Horn, W.C. Sheng, S. Chen, P.J. Ferreira, E.F. Holby, D. Morgan, *Top. Catal.* 46 (2007) 285.
- [55] S.M. Andersen, L. Grahl-Madsen, E.M. Skou, *Solid State Ionics* 192 (2010) 602.
- [56] K.J.J. Mayrhofer, K. Hartl, V. Juhart, M. Arenz, *J. Am. Chem. Soc.* 131 (2009) 16348.
- [57] S. Yin, S. Mu, H. Lv, N. Cheng, M. Pan, Z. Fu, *Appl. Catal. B Environ.* 93 (2010) 233.
- [58] W.R. Baumgartner, P. Parz, S. Fraser, E. Wallnöfer, V. Hacker, *J. Power Sources* 182 (2008) 413.
- [59] P.J. Ferreira, G.J. la O', Y. Shao-Horn, D. Morgan, R. Makharia, S. Kocha, H.A. Gasteiger, *J. Electrochem. Soc.* 152 (2005) A2256.
- [60] A.S. Aricò, A. Stassi, I. Gatto, G. Monforte, E. Passalacqua, V. Antonucci, *J. Phys. Chem. C* 114 (2010) 15823.
- [61] A.S. Aricò, A. Stassi, E. Modica, R. Ornelas, I. Gatto, E. Passalacqua, V. Antonucci, *J. Power Sources* 178 (2008) 525.
- [62] Y. Zhai, H. Zhang, D. Xing, Z.-G. Shao, *J. Power Sources* 164 (2007) 126.
- [63] M. Perchthaler, T. Ossiander, V. Juhart, J. Mitzel, C. Heinzl, C. Scheu, V. Hacker, *J. Power Sources* 243 (2013) 472.
- [64] T. Zhu, C. Du, C. Liu, G. Yin, P. Shi, *Appl. Surf. Sci.* 257 (2011) 2371.

- [65] P. Sabatier, *Berichte Der Dtsch. Chem. Gesellschaft* 44 (1911) 1984.
- [66] J. Greeley, I.E.L. Stephens, A.S. Bondarenko, T.P. Johansson, H.A. Hansen, T.F. Jaramillo, J. Rossmeisl, I. Chorkendorff, J.K. Nørskov, *Nat. Chem.* 1 (2009) 552.
- [67] J. Rossmeisl, G.S. Karlberg, T.F. Jaramillo, J.K. Nørskov, *Faraday Discuss.* 140 (2009) 337.
- [68] J.K. Nørskov, J. Rossmeisl, A. Logadottir, L. Lindqvist, J.R. Kitchin, T. Bligaard, H. Jónsson, *J. Phys. Chem. B* 108 (2004) 17886.
- [69] P. Strasser, S. Koh, T. Anniyev, J. Greeley, K. More, C. Yu, Z. Liu, S. Kaya, D. Nordlund, H. Ogasawara, M.F. Toney, A. Nilsson, *Nat. Chem.* 2 (2010) 454.
- [70] G.S. Karlberg, J. Rossmeisl, J.K. Nørskov, *Phys. Chem. Chem. Phys.* 9 (2007) 5158.
- [71] I.E.L. Stephens, A.S. Bondarenko, U. Grønberg, J. Rossmeisl, I. Chorkendorff, *Energy Environ. Sci.* 5 (2012) 6744.
- [72] M. Escudero-Escribano, A. Verdaguier-Casadevall, P. Malacrida, U. Grønberg, B.P. Knudsen, A.K. Jepsen, J. Rossmeisl, I.E.L. Stephens, I. Chorkendorff, *J. Am. Chem. Soc.* 134 (2012) 16476.
- [73] V.R. Stamenkovic, B.S. Mun, M. Arenz, K.J.J. Mayrhofer, C.A. Lucas, G. Wang, P.N. Ross, N.M. Markovic, *Nat. Mater.* 6 (2007) 241.
- [74] J.R. Kitchin, J.K. Nørskov, M.A. Barteau, J.G. Chen, *J. Chem. Phys.* 120 (2004) 10240.
- [75] V.R. Stamenkovic, B. Fowler, B.S. Mun, G. Wang, P.N. Ross, C.A. Lucas, N.M. Marković, *Science* 315 (2007) 493.
- [76] T. Toda, H. Igarashi, H. Uchida, M. Watanabe, *J. Electrochem. Soc.* 146 (1999) 3750.
- [77] X. Liu, G. Fu, Y. Chen, Y. Tang, P. She, T. Lu, *Chemistry* 20 (2014) 585.
- [78] G. Fu, K. Wu, J. Lin, Y. Tang, Y. Chen, Y. Zhou, T. Lu, *J. Phys. Chem. C* 117 (2013) 9826.
- [79] E. Antolini, T. Lopes, E.R. Gonzalez, *J. Alloys Compd.* 461 (2008) 253.

- [80] B.C. Beard, P.N. Ross, *J. Electrochem. Soc.* 137 (1990) 3368.
- [81] V.R. Stamenkovic, T.J. Schmidt, P.N. Ross, N.M. Markovic, *J. Phys. Chem. B* 106 (2002) 11970.
- [82] N.M. Markovic, T.J. Schmidt, V.R. Stamenkovic, P.N. Ross, *Fuel Cells* 1 (2001) 105.
- [83] J. Salgado, E. Antolini, E. Gonzalez, *J. Power Sources* 141 (2005) 13.
- [84] J.R.C. Salgado, E. Antolini, E.R. Gonzalez, *J. Power Sources* 138 (2004) 56.
- [85] T. Lopes, E. Antolini, F. Colmati, E.R. Gonzalez, *J. Power Sources* 164 (2007) 111.
- [86] E. Antolini, J.R.C. Salgado, E.R. Gonzalez, *J. Electroanal. Chem.* 580 (2005) 145.
- [87] I. Spanos, J.J.K. Kirkensgaard, K. Mortensen, M. Arenz, *J. Power Sources* 245 (2014) 908.
- [88] K. Jayasayee, J.A.R. Van Veen, T.G. Manivasagam, S. Celebi, E.J.M. Hensen, F.A. de Bruijn, *Appl. Catal. B Environ.* 111-112 (2012) 515.
- [89] S. Koh, P. Strasser, *J. Am. Chem. Soc.* 129 (2007) 12624.
- [90] V.R. Stamenkovic, B.S. Mun, K.J.J. Mayrhofer, P.N. Ross, N.M. Markovic, *J. Am. Chem. Soc.* 128 (2006) 8813.
- [91] D.F. van der Vliet, C. Wang, D. Li, A.P. Paulikas, J. Greeley, R.B. Rankin, D. Strmcnik, D. Tripkovic, N.M. Markovic, V.R. Stamenkovic, *Angew. Chem. Int. Ed. Engl.* 51 (2012) 3139.
- [92] I.E.L. Stephens, A.S. Bondarenko, U. Grønbjerg, J. Rossmeisl, I. Chorkendorff, *Energy Environ. Sci.* 5 (2012) 6744.
- [93] Y. Xu, A. V. Ruban, M. Mavrikakis, *J. Am. Chem. Soc.* 126 (2004) 4717.
- [94] V. Stamenkovic, B.S. Mun, K.J.J. Mayrhofer, P.N. Ross, N.M. Markovic, J. Rossmeisl, J. Greeley, J.K. Nørskov, *Angew. Chemie* 45 (2006) 2897.
- [95] S.J. Hwang, S.-K. Kim, J.-G. Lee, S.-C. Lee, J.H. Jang, P. Kim, T.-H. Lim, Y.-E. Sung, S.J. Yoo, *J. Am. Chem. Soc.* 134 (2012) 19508.

- [96] I.E.L. Stephens, A.S. Bondarenko, F.J. Perez-Alonso, F. Calle-Vallejo, L. Bech, T.P. Johansson, A.K. Jepsen, R. Frydendal, B.P. Knudsen, J. Rossmeisl, I. Chorkendorff, *J. Am. Chem. Soc.* 133 (2011) 5485.
- [97] B. Cordero, V. Gómez, A.E. Platero-Prats, M. Revés, J. Echeverría, E. Cremades, F. Barragán, S. Alvarez, *Dalton Trans.* (2008) 2832.
- [98] M. Nesselberger, S. Ashton, J.C. Meier, I. Katsounaros, K.J.J. Mayrhofer, M. Arenz, *J. Am. Chem. Soc.* 133 (2011) 17428.
- [99] C. Grimmer, *Activity and Stability Enhancement of Platinum Cobalt Catalysts for HTPEM Fuel Cells*, Graz University of Technology, 2013.
- [100] C. Wang, D. van der Vliet, K.L. More, N.J. Zaluzec, S. Peng, S. Sun, H. Daimon, G. Wang, J. Greeley, J. Pearson, A.P. Paulikas, G. Karapetrov, D. Strmcnik, N.M. Markovic, V.R. Stamenkovic, *Nano Lett.* 11 (2011) 919.
- [101] C. Wang, M. Chi, D. Li, D. Strmcnik, D. van der Vliet, G. Wang, V. Komanicky, K.-C. Chang, A.P. Paulikas, D. Tripkovic, J. Pearson, K.L. More, N.M. Markovic, V.R. Stamenkovic, *J. Am. Chem. Soc.* 133 (2011) 14396.
- [102] R.W.G. Wyckoff, *The Structure of Crystals.*, Vol.1, 2nd ed., Interscience Publishers, New York, 1963.
- [103] G. Cliff, G.W. Lorimer, *J. Microsc.* 103 (1975) 203.
- [104] H.E. Swanson, E. Tatge, *Natl. Bur. Stand. Circ.* 539 (1953) 1.
- [105] P. Scherrer, *Nachrichten von Der Gesellschaft Der Wissenschaften ...* 26 (1918) 98.
- [106] A.S. Darling, *Platin. Met. Rev.* (1963) 96.
- [107] E.I. Santiago, L.C. Varanda, H.M. Villullas, *J. Phys. Chem. C* 111 (2007) 3146.
- [108] E.A. Owen, D. Madoc Jones, *Proc. Phys. Soc. Sect. B* 67 (1954) 456.
- [109] B. Pichler, *Synthesis of PtFe/C Catalysts for the Oxygen Reduction Reaction in High-Temperature PEM Fuel Cells*, 2014.
- [110] Y. Garsany, O.A. Baturina, K.E. Swider-Lyons, S.S. Kocha, *Anal. Chem.* 82 (2010) 6321.

- [111] Y. Garsany, I.L. Singer, K.E. Swider-Lyons, *J. Electroanal. Chem.* 662 (2011) 396.
- [112] K.J.J. Mayrhofer, D. Strmcnik, B.B. Blizanac, V.R. Stamenkovic, M. Arenz, N.M. Markovic, *Electrochim. Acta* 53 (2008) 3181.
- [113] J. Schumpeter, *Capitalism, Socialism and Democracy*, rev. Ed., Routledge, London, 1942.
- [114] L. Xiong, A. Manthiram, *Electrochim. Acta* 50 (2005) 2323.
- [115] M.E. Orazem, B. Tribollet, *Electrochemical Impedance Spectroscopy*, John Wiley & Sons, Inc., Hoboken, New Jersey, 2008.
- [116] S.M. Rezaei Niya, M. Hoorfar, *J. Power Sources* 240 (2013) 281.
- [117] D.D. Macdonald, *Electrochim. Acta* 51 (2006) 1376.
- [118] J. Jespersen, E. Schaltz, S. Kær, *J. Power Sources* 191 (2009) 289.
- [119] S. Weinberger, *Elektrochemische Charakterisierung Bifunktionaler Gasdiffusionselektroden Für Elektrisch Wiederaufladbare Zink-Luft Zellen*, 2012.
- [120] X. Yuan, H. Wang, J.C. Sun, J. Zhang, *Int. J. Hydrogen Energy* 32 (2007) 4365.
- [121] T.J.P. Freire, E.R. Gonzalez, *J. Electroanal. Chem.* 503 (2001) 57.
- [122] W.H. Zhu, R.U. Payne, B.J. Tatarchuk, *J. Power Sources* 168 (2007) 211.
- [123] X. Yuan, J.C. Sun, M. Blanco, H. Wang, J. Zhang, D.P. Wilkinson, *J. Power Sources* 161 (2006) 920.
- [124] S. Kamarajugadda, S. Mazumder, *J. Power Sources* 208 (2012) 328.
- [125] L. Vegard, *Zeitschrift Für Phys.* 5 (1921) 17.

7 Appendix

7.1 Abbreviations

AFC	...	Alkaline fuel cell
AST	...	Accelerated stress test
AC	...	Alternating current
BoL	...	Begin of lifetime
CHP	...	Combined heat and power
CV	...	Cyclic voltammetry
DMAc	...	Dimethylacetamide
DMFC	...	Direct methanol fuel cell
EC	...	Equivalent circuit
ECSA	...	Electrochemical active surface area
EDX	...	Energy dispersive X-ray
EG	...	Ethylene glycol
EIS	...	Electrochemical impedance spectroscopy
Eq.	...	Equation
GC	...	Glassy carbon
GDE	...	Gas diffusion electrode
GHG	...	Greenhouse gases
HOR	...	Hydrogen oxidation reaction
HR	...	High resolution
HT	...	High temperature
H _{upd}	...	Hydrogen under potentially deposited
ICE	...	Internal combustion engine

LT	...	Low temperature
MCFC	...	Molten carbonate fuel cell
MA	...	Mass activity
MEA	...	Membrane electrode assembly
OCV	...	Open circuit voltage
ORR	...	Oxygen reduction reaction
PAFC	...	Phosphoric acid fuel cell
PBI	...	Polybenzimidazole
PEM	...	Polymer electrolyte membrane, proton exchange membrane
PEMFC	...	Polymer electrolyte membrane fuel cell, proton exchange membrane fuel cell
PFSA	...	Perfluorosulphonic acid polymer
PTFE	...	Polytetrafluoroethylene
Pt-M	...	Platinum transition metal catalyst
Pt-M/C	...	Carbon supported platinum transition metal catalyst
RDE	...	Rotating disk electrode
RHE	...	Reversible hydrogen electrode
SCD	...	Specific current density
SOFC	...	Solid oxide fuel cell
STEM	...	Scanning transmission electron microscopy
TEM	...	Transmission electron microscopy
VI	...	Voltage-current
XRD	...	X-ray diffraction

7.2 List of figures

Figure 1: Global warming and causal connection to increasing CO ₂ emissions and increasing global population. a) global land and ocean temperature index [1], b) global temperature (meteorological stations) [1], c) global fossil fuel CO ₂ emissions (the insert shows the increase of CO ₂ emissions from 1880-2014) [2], and d) global population (the insert shows the increase of population from 1880-2014) [3,4].....	19
Figure 2: a) World primary energy supply 2011, shares of fuels [6,7,11], b) origin and share of anthropogenic GHG emissions [11], c) global CO ₂ anthropogenic emissions by fossil fuels [5], and d) shares of different GHG emitted by energy production and consumption [11].	20
Figure 3: Scheme of a PEMFC	33
Figure 4: Influence of different loss mechanisms on the VI-characteristic of a PEM fuel cell. Figure adapted from [36].	36
Figure 5: Langmuir-type adsorption of hydrogen and carbon monoxide on platinum as a function of the temperature. Adopted from [37].....	39
Figure 6: Smart heating system for single-family households based on natural gas reforming and HT-PEM fuel cell technology. This picture has been provided by elcore and elcomax GmbH.	42
Figure 7: Chemical structure of Polybenzimidazole.....	43
Figure 8: Structure of phosphoric acid-doped Polybenzimidazole.	43
Figure 9: Proposed proton conduction mechanism (proton hopping). Figure adapted from [50–53].....	44
Figure 10: Activity of pure metals towards oxygen reduction reaction described in form of a volcano plot. Adapted from [68].....	47
Figure 11: Description of the UI-characteristics of a state-of-the-art PEM fuel cell using a Pt/C catalyst at both electrodes. The figure is adapted from [36].....	48

Figure 12: Reaction coordinates for the oxygen reduction reaction, a) dissociative and b) associative mechanism at different potentials and having different oxygen coverage at the Pt (111) catalyst surface. Adapted from [68].	49
Figure 13: Reaction coordinate for the oxygen reduction reaction following the associative mechanism at a potential of 0.9 V _{RHE} at the Pt (111) catalyst surface. Adapted from [67].	50
Figure 14: A combined experimental and theoretical ORR volcano described by the difference in oxygen binding energy of the Pt-alloys in comparison to pure Pt. Figure adapted from [73]	52
Figure 15: Preparation of the gas diffusion electrodes in a roll-to-roll production process at elcomax GmbH. a) Carbon cloth, b) applying of HSAC slurry, c) doctor blading of the HSAC slurry and d) final gas diffusion electrodes after drying. All pictures are provided by elcomax GmbH.	57
Figure 16: Preparation of the Pt-Co/C catalysts. a) GDE sheet, b) GDE pads for optimisation of the catalyst preparation, c) impregnation solution and d) impregnation of larger electrode sheets at elcomax GmbH. Figures c) and d) are provided by elcomax GmbH.	58
Figure 17: Schematic drawing of the nanoparticle synthesis.	59
Figure 18: High-Resolution TEM images of the prepared Pt-Co/C catalysts before leaching and heat treatment (a) and afterwards (b). The insets show the electron diffraction patterns of the crystalline catalysts particles. The indicated d-values are given in Å. Both images have been published in Ref. [31].	62
Figure 19: EDX spectra from Pt-Co/C catalyst samples before (a) and after leaching (b).	63
Figure 20: X-ray diffraction patterns of the untreated, leached, the leached and heat treated Pt-Co/C catalysts and the Pt/C catalysts [31].	65
Figure 21: 3-electrode set-up for ex-situ electrochemical studies of the Pt-Co/C catalysts.	67

Figure 22: A homogeneous catalyst film after pipetting the catalyst dispersion onto the RDE tip. The image was provided by elcomax GmbH.....	68
Figure 23: Effect of catalyst thin-film quality on cyclic voltammetry in inert electrolyte (a) and oxygen reduction reaction polarisation (b). Adapted from <i>Garsany et al.</i> [110].....	69
Figure 24: Influence of the applied corrections on the oxygen reduction reaction.....	71
Figure 25: Cyclic voltammogram of the Pt-Co/C catalyst directly after reduction of the precursor metal salts.....	73
Figure 26: ORR polarisation curves and corresponding Tafel plots of the untreated Pt-Co/C and the commercial Pt/C catalyst recorded at a scan rate of 50 mV s ⁻¹ in 0.1 M HClO ₄ electrolyte.....	74
Figure 27: Cyclic voltammograms of the untreated Pt-Co/C catalyst (a), and the Pt/C catalyst (b) recorded at a scan rate of 50 mV s ⁻¹ in nitrogen saturated 0.1 M HClO ₄ electrolyte. The gradual degradation of the catalysts during AST cycling is given after 555, 1110 and 1665 cycles in form of the loss of ECSA [31].....	75
Figure 28: Comparison of the cyclic voltammograms of the untreated and the leached Pt-Co/C catalysts recorded at a scan rate of 50 mV s ⁻¹ in nitrogen saturated 0.1 M HClO ₄ electrolyte.....	76
Figure 29 ORR polarisation curves and corresponding Tafel plots of the leached Pt-Co/C and the commercial Pt/C catalyst recorded at a scan rate of 50 mV s ⁻¹ in 0.1 M HClO ₄ electrolyte.....	77
Figure 30: Cyclic voltammogram of the leached Pt-Co/C catalyst recorded at a scan rate of 50 mV s ⁻¹ in nitrogen saturated 0.1 M HClO ₄ electrolyte. The gradual degradation of the catalyst during AST cycling is given after 555, 1110 and 1665 cycles in form of the loss of ECSA [31].....	78
Figure 31: Cyclic voltammograms of the as-prepared Pt-Co/C catalysts recorded at a scan rate of 50 mV s ⁻¹ in nitrogen saturated 0.1 M HClO ₄ electrolyte [31].....	79

Figure 32: (a) Comparison of the ORR polarisation curves of the as-prepared Pt-Co/C catalysts and the Pt/C catalyst, recorded at a scan rate of 50 mV s ⁻¹ in oxygen saturated 0.1 M HClO ₄ electrolyte with a rotation speed of 1600 rpm. (b) Corresponding Tafel plots [31].	80
Figure 33: Cyclic voltammograms of the leached and heat treated Pt-Co/C catalyst recorded at a scan rate of 50 mV s ⁻¹ in nitrogen saturated 0.1 M HClO ₄ electrolyte. The gradual degradation of the catalysts during AST cycling is given after 555, 1110 and 1665 cycles in form of the loss of ECSA [31].	81
Figure 34: Membrane fabrication: a) m-PBI powder, b) casting machine and c) final membrane. Pictures were provided by elcomax GmbH.	83
Figure 35: a) Manual assembling of the MEA, placing the membrane on the anode catalyst layer, b) final MEAs in different sizes, small for single cell measurements only, big for single cell and stack test. Pictures were provided by elcomax GmbH.	84
Figure 36: Small HT-PEM fuel cell set-up: a) assembled fuel cell, b) serpentine flow field. Pictures were provided by elcomax GmbH.	85
Figure 37: HT-PEM fuel cell stack from elcomax GmbH photographed from different angles and perspectives. Pictures were provided by elcomax GmbH.	86
Figure 38: Polarisation curves and power densities of the leached and heat treated Pt-Co/C based HT-PEM MEA before and after 600 h long term operation and the commercial HT-PEM MEA under constant load of 0.2 A cm ⁻² at 160 °C, fuelled with hydrogen (a) and synthetic reformat (b) at the anode and air at the cathode [31].	87
Figure 39: Comparison of cell voltages and the corresponding 1 kHz AC resistances of the leached and heat treated Pt-Co/C based HT-PEM MEA and a commercial HT-PEM MEA during durability testing at 160 °C. The insert shows the first 14 h of the long term operation of the in-house prepared MEA [31].	89
Figure 40: a) Applied equivalent circuit for fitting procedure, b) and c) the corresponding ECs after both simplification steps [31].	92

Figure 41: Nyquist plots of the EIS measurements of the leached and heat treated Pt-Co/C based HT-PEM MEA at BoL and after 600 h of operation.	92
Figure 42: Nyquist plots of the EIS measurements of the leached and heat treated Pt-Co/C based HT-PEM MEA at BoL and after 600 h of operation and the corresponding fits [31].	94
Figure 43: Cyclic voltammograms of the cathode layer of the leached and heat treated Pt-Co/C based HT-PEM MEA before and after long term operation test, recorded at a scan rate of 50 mV s ⁻¹ . The anode (fed with dry hydrogen) was used as pseudo-reference electrode. The cathode was supplied with humidified nitrogen [31].	97
Figure 44: In-situ HT-PEM fuel cell accelerated stress test of the Pt-Co/C catalysts.	99
Figure 45: Zoom of the different phases of the in-situ AST.	99
Figure 46: In-situ HT-PEM fuel cell accelerated stress test of the Pt-Co/C catalysts after refined preparation.	101
Figure 47: Long term operation of 3 Pt-Co/C based HT-PEM MEAs in a HT-PEM fuel cell stack test.....	103
Figure 48: Comparison of the standard Pt/C and the Pt-Co/C based MEAs during long term HT-PEM stack operation. The mean cell voltages of 3 Pt-Co/C and 3 Pt/C MEAs are depicted.	104
Figure 49: Long term HT-PEM in-situ AST of the Pt-Co/C based MEA in stack operation.	105
Figure 50: Determination the charge of the H _{upd} peak.....	118

7.3 List of tables

Table 1: Prioritised ranking of the most critical global problems for the next 100 years [8].	22
Table 2: Summary of fuel cell types [21].	28
Table 3: The theoretical cell voltage depending on the total reaction enthalpy.	37
Table 4: Summary of the properties of the differently treated Pt-Co/C catalysts and the commercial Pt/C catalyst obtained from XRD measurements. The amounts (at.%) of Co refer to lattice parameter of the Pt/C sample of 0.39147(7) nm and metallic Pt [104], respectively [31].	66
Table 5: Common electrical elements in EC analysis and their corresponding impedances [119].	91
Table 6: Electrical elements for electrochemical impedance spectroscopy and their description [119].	91
Table 7: Parameters obtained by the EC fitting procedure (*: fixed parameters) [31].	95
Table 8: The ECSA increase vs. the increase of the kinetic conductance ($S_{kin} = 1/R_{kin}$) [31].	96
Table 9: Summary of performed electrochemical measurement procedures.	117

7.4 Publication



Platinum–cobalt catalysts for the oxygen reduction reaction in high temperature proton exchange membrane fuel cells – Long term behavior under ex-situ and in-situ conditions



Alexander Schenk^{a,*}, Christoph Grimmer^a, Markus Perchthaler^{a,b}, Stephan Weinberger^a, Birgit Pichler^a, Christoph Heinzl^c, Christina Scheu^c, Franz-Andreas Mautner^d, Brigitte Bitschnau^d, Viktor Hacker^a

^a Institute of Chemical Engineering and Environmental Technology, Fuel Cell Systems Group, Graz University of Technology, Steyrergasse 21, Graz 8010, Austria

^b elcomax GmbH, Bayerwaldstraße 3, Munich 81737, Germany

^c Department of Chemistry, Ludwig-Maximilians-University Munich, Butenandtstr. 11, Munich 81377, Germany

^d Institute of Physical and Theoretical Chemistry, Structure Science Group, Graz University of Technology, Stremayrgasse 9, Graz 8010, Austria

H I G H L I G H T S

- Platinum cobalt catalysts are synthesized by a scalable straightforward process.
- Stability increasing post-preparation treatments are developed and optimized.
- RDE experiments and HT-PEM single cell tests are conducted.
- Platinum loading is reduced without loss of performance and durability.

A R T I C L E I N F O

Article history:

Received 11 December 2013

Received in revised form

7 April 2014

Accepted 5 May 2014

Available online 17 May 2014

Keywords:

PEMFCs

High temperature

ORR catalysts

Pt catalysts

Long term operation

Stability

A B S T R A C T

Platinum cobalt catalysts (Pt–Co) have attracted much interest as cathode catalysts for proton exchange membrane fuel cells (PEMFCs) due to their high activity toward oxygen reduction reaction (ORR). Many of the reported catalysts show outstanding performance in ex-situ experiments. However, the laborious synthesis protocols of these Pt–Co catalysts disable an efficient and economic production of membrane electrode assemblies (MEAs). We present an economic, flexible and continuous Pt–M/C catalyst preparation method as part of a large scale membrane electrode assembly manufacturing. In comparison, the as-prepared Pt–Co/C based high temperature (HT)-PEM MEA showed an equal performance to a commercially available HT-PEM MEA during 600 h of operation under constant load, although the commercial one had a significantly higher Pt loading at the cathode.

© 2014 Elsevier B.V. All rights reserved.

1. Introduction

Proton exchange membrane fuel cell (PEMFC) technology enables clean and efficient energy conversion with high energy density and is therefore considered to be a key source of power in a future society based on renewable and sustainable energy. So far, this promising technology has not yet penetrated the market to compete with conventional power sources.

Platinum offers the highest catalytic activity toward oxygen reduction reaction (ORR) of any pure metals. But nevertheless the ORR activity on Pt is too slow for an efficient operation of fuel cells.

* Corresponding author. Tel.: +43 316 873 8783; fax: +43 316 873 8782.

E-mail addresses: alexander.schenk@tugraz.at (A. Schenk), christoph.grimmer@tugraz.at (C. Grimmer), Markus.Perchthaler@elcomax.com (M. Perchthaler), stephan.weinberger@tugraz.at (S. Weinberger), birgit.pichler@tugraz.at (B. Pichler), Christoph.Heinzl@cup.uni-muenchen.de (C. Heinzl), Christina.Scheu@cup.uni-muenchen.de (C. Scheu), mautner@tugraz.at (F.-A. Mautner), bitschnau@tugraz.at (B. Bitschnau), viktor.hacker@tugraz.at (V. Hacker).

Due to kinetic limitations, at present, PEMFCs require relatively high loadings of platinum. It has been shown, that the anode loading could be reduced from 0.1 to 0.05 mg cm⁻² [1,2]. However, at the cathode, 0.4 mg cm⁻² are required to compensate the high overpotential losses of the ORR [1,3,4]. Considering state-of-the-art high temperature PEM fuel cell technology even higher Pt loadings are used. Recent developments led to a reduction of the Pt loading at the anode to 0.9 mg cm⁻², whereas the cathode still required 1.7 mg cm⁻² [5].

Over the last two decades substantial efforts have been dedicated to find new catalyst systems for fuel cells. As the replacement of Pt by catalysts made of abundant elements, which show ORR activities close to that of Pt, faces several challenges, such as long term stability in acidic media, most of the research work focusses on improving the ORR activity of Pt in fuel cells [1,3,6–12]. By using an appropriate combination of platinum with other metals (e.g. Pd, Ru, V, Cr, Co, Ni, Cu etc.) it is possible to increase the activity toward ORR significantly and hence reduce the Pt loading at the cathode [1,3,13–23]. In particular the formation of platinum alloys with late transition metals such as Co has been investigated extensively [17,21–29]. The reported Pt–Co catalysts show an increased activity toward ORR compared to pure Pt. Whereby this enhancement of the electrocatalytic ORR activity of these catalysts is related to the weaker binding of the surface to ORR intermediates, e.g. HO* [1,3,4,14–17,23].

Although these Pt–M catalysts offer several advantages for PEMFC technology, there are further improvements to be achieved. Especially the highly corrosive conditions in PEM fuel cells result in gradual dissolution of the transition metal, the agglomeration of platinum or its loss to the electrolyte and consequently to a loss of power density [1,3,29–33]. Hence, the combination of advanced catalyst development, functionalization of support materials, appropriate membrane manufacturing and the methods of their composition lay the foundation for a large-scale catalyst and membrane electrode assembly production and is the crucial step toward commercialization of fuel cell technology.

In literature many approaches and methods can be found for the synthesis of carbon supported platinum alloy nanoparticles Pt–M/C. In order to keep an easily up-scalable production process in mind, it is most likely to use solution-based chemical approaches, such as impregnation. For impregnation metal precursor salts are dissolved in an appropriate solvent and then merged with a suitable support material, usually high surface area carbon (HSAC). The precursor solution wets the pores of the support material by capillary forces. The product is dried afterwards to remove excess solvent, heated and finally reduced to give the corresponding metals. In order to increase the reaction rate and to directly convert the metal salts into metallic nanoparticles a reducing agent, e.g. ethylene glycol, is added to the impregnation solution. Additionally, the as-prepared catalysts can be leached in acid solution to remove the inactive transition metal from the catalysts surface, leading to a so-called Pt-skeleton surface [1,14,28,33]. A heat treatment of the Pt–M/C catalysts, depending on the temperature, can either be used to decompose any undesired organic residues or to rearrange the positioning of Pt and M within the catalysts [28,34]. Due to the lower surface energy of Pt, in comparison to the transition metal in inert atmosphere, platinum migrates to the catalysts surface, leading to a so-called Pt-skin structure [1,14,28,33]. Both processes, leaching and heat treatment, form a Pt overlayer at the surface of the Pt–M catalysts and induce through strain and ligand effects a weakening of the binding of ORR intermediates at the Pt surface, hence leading to a higher activity toward ORR [1,33]. Furthermore, the Pt overlayer renders the Pt–M catalysts kinetically stable against dissolution of the solute transition metal under the acidic and oxidizing environment of the (HT-)PEM fuel cell cathode [1,33].

In this paper we present an economic, flexible and continuous Pt–M/C catalyst preparation as part of a large scale MEA manufacturing. The given MEA manufacturing process consists of the following production steps: (i) deposition of high surface area carbon (HSAC) on carbon paper, (ii) impregnation with metal salt containing solutions, (iii) reduction of the precursor salts, (iv) stabilization of the Pt–M catalysts, (v) doping with phosphoric acid and (vi) assembling of the MEA.

The focus of our work was set on the establishment of an active and stable catalyst system, which opens up the possibility for the reduction of the precious metal loading, thus a cost reduction of a state-of-the-art membrane electrode assembly. Every single step of the MEA manufacturing has been designed to fit into a continuous production process, such as roll-to-roll production. The continuous deposition of the catalysts directly in the, for HT PEM usage optimized, porous layer of the gas diffusion electrode leads to a better utilization of Pt. In contrast, conventional impregnation of catalysts onto HSAC and casting it afterwards onto the gas diffusion layer leads to a higher loss of Pt during the production and therefore to a more expensive process. Furthermore, Pt can be enclosed in carbon aggregates during conventional deposition and is therefore lost for the electrocatalytic reactions. The herein presented continuous MEA fabrication is much more time and cost saving, since batch processes, such as conventional loading of the HSAC, filtering or centrifugation, multiple washing, drying and annealing steps in tube furnaces, are eliminated. Moreover, the scrap, which could be produced during the manufacturing of the porous layer, has no expensive catalyst in it. So, higher scrap rates can be accepted.

2. Experimental

2.1. Preparation of gas diffusion electrodes

The catalyst support (turbostratic (t-carbon or disordered graphite) HSAC, BET: 250–300 m² g⁻¹) material with PTFE as hydrophobic binder material was applied on a wet proofed carbon based gas diffusion layer via a doctor blade process. The catalyst support slurry consists of the HSAC, a PTFE dispersion (Dyneon™, TF 5035 PTFE), deionized water and 2-propanol (gradient grade, Merck). The gap of the doctor blade was adjusted to 610 μm to get an optimal loading of carbon/PTFE on the gas diffusion layer. The prepared gas diffusion electrode (GDE) was dried at 170 °C under constant air flow.

2.2. Catalyst preparation

All chemicals were used as purchased without further purification.

An optimized deposition of the nanocrystalline platinum cobalt catalysts supported on HSAC (Pt–Co/C) was obtained by adjusting the composition of the precursor solution, the reducing atmosphere, the temperature and the atomic ratio of platinum and cobalt salts as a function of each other, respectively. The impregnation solution was drop-coated on previously fabricated GDE sheets, resulting in a platinum loading of 1.00 mg cm⁻². In order to achieve a cheap and easy deposition of the catalysts, we obtained best results with an impregnation solution, having a Pt:Co ratio of 1:5. The solution contained hexachloroplatinic acid (H₂PtCl₆*6H₂O, Sigma–Aldrich), cobalt nitrate (Co(NO₃)₂*6H₂O, Sigma–Aldrich), ethylene glycol (EG, Carl Roth) as reducing agent and 2-propanol (Sigma–Aldrich)/ultrapure water (18.1 MΩ cm, Barnstead nanopure) (1:1) as solvent. Furthermore, activity and stability enhancing treatment of the active catalyst layer includes the addition of a non-ionic surfactant (Brij-30, Sigma–Aldrich) to the precursor solution to prevent the nanoparticles from agglomeration during the reduction

step, acid leaching and annealing steps after reduction [35]. The reduction of the deposited metal salts was initiated by a mild thermal treatment at 240 °C in nitrogen atmosphere. Conducted post-preparation treatments of Pt:Co 1:5 catalysts and their combinations are given in Table 1.

A commercially available Pt/C catalyst sample was obtained from elcomax GmbH and used as reference.

2.3. MEA preparation

After the deposition of the cathode catalysts on the GDE as described above, the HT-PEM MEAs were manufactured by doping the catalyst layer with a mixture of phosphoric acid (85 wt.%) and 1-pentanol. After evaporation of 1-pentanol at 230 °C, the electrodes were hot pressed with a membrane based on polybenzimidazole (PBI) at 150 °C to form the membrane electrode assembly.

The membranes were casted from a solution based on PBI and dimethylacetamide (N,N-DMAC, synthesis grade, Merck). Therefore meta-PBI powder was dissolved in DMAC under stirring for 3 h at 200 °C under pressure. All chemicals were used as purchased without further purification. The membranes were casted by solvent evaporation at 70–100 °C on a carrier foil. Afterwards, a thermal treatment of the membranes, to remove DMAC residues, was performed.

For the anode a standard Pt based GDE from elcomax GmbH was used. The reference HT-PEM MEA was also obtained from elcomax GmbH.

2.4. Structural and chemical analysis

A FEI Titan 80 – 300 scanning transmission electron microscope (STEM) equipped with an EDAX energy dispersive X-ray spectroscopy (EDX) detector for analytical measurements was used for the investigation of the catalysts nanoparticles. The measurements were performed at 300 kV. The electrode material was suspended in 2-propanol/water (1:1), ultrasonicated for 10 min and one droplet of the suspension was dripped on a holey carbon coated nickel grid. The crystal structure was determined via electron diffraction patterns measured over several nanoparticles and by analyzing high resolution TEM micrographs. In addition, the size and distribution of the catalyst particles was determined by TEM.

X-ray powder diffraction profiles were obtained on a Bruker AXS D8 Advance powder diffractometer in Bragg-Brentano θ - θ geometry operated at 40 kV and 40 mA, using Cu K_{α} radiation ($\lambda = 1.54178 \text{ \AA}$). The 2θ diffraction angles were measured by scanning the goniometer from 30 to 138° 2θ having a step size of 0.025° 2θ . The profile-fit was performed using PANalytical X'Pert High Score Plus software using the crystal structure data of metallic Pt [36] and Co [37]. Calculations using Vegard's law [38] support the observed shifts in the peaks when compared to those for pure Pt and Co. The average primary crystallite sizes of the samples (d_{xRD}) were determined according to the broadening of the diffraction peaks using the Scherrer relationship [39]

($d_{xRD} = (K\lambda) / \Delta(2\theta) \cos\theta$) where d is the mean crystallite dimension, K is the shape factor (0.9), λ is the X-ray wavelength in nm, $\Delta(2\theta)$ is the peak broadening at full width at half-maximum in radians and θ is the Bragg angle.

2.5. Electrochemical studies

Electrochemical studies were conducted in 0.1 M HClO₄ as electrolyte at room temperature and in a 50 cm² HT-PEMFC single cell at 160 °C, respectively. Ex-situ characterization served for preliminary evaluation and screening of the catalysts; whereas, in-situ studies were carried out using the most auspicious formulation.

2.5.1. Ex-situ characterization

All glassware was cleaned for 24 h in sulfuric acid solution, followed by heating and rinsing with ultrapure water to remove sulfate residues. The electrochemical experiments were carried out using an Autolab PGSTAT302N potentiostat (Metrohm Autolab B.V.), controlled by a computer. The rotating disc electrode (RDE) assembly was a combination of a rotator and an electrode from Pine Instruments Company (AFE5T050GC). Prior to electrode preparation, the glassy carbon rotating electrode disc was polished to a mirror finish using a 0.05 μm alumina suspension (MasterPrep, Buehler).

The electrolyte, 0.1 M HClO₄ (Fixanal, Fluka Analytical), was prepared with ultrapure water. The working electrode was a commercial glassy carbon disc electrode of 5 mm fixed diameter. A platinumized titanium rod (Bank Elektronik – Intelligent Controls GmbH) was used as counter electrode and the reference electrode was a reversible hydrogen electrode (RHE, Hydroflex, Gaskatel Gesellschaft für Gassysteme durch Katalyse und Elektrochemie mbH). Hence, all potentials reported here are quoted with respect to RHE and are corrected for ohmic losses. 0 V_{RHE} was controlled subsequently after each measurement by performing the hydrogen evolution reaction on Pt in the same electrolyte. The internal resistance drop was determined by carrying out an impedance spectrum with a peak-to-peak amplitude of 10 mV in the range from 100 kHz to 1 Hz. The ohmic drop was evaluated from the high frequency intercept point on the real axis of the Nyquist plot. Typically the uncompensated resistance came to 25–30 Ω . RDE measurements were conducted in a nitrogen (5.0, Messer Group GmbH) saturated electrolyte, whereas, the oxygen reduction reaction (ORR) activity measurements were performed in an electrolyte saturated with oxygen (5.5, Messer Group GmbH). During measurement the oxygen supply was sustained to keep the oxygen concentration in solution at a constant level.

In order to prepare the rotating disc electrodes for cyclic voltammetry and ORR measurements, 2 cm² of the impregnated gas diffusion electrodes were suspended in 2-propanol and treated in an ultrasonic bath to form a homogeneous catalysts dispersion. A 10 μl aliquot of the dispersion was dispensed onto the working electrode resulting in a loading of 28 $\mu\text{g}_{Pt} \text{ cm}^{-2}$ geometric surface area.

The electrocatalysts were pre-treated using 250 cyclic voltammetry scans between 0.050 and 1.255 V_{RHE} at a scan rate of 500 mV s^{-1} . Afterwards, an analysis cycle was performed from 0.050 to 1.055 V_{RHE} at 50 mV s^{-1} . The electrochemical active platinum surface area (ECSA) was determined from the mean integral charge Q of the hydrogen adsorption/desorption area (H_{upd}) after double-layer correction, considering 210 $\mu\text{C cm}^{-2}$ as conversion factor [3,40] according to Eq. (1). L_{Pt} is the Pt loading on the working electrode ($\text{mg}_{Pt} \text{ cm}^{-2}$) and A_g (cm^2) is the geometric surface of the glassy carbon electrode and the cathode for HT-PEM in-situ ECSA determination, respectively.

Table 1
Nomenclature of the prepared Pt–Co/C catalysts and their post-preparation treatments.

Pt–Co/C	1st Treatment	2nd Treatment
untreated	–	–
leached	Leaching, 10 vol.% H ₂ SO ₄	–
leached + HT	Leaching, 10 vol.% H ₂ SO ₄	Ramped annealing, starting at 30 °C, 5 °C min ⁻¹ to 220 °C, dwell 45 min

$$\text{ECSA}(\text{cm}^2 \text{ mg}_{\text{Pt}}^{-1}) = \frac{Q_{\text{Hupd}}(\text{C})}{210 \times 10^{-6} \text{ C cm}_{\text{Pt}}^{-2} L_{\text{Pt}}(\text{mg}_{\text{Pt}} \text{ cm}^{-2}) A_{\text{g}}(\text{cm}^2)} \quad (1)$$

To investigate the ORR activity potential sweeps between 0.050 and 1.055 V with a scan rate of 50 mV s^{-1} were conducted at a rotating speed of 1600 rpm. The specific current density (specific activity, SA) and the mass activity (MA) were calculated at $0.9 V_{\text{RHE}}$, respectively [41].

In order to determine the stability and durability of the as-prepared catalyst samples accelerated stress tests (AST) were conducted. Therefore, the electrodes were cycled 1665 times between 0.5 and $1.4 V_{\text{RHE}}$ in deaerated 0.1 M HClO_4 at a scan rate of 500 mV s^{-1} . Every 555th cycle the ECSA was determined. The loss of ECSA gives information on the stability of the synthesized Pt–Co electrocatalysts.

2.5.2. In-situ characterization

2.5.2.1. Polarization curves. A single cell setup with an active area of 50 cm^2 and a serpentine channel flow field structure on anode and cathode was chosen. Reactant flow rates were measured and controlled using mass flow controllers. Cell temperature was set to $160 \text{ }^\circ\text{C}$ controlled by electrical heating cartridges and the stoichiometries were kept constant at 1.2 for hydrogen (3.0, Westfalen AG) or synthetic reformat (76.0% H_2 , 1.2% CO and 22.8% CO_2 , Westfalen AG) and 2.0 for air, respectively.

2.5.2.2. Long term operation under constant load. Long term operation under constant load was conducted at a current density of 0.2 A cm^{-2} and at a temperature of $160 \text{ }^\circ\text{C}$. The single cell was fueled with hydrogen on the anode with a stoichiometry of 1.2 and air at the cathode with a stoichiometry of 2.0.

2.5.2.3. Cyclic voltammetry. Cyclic voltammograms were recorded using a Zahner power potentiostat (PP241, Zahner Elektrik) and a Zahner electrochemical workstation (IM6ex, Zahner Elektrik). The MEAs were tested in a 50 cm^2 single cell and fed with dry hydrogen on the anode (which was also used as pseudo-reference electrode) and humidified nitrogen on the cathode. The ECSA was determined by cycling the cathode between 0.095 and 1.100 V with 100 mV s^{-1} 100 times, followed by an analysis scan with 50 mV s^{-1} . The ECSA was calculated according to Eq. (1).

2.5.2.4. Electrochemical impedance spectroscopy.

Electrochemical impedance spectra (EIS) were recorded in a pseudo-galvanostatic mode with a Zahner power potentiostat (PP241, Zahner Elektrik) and the results are presented in Nyquist plots. The peak-to-peak amplitude was set to 5 mV at 0.2 A cm^{-2} . At the anode synthetic reformat was supplied.

Equivalent circuit (EC) analysis was used to quantify the different losses occurring in the as-prepared HT-PEM MEA.

3. Results and discussion

3.1. Structural and chemical analysis

In order to obtain information about the size of the catalysts particles as well as their distribution on the carbon electrode TEM measurements were performed. The high-resolution TEM images in Fig. 1 show the crystalline catalyst particles on the turbostratic carbon electrode before leaching and heat treatment (a) and afterwards (b). The separate spherical nanoparticles are randomly distributed across the HSAC and possess a size of $4.6 \pm 1.1 \text{ nm}$ with a minimum value of about 2.2 nm and a maximum of 7.3 nm in diameter before leaching. The average size of the nanoparticles after the leaching is $4.5 \pm 0.9 \text{ nm}$ with a minimum value of about 2.4 nm and a maximum of 7.0 nm in diameter. The morphology as well as the size of the catalysts nanoparticles did not change significantly during leaching and heat treatment. The electron diffraction patterns shown in the insets of Fig. 1 reveal the quasi polycrystallinity. The diffraction rings were obtained by averaging over several randomly oriented platinum crystals. When comparing the measured d-values with literature values for cubic platinum [42] a maximum deviation of 1.3% can be detected after leaching. Neither for cubic nor for hexagonal crystalline cobalt diffraction intensities were observed. Nevertheless, the presence of cobalt was verified via EDX measurements taken over an area of several hundred nanometers in dimension. The ratio of cobalt to platinum after leaching shows that the amount of platinum with $96.5 \pm 1.3 \text{ at.}\%$ highly outweighs the contained amount of cobalt with $3.5 \pm 1.3 \text{ at.}\%$. The analysis of the elemental distribution within an individual nanoparticle was not successful due to the weak signal. Given this small quantity of cobalt, a supposed alloy of platinum and cobalt would result in only slightly modified lattice plane distances. Therefore the detection of such an alloy cannot be achieved via electron diffraction or high-resolution TEM regarding

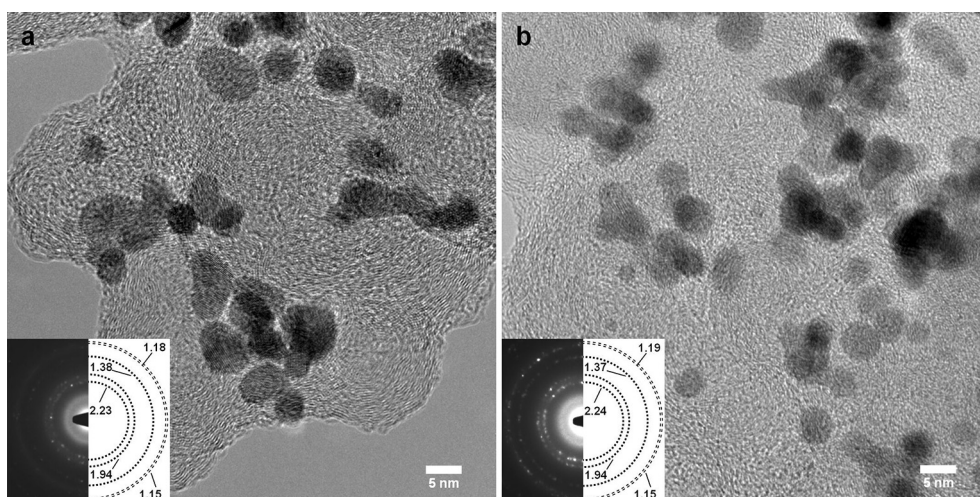


Fig. 1. High-Resolution TEM images of Pt–Co loaded HSAC before leaching and heat treatment (a) and afterwards (b). The insets show the electron diffraction patterns of the crystalline catalyst particles. The indicated d-values are given in Å.

the experimental error. EDX measurements before leaching show a significant higher ratio of cobalt (28.0 ± 6.0 at.%) to platinum (72.0 ± 6.0 at.%). Electron diffraction experiments before leaching also show intensities originating from crystalline cubic platinum only. The deviation from literature d -values (1.5%) for platinum is in the same range as for the leached sample and represents the measuring error. This finding and the fact that about 88% of the initial amount of cobalt is removed during the leaching process, lead to the assumption that most of the cobalt on the electrode was present in amorphous state.

The Pt–Co/C catalysts were further analyzed using X-ray diffraction technique. The XRD patterns of the untreated, the leached and the leached and heat treated Pt–Co/C samples as well as the Pt/C reference are given in Fig. 2. The 2θ Bragg peaks at ca. 39.8° , 46.3° , 67.7° , 81.4° , 85.5° , 103.6° , 118.1° and 123.2° correspond to the face-centered cubic (fcc) reflections of Pt(111), Pt(200), Pt(220), Pt(311), Pt(222), Pt(400), Pt(331) and Pt(420), respectively [36]. The average particle size of the catalysts was determined by using the Scherrer relationship [39]. The obtained crystallite sizes of the Pt–Co/C catalysts are within a range of 2.6–2.9 nm, whereas the particle size of the Pt/C sample is 4.1 nm. As XRD only provides the average size of the diffracting crystals rather than the particle size, the calculated crystallite sizes of the as-prepared Pt–Co/C catalysts are smaller than those determined from HR-TEM images. The Co contents within the Pt–Co/C samples were calculated by comparing the lattice parameters (a) obtained from the measured 2θ Bragg peaks with those of the commercial Pt/C catalyst ($a = 0.39147(7)$ nm), metallic Pt ($a = 0.39231$ nm) [36] and metallic Co ($a = 0.35441$ nm), respectively [37]. The lattice parameter of the commercial Pt/C sample is comparable with the previously published value of 0.39158 nm [38]. The lattice parameters of the nanocrystalline samples, the contents of Co in the Pt–Co/C catalysts derived from Vegard's law [38,43] and crystallite sizes are given in Table 2. The amounts (at.%) of Co refer to the lattice parameter of the Pt/C sample of 0.39147(7) nm. However, if the lattice parameter of metallic Pt of 0.39231 nm [36] is used as reference for Vegard's law, the Co content of the PtCo solid solutions is increased by 2.3 at.%. In both cases, the results obtained from the XRD measurements are in accordance to the EDX analysis.

3.2. Catalytic activity and degradation tests

After having discussed the structural and chemical properties of the prepared catalysts, we focus on their electrochemical and catalytic characteristics. Figs. 3 and 4 depict the beneficial effects of

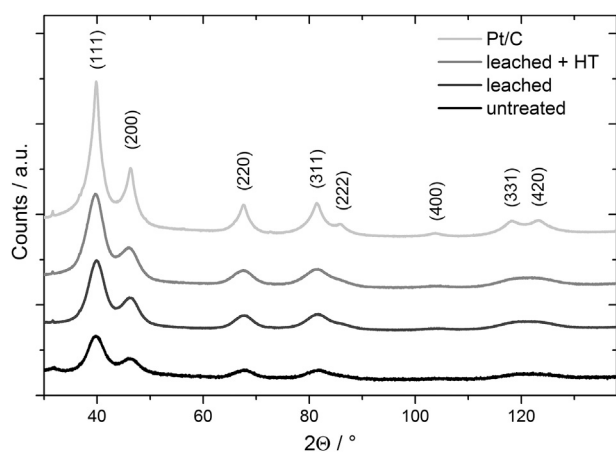


Fig. 2. X-ray diffraction patterns of the untreated, leached, the leached and heat treated Pt–Co/C catalysts and the Pt/C catalysts.

Table 2

Summary of the properties of the differently treated Pt–Co/C catalysts and the commercial Pt/C catalyst obtained from XRD measurements. The amounts (at.%) of Co refer to lattice parameter of the Pt/C sample of 0.39147(7) nm.

	a /nm	at.% Co	Size/nm
Pt–Co/C untreated	0.39013(8)	3.6	2.9
Pt–Co/C leached	0.39079(8)	1.8	2.6
Pt–Co/C leached + HT	0.39060(7)	2.4	2.6
Pt/C	0.39147(7)	–	4.1

the performed post-preparation treatments on the catalytic properties of the Pt–Co/C catalyst, which are summarized in Table 3. Fig. 4(b) shows the ORR polarization curves of the leached and heat treated Pt–Co/C catalyst and the Pt/C catalyst. Clearly, the leached and heat treated Pt–Co/C catalyst shows a more positive onset potential than the Pt/C catalyst and a higher current in the mixed-kinetic-diffusion region. The positive effect of acid-leaching on the performance of the Pt-transition metal catalysts in comparison to the Pt/C catalyst is ascribed to the dissolution of the inactive transition metal components and the segregation of Pt at the surface of the catalysts, resulting in a roughening of the surface and leaving behind a Pt-skeleton structure with a negligible amount of the solute metal [1,14,28,33]. Treating the carbon supported Pt–Co catalysts in 10 vol.% H_2SO_4 for 30 min led to a 1.7-fold increase of the specific activity (SA) and a 1.6-fold increase of the mass activity (MA) in comparison to the Pt/C sample. Additionally, a heat treatment was performed. In contrast to previously reported annealing steps in inert, reducing atmosphere or in vacuum at temperatures above $450^\circ C$ [1,28,33,44], a mild heat treatment at $220^\circ C$ in nitrogen atmosphere was performed [34,45]. The heat treatment step was initiated with an applied temperature ramp of $5^\circ C\ min^{-1}$ starting at $30^\circ C$. The final temperature of $220^\circ C$ was held for 45 min; afterwards the catalyst samples were removed from the oven and cooled down to room temperature immediately. The additional heating induced a further increase of the MA of the catalysts toward ORR in comparison to the leached samples, resulting in a 2-fold activity increase over the Pt/C catalyst, whereas, the SA was not affected. The Tafel plot in Fig. 4(a) compares the electrocatalytic ORR activities of the differently treated catalysts samples to the commercial Pt/C sample.

The cyclic voltammograms (CVs) in Fig. 3, recorded in nitrogen saturated 0.1 M $HClO_4$ solution, show the typical features of Pt-based catalysts including a H_{upd} region, a double layer and an oxide formation region. The H_{upd} region reflects the catalysts

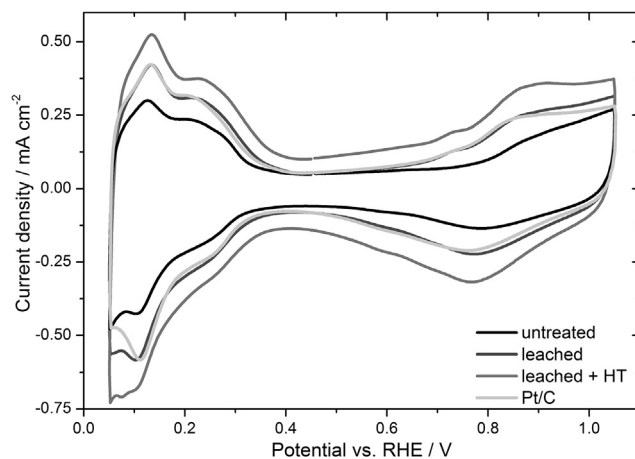


Fig. 3. Cyclic voltammograms of the as-prepared Pt–Co/C catalysts and the Pt/C reference recorded at a scan rate of $50\ mV\ s^{-1}$ in nitrogen saturated 0.1 M $HClO_4$ electrolyte.

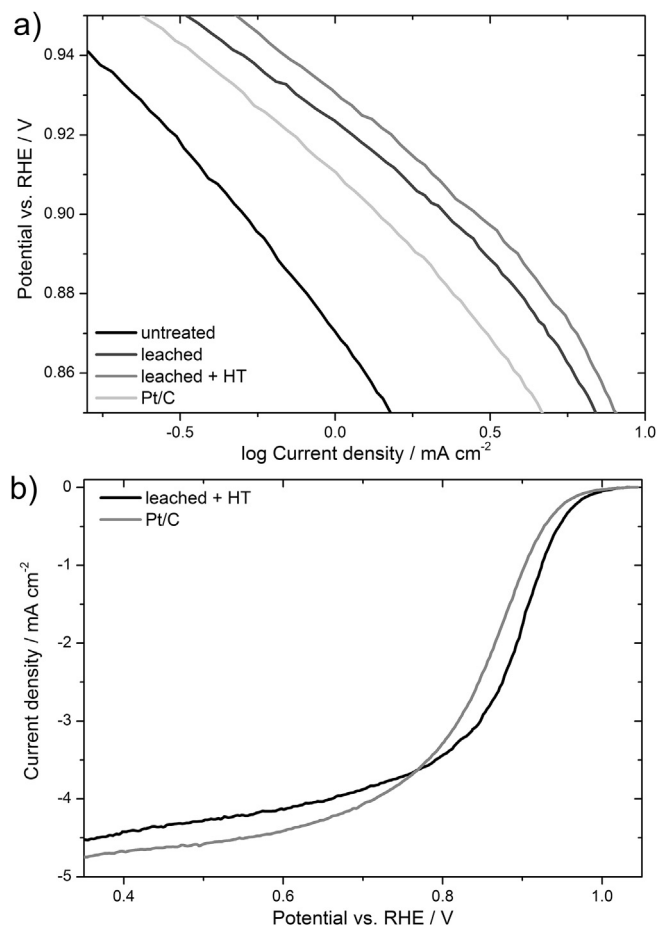


Fig. 4. (a) Tafel plots obtained from corresponding ORR polarization curves of the Pt/C and the Pt–Co/C catalyst samples, recorded at a scan rate of 50 mV s^{-1} in oxygen saturated 0.1 M HClO_4 electrolyte with a rotation speed of 1600 rpm . (b) Comparison of the ORR polarization curves of the leached and heat treated Pt–Co/C catalyst and the Pt/C catalyst.

electrochemical active surface area. It is evident that the catalysts reveal a higher ECSA after post-preparation treatment. As discussed above, the increase in ECSA is mainly due to the dissolution of the electrocatalytically inactive Co at the catalysts surface. Furthermore, the leaching and especially the heat treatment of the Pt–Co/C catalysts led to the removal of ethylene glycol, its decomposition products and the non-ionic surfactant from the catalysts surface. One would anticipate a decrease of ECSA during heat treatment, but using rather low temperatures, the cleaning of the catalysts surface from organic residues has a higher impact on the active surface than the increase of the mean particle size (see Fig. 3) [34,45]. However, since the annealing step is part of a continuous process, oxygen impurities in the N_2 atmosphere are almost unavoidable.

Table 3

Summary of the properties of the differently treated Pt–Co/C catalysts and the Pt/C reference catalyst.

	SA/ mA cm^{-2}	MA/A $\text{mg}_{\text{Pt}}^{-1}$	Roughness factor/ $\text{cm}^2_{\text{Pt}}/\text{cm}^2_{\text{geo}}$	Initial ECSA/ $\text{cm}^2/\text{mg}_{\text{Pt}}^{-1}$	ECSA loss after 3rd AST/%
Pt–Co/C untreated	0.090	0.018	5.54	198	38
Pt–Co/C leached	0.318	0.081	7.18	257	23
Pt–Co/C leached + HT	0.322	0.100	8.68	310	20
Pt/C	0.188	0.049	7.29	260	49

Thus, the CV of the leached and heat treated catalyst exhibits an increased double layer capacitance compared to the other catalyst samples due to partial surface oxidation of the HSAC. The CV of the Pt/C catalyst sample equals the leached Pt–Co/C catalyst.

As mentioned before, due to the highly acidic and oxidizing environment of an HT-PEMFC cathode, Pt–M catalysts are prone to gradual degradation, which limits the lifetime of the PEMFC significantly. Especially high potentials ($>1.2 \text{ V}$) lead to the corrosion of the carbon support material, the detachment of the Pt nanoparticles, their agglomeration and/or loss of electrical contact [1]. In order to determine the stability and durability of the prepared Pt–Co/C catalysts samples accelerated stress tests were conducted. Fig. 5 compares the degradation behavior of the untreated (a) to the leached and heat treated catalyst (b) and to the Pt/C reference (c). By treating the as-prepared catalysts according to the procedures mentioned above the initial ECSA as well as the stability are increased significantly. In accordance to the results obtained from XRD and TEM analysis and since the ECSA increases after leaching and heat treatment, the increase of stability cannot be attributed to an enlargement of the average particle size. We support the speculation of Stephens et al. that the annealing procedure smooths out the surface of the catalysts and/or removes defects of undercoordinated sites, which are most susceptible to corrosion [1].

3.3. HT-PEMFC studies

To enhance the knowledge of the interactions of the as-prepared leached and heat treated Pt–Co/C catalyst with other components inside an HT-PEM MEA, e.g. phosphoric acid, single cell tests were carried out. Furthermore, the operation in fuel cells should give information on the performance of the synthesized nanoparticles and their long term stability toward corrosion and/or de-alloying.

3.3.1. Polarization and power density

After manufacturing, the MEA was characterized by investigation of polarization, power density and electrochemical impedance properties, using hydrogen and synthetic reformate as anode feedstock, respectively. In Fig. 6 the polarization of the leached and heat treated Pt–Co/C based MEA and the commercial Pt/C based HT-PEM MEA are shown. The first polarization curve of the leached and heat treated Pt–Co/C based MEA was recorded immediately after the MEA hot pressing step; the second was taken after 600 h long term operation under a constant load of 0.2 A cm^{-2} at $160 \text{ }^\circ\text{C}$. In both cases, applying pure hydrogen and synthetic reformate at the anode, the performance of the in-house prepared HT-PEM MEA was enhanced during operation. The open cell voltage (OCV) value as well as the ohmic resistance improved during the long term test. The polarization and power density of the commercial Pt/C MEA showed no change during the 600 h long term operation. While fed with hydrogen, the in-house prepared Pt–Co/C based HT-PEM MEA, having a lower Pt loading at the cathode, shows an enhanced performance over the commercial MEA after 600 h of operation, especially at higher current densities (Fig. 6(a)). However, when fueled with synthetic reformate, both MEAs exhibit an equal performance (Fig. 6(b)). The results of the durability test confirm the higher activity of the as-prepared leached and heat treated Pt–Co/C catalyst compared to the commercial Pt/C catalyst, as observed in ex-situ analysis, due to the equal performance while having less Pt.

3.3.2. Long term operation under constant load

The as-prepared MEA demonstrated a good durability in single cell operation (Fig. 7). The average degradation rate of the leached and heat treated Pt–Co/C based HT-PEM MEA during the 600 h test

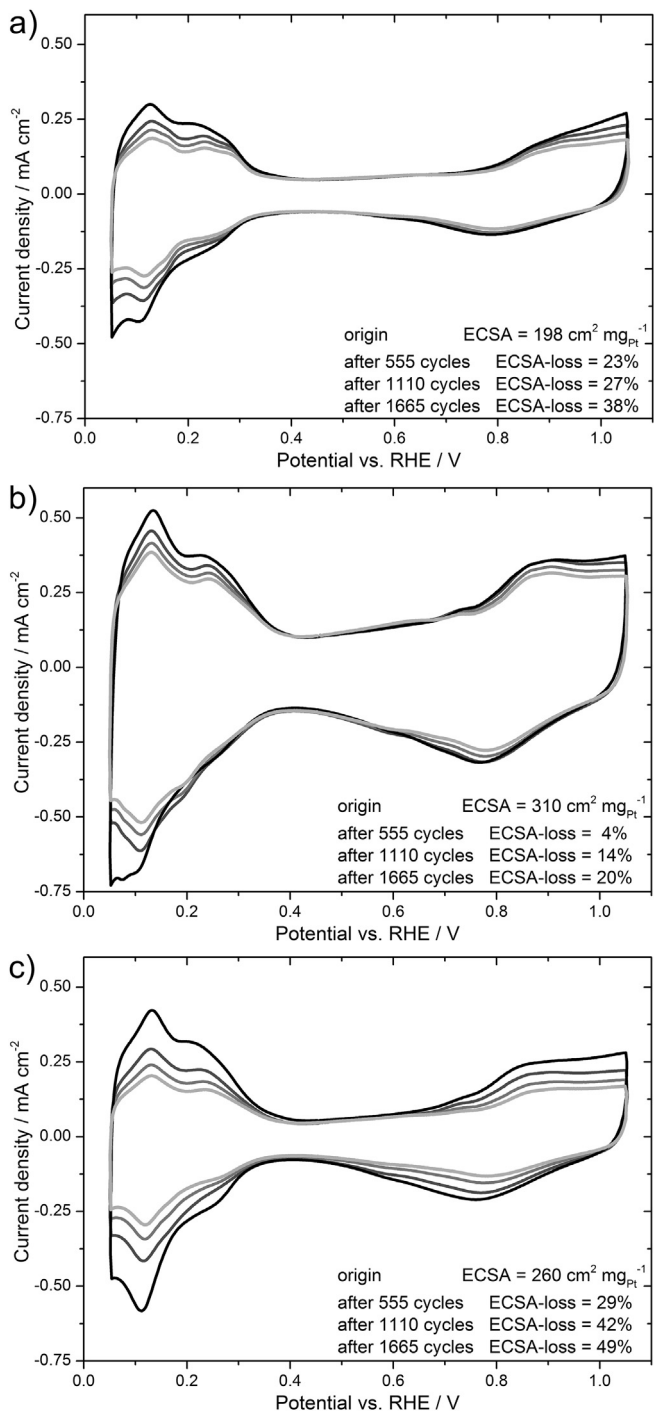


Fig. 5. Cyclic voltammograms of the untreated Pt–Co/C catalyst (a), the leached and heat treated Pt–Co/C catalyst (b) and the Pt/C catalyst (c) recorded at a scan rate of 50 mV s⁻¹ in nitrogen saturated 0.1 M HClO₄ electrolyte. The gradual degradation of the catalysts during AST cycling is given after 555, 1110 and 1665 cycles in form of the loss of ECSA.

under steady state conditions at 160 °C was 0 μV h⁻¹. Especially during the first 14 h of the long term operation a very steep increase in cell voltage was observed, followed by a constant increase up to 500 h runtime. After that, the cell voltage stabilized at 604 mV. In contrast, the commercially obtained HT-PEM MEA from elcomax GmbH showed a better performance at the beginning of the durability test, but lost cell voltage continually over the first 400 h of operation, which stabilized at 608 mV afterwards. The 1 kHz AC

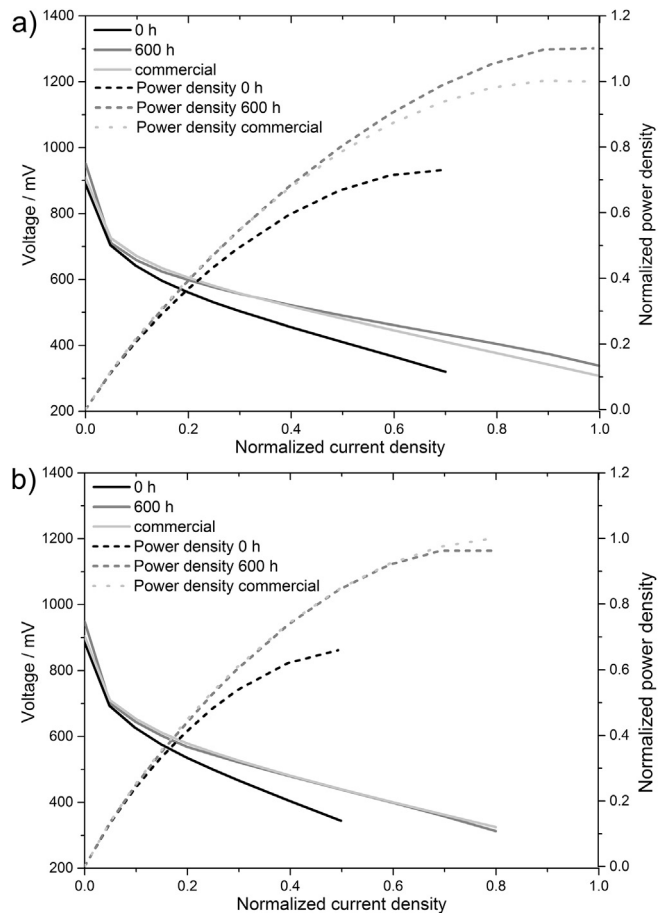


Fig. 6. Polarization curves and power densities of the leached and heat treated Pt–Co/C based HT-PEM MEA before and after 600 h long term operation and the commercial HT-PEM MEA under constant load at 160 °C, fueled with hydrogen (a) and synthetic reformat (b) at the anode and air at the cathode.

resistances were at a constant value of 2.4 mΩ for the leached and heat treated Pt–Co/C based HT-PEM MEA and 1.7 mΩ for the commercial one, respectively. Both values indicate a good distribution of H₃PO₄ electrolyte within the catalyst layer of the cathode electrode. By comparison, both MEAs showed an equal

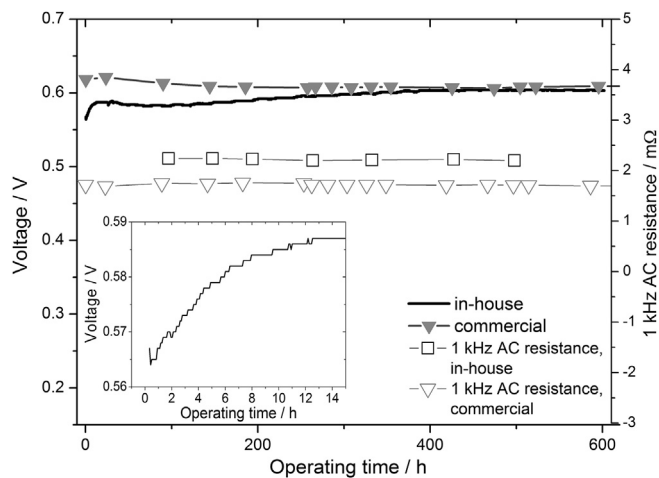


Fig. 7. Comparison of cell voltages and the corresponding 1 kHz AC resistances of the leached and heat treated Pt–Co/C based HT-PEM MEA and a commercial HT-PEM MEA during durability testing at 160 °C. The insert shows the first 14 h of the long term operation of the in-house prepared MEA.

performance during 600 h of operation under constant load, although the commercial HT-PEM MEA had a much higher Pt loading at the cathode.

3.3.3. Electrochemical impedance spectroscopy

EIS is a commonly applied tool in electrochemistry to investigate corrosion processes and to quantify losses occurring in electrochemical devices, such as batteries. In fuel cell research it is a reliable method, providing information on catalyst and membrane materials [46]. In general, the information on the catalyst and membrane materials derives either from a process model based on physicochemical relations, kinetics, mechanisms and consequently analytic equations or from a measurement model by means of equivalent circuit (EC) analogs. Both evaluation approaches offer advantages, but have insufficiencies as well. For example a good numerical complex nonlinear least square fit of a measurement model to experimental data does not necessarily mean the correct EC is applied. On the other hand a process model approach is often too complex to be applied on multipart systems like fuel cells. Rezaei Niya et al. gives a very concise comparison of these two approaches with respect to fuel cell applications [47] and Macdonald makes a very detailed distinction between models and analogs [48]. Due to the increasing complexity of process models with the increasing number of components in a fuel cell a measurement model based analysis is the more straight-forward approach for our HT-PEMFC investigation. Although the physical meaning of the applied EC elements may be under discussion at least correlations can be drawn between the described equivalent circuit and the analysis as follows.

Herein, EC analysis was used to simulate the entire frequency range of the given impedance spectra (e.g. Fig. 8). Therefore, electric components, such as resistors and capacitors, were used for the simulation and fitting process. The applied EC (Fig. 9) is based on the modified Randles cell equivalent circuit suggested by Zhang et al. [49] and its further modification as described in Ref. [50].

In Fig. 8 the recorded EIS spectra of the leached and heat treated Pt–Co/C based MEA are presented in form of their Nyquist plots. The measurement at the beginning of the long term operation shows three depressed semicircles, while after 600 h of operation a fourth arising semicircle may be observed additionally. Both impedance spectra show the same frequency dependence and are interpreted as follows.

The beginning semicircle which is observed in the very high frequency area may not be attributed to an anode charge transfer reaction since the characteristic frequency (23208 Hz) is too high to be formed by a chemical reaction. The origin of this rc element is due to contact resistance between the flowplates and the MEA while the capacitance is attributed to small amounts of H_3PO_4 at the interface between the two layers. Other explanations for such a behavior refer these potential independent high frequency

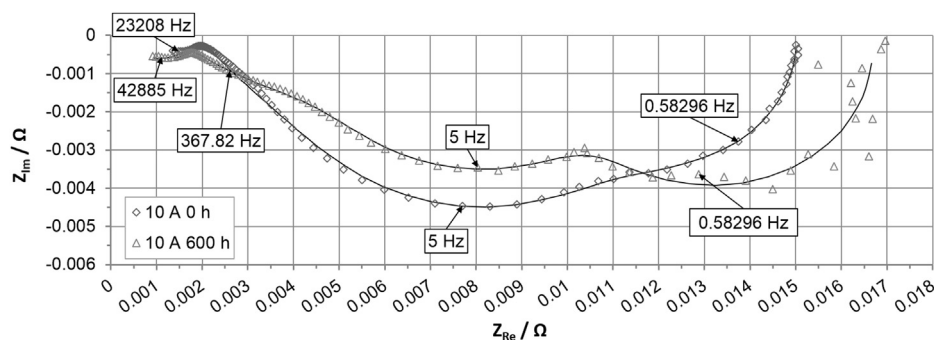


Fig. 8. Nyquist plots of the EIS measurements of the leached and heat treated Pt–Co/C based HT-PEM MEA at BoL and after 600 h of operation.

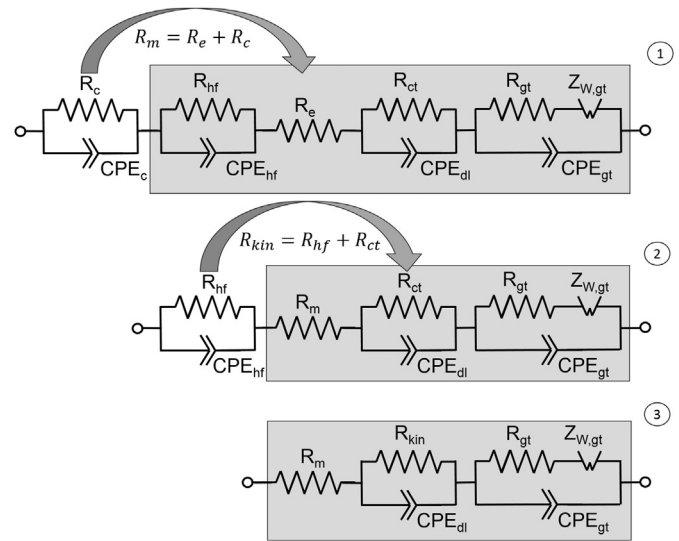


Fig. 9. Equivalent circuit which was applied for fitting procedure (1) and simplification steps (2) and (3).

semicircles to the distribution of resistance effects within the electrolyte in the catalysts layer [51,52]. This phenomenon leads to the fact that the high frequency intercept, which is commonly ascribed to the electrolyte resistance (R_e), is not seen directly within the observed frequency range. Therefore, the membrane resistance is obtained by calculating the sum of these distributed ohmic contact resistances (R_c) and the electrolyte resistance (R_e) and is in accordance with [50,53] denoted by membrane resistance (R_m).

In the mid frequency area at least one depressed semicircle is observed which is attributed mainly to the ORR charge transfer reaction. The corresponding anode impedance semicircle or anode loop is masked by the more significant ORR semicircle. Especially at the beginning of the long term operation the characteristic frequencies are too close together to be seen as separate semicircles. After 600 h of operation the characteristic frequencies have separated leading to two semicircles in the Nyquist plot and the anode reaction semicircle is observed. Since the origin of this loop is still under discussion the corresponding equivalent circuit element is better denoted by high frequency loop ($R_{hf}|CPE_{hf}$) than by anode loop [54].

In the low frequency area mass transport limitations are observed in both spectra, but are more significant after 600 h of operation. Additionally, the fluctuations in the low frequency arc indicate a slight flooding event. According to this interpretation the equivalent circuit shown in Fig. 9 was applied for our fitting procedure and simplified for the discussion.

The for the fitting procedure applied formulas as well as the obtained parameters are shown in Table 4, where the kinetic

resistance R_{kin} is the sum of the charge transfer and high frequency resistances ($R_{ct} + R_{hf}$). The membrane resistance R_m is, as described above, the sum of the ohmic contact resistances (R_c) and the electrolyte resistance (R_e). R_{gt} specifies the resistance occurring by the transport of the reactant gases through the porous layer of the GDE. The overall Warburg impedance Z_W is calculated from the Warburg diffusion interpretation parameter T_W , the finite length Warburg resistance R_W and the Warburg exponent P_W . The second column of Table 4 specifies the different coefficients T_{ct} , T_{hf} , T_c and T_{gt} and their corresponding exponents P_{ct} , P_{hf} , P_c and P_{gt} of the constant phase elements (CPEs) given in Fig. 9. All of these parameters exhibit changes during the long term operation experiment. After the first step of simplification it is seen that the membrane resistance $R_m (=R_c + R_e$, see Table 4) has decreased starting from 1.95 mΩ to 1.53 mΩ which is slightly lower than the obtained 1 kHz AC resistance (Fig. 7) recorded throughout the long term experiment. This decrease indicates an improved electrolyte distribution within the active layer, which leads to a decrease of R_c and R_m , respectively. Furthermore, it indicates that the main part of the membrane resistance rather originates from an insufficient electrolyte distribution in the active layer than from the electrolyte resistance itself.

The decrease in the diameter of the mid frequency semicircle ($R_{kin} = R_{ct} + R_{hf}$) is also due to the improved electrolyte distribution within the catalysts layer. During the operation the exponent (P_{dl}) of the constant phase element ascribed to the double layer (CPE_{dl}) decreased as well, which generally indicates a broader distribution of time constants and a better distribution of H_3PO_4 . Both tendencies, the decreased R_{kin} as well as the decreased P_{dl} , indicate an increased active catalyst surface area due to an improved H_3PO_4 distribution. But nevertheless, the fractional increase of the obtained ECSA by CV analysis (see Fig. 10) goes beyond the fractional increase of the kinetic conductance (Table 5). This difference may be explained by the surface roughening effect of the catalysts particles, which increases the accessible inner surface of the catalysts particles and consequently the obtained ECSA.

In Fig. 10 the cyclic voltammograms of the leached and heat treated Pt–Co/C based HT-PEM MEA before and after the durability test are shown. During operation the ECSA of the cathode catalysts layer increased slightly from 104 to 113 cm² mg_{Pt}⁻¹. This enlargement of the active surface area can be attributed either to the redistribution of the H_3PO_4 electrolyte in the doped catalysts layer, resulting in an improved membrane resistance ($R_m = R_e + R_c$) as well as kinetic conductance ($S_{kin} = 1/R_{kin}$), as observed in EIS measurements, or to an additional removal of impurities and inactive Co sites at the surface of the GDE.

According to the obtained parameters (Table 4) the diameter of the low frequency semicircle which is observed more clearly after

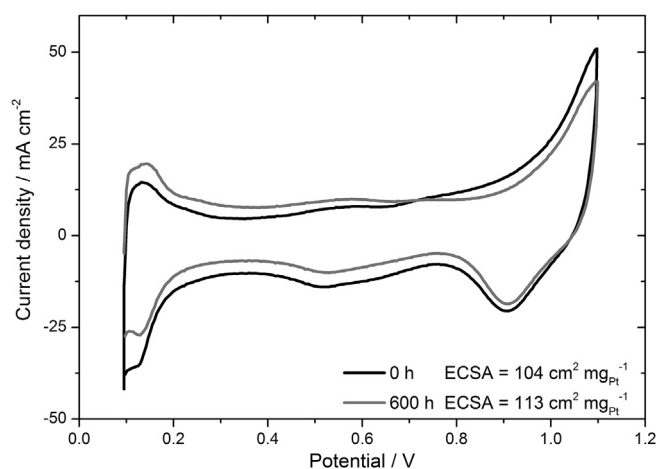


Fig. 10. Cyclic voltammograms of the cathode layer of the leached and heat treated Pt–Co/C based HT-PEM MEA before and after long term operation test, recorded at a scan rate of 50 mV s⁻¹. The anode (fed with dry hydrogen) was used as pseudo-reference electrode. The cathode was supplied with humidified nitrogen.

600 h of operation under constant load is increased. This may also be attributed to an increased wetting of the active layer and consequently longer diffusion pathways when thinking of a flooded agglomerate model [55]. The fluctuations in the low frequency arc also indicate a slight flooding of the active layer although the polarization curve does not indicate such an issue.

4. Conclusion and outlook

In this paper we have presented roll-to-roll processed Pt-M/C catalysts as part of an economic and flexible large scale MEA manufacturing for application as cathode catalysts in PBI-based HT-PEM fuel cells. During production it has been paid attention to keep the synthesis of the catalysts as simple as possible. To obtain a higher Pt utilization the continuous deposition of the catalysts was achieved directly in the optimized porous layer of the gas diffusion electrode. In contrast to conventional casting of catalyst loaded HSAC onto the GDL, the loss of Pt during production is reduced by the presented process, rendering it more economical. Furthermore, Pt enclosures in carbon aggregates are eliminated and due to the absence of batch processes, such as filtering, centrifugation, multiple washing, drying and annealing in tube furnaces, the herein presented continuous MEA fabrication is much more time and cost saving.

After post preparation treatment, such as acid-leaching and annealing, the developed Pt–Co catalysts exhibit good catalytic properties and enhanced stability in ex-situ tests. In comparison to

Table 4
Parameters obtained by the EC fitting procedure (*: fixed parameters).

		0 h	600 h		0 h	600 h
$^0R_{kin}$	R_{ct}/Ω	5.01E-03	4.99E-03	$^2T_{dl}/A V^{-1} \dim[(j\omega)^{-P}]$	1.17E+01	7.91E+00
	R_{hf}/Ω	4.81E-03	4.61E-03	$^2T_{hf}/A V^{-1} \dim[(j\omega)^{-P}]$	5.10E+00	6.29E+00
0R_m	R_c/Ω	1.48E-03	1.21E-03	$^2T_c/A V^{-1} \dim[(j\omega)^{-P}]$	1.00E-02	1.00E-02
	R_e/Ω	4.70E-04	3.18E-04	$^2T_{gt}/A V^{-1} \dim[(j\omega)^{-P}]$	50.4E+00	57.4E+00
R_{gt}	R_{gt}/Ω	3.08E-05	1.17E-03	$^2P_{dl}$	6.43E-01	5.59E-01
1Z_W	T_W	3.77E-04	3.77E-04	$^2P_{hf}$	1.09E+00	1.02E+00
	R_W/Ω	3.27E-03	4.41E-03	2P_c	8.58E-01	9.00E-01
	*P_W	0.5	0.5	$^2P_{gt}$	1.10E+00	1.10E+00
				Applied formulas		
$^0R_{kin} = R_{ct} + R_{hf}$				$j = \text{square root of } -1; \omega = \text{angular frequency/rad s}^{-1}$		
$^1Z_W = R_W \frac{\tanh[(j\omega T_W)^{P_W}]}{(j\omega T_W)^{P_W}}$						
$^2Z_{CPE} = \frac{1}{T_x(j\omega)^{P_x}}$						

Table 5
The ECSA increase vs. the increase of the kinetic conductance ($S_{\text{kin}} = 1/R_{\text{kin}}$).

	ECSA/cm ² mg _{Pt} ⁻¹	R _{kin} /Ω	S _{kin} /Ω ⁻¹
0 h	104	9.82E-03	102
600 h	113	9.60E-03	104
Ratio	1.09		1.02

reported Pt₃Co catalysts, which have been prepared by laborious and expensive production processes, our Pt–Co catalysts lack in high specific and mass activity toward oxygen reduction reaction under ex-situ conditions. Though, under in-situ conditions our catalysts perform equally to commercially available Pt catalysts or even outperform them.

The begin-of-lifetime polarization curves, which were obtained directly after hot-pressing of the leached and heat treated Pt–Co/C based HT-PEM MEA, show a poor performance. Within the first 14 h of operation at constant load a steep increase of the cell performance was observed. We ascribe this voltage gain to the redistribution of the electrolyte within the cathode catalyst layer after hot-pressing and to a further cleaning of the catalysts surface. EIS measurements, recorded in synthetic reformat, and fitting of the data thereof confirm our assumption. After the steep increase the cell voltage stabilized at 604 mV for the remaining test period. A comparison of the polarization curves taken before and after the long term HT-PEM test for 600 h showed a significant increase of cell performance and OCV.

By using our newly developed catalyst deposition system we achieved a reduction of the platinum loading of HT-PEM MEA cathodes without loss of performance.

Currently, a fuel cell stack test including long term operation with natural gas reformat is under progress. With these results we will gain further insight into the durability of our Pt–Co/C catalyst system and its feasibility for HT-PEM fuel cell systems.

Acknowledgments

Support from NAWI Graz and financial support by the Austrian Federal Ministry of Transport, Innovation and Technology (BMVIT) and The Austrian Research Promotion Agency (FFG) through the program a3plus and the IEA research cooperation is gratefully acknowledged. Financial support from the German Federal Ministry for Economy and Technology within the program ZIM-KOOP is also gratefully acknowledged.

References

- [1] I.E.L. Stephens, A.S. Bondarenko, U. Grønberg, J. Rossmeisl, I. Chorkendorff, *Energy Environ. Sci.* 5 (2012) 6744.
- [2] K.C. Neyerlin, W. Gu, J. Jorne, H.A. Gasteiger, *J. Electrochem. Soc.* 154 (2007) B631.
- [3] H.A. Gasteiger, S.S. Kocha, B. Sompalli, F.T. Wagner, *Appl. Catal. B Environ.* 56 (2005) 9.
- [4] J.K. Nørskov, J. Rossmeisl, A. Logadottir, L. Lindqvist, J.R. Kitchin, T. Bligaard, H. Jónsson, *J. Phys. Chem. B* 108 (2004) 17886.
- [5] S.-K. Kim, K.-H. Kim, J.O. Park, K. Kim, T. Ko, S.-W. Choi, C. Pak, H. Chang, J.-C. Lee, *J. Power Sources* 226 (2013) 346.
- [6] R. Bashyam, P. Zelenay, *Nature* 443 (2006) 63.
- [7] M.S. Thorum, J. Yadav, A.A. Gewirth, *Angew. Chem. Int. Ed. Engl.* 48 (2009) 165.
- [8] G. Wu, K.L. More, C.M. Johnston, P. Zelenay, *Science* 332 (2011) 443.
- [9] F. Calle-Vallejo, J.I. Martínez, J. Rossmeisl, *Phys. Chem. Chem. Phys.* 13 (2011) 15639.
- [10] M. Lefèvre, E. Proietti, F. Jaouen, J.-P. Dodelet, *Science* 324 (2009) 71.
- [11] Y. Gorlin, T.F. Jaramillo, *J. Am. Chem. Soc.* 132 (2010) 13612.
- [12] J. Suntivich, H.A. Gasteiger, N. Yabuuchi, Y. Shao-Horn, *J. Electrochem. Soc.* 157 (2010) B1263.
- [13] M. Escudero-Escribano, A. Verdagué-Casadevall, P. Malacrida, U. Grønberg, B.P. Knudsen, A.K. Jepsen, J. Rossmeisl, I.E.L. Stephens, I. Chorkendorff, *J. Am. Chem. Soc.* 134 (2012) 16476.
- [14] V.R. Stamenkovic, B.S. Mun, M. Arenz, K.J.J. Mayrhofer, C.A. Lucas, G. Wang, P.N. Ross, N.M. Markovic, *Nat. Mater.* 6 (2007) 241.
- [15] J.R. Kitchin, J.K. Nørskov, M.A. Barteau, J.G. Chen, *J. Chem. Phys.* 120 (2004) 10240.
- [16] V.R. Stamenkovic, B. Fowler, B.S. Mun, G. Wang, P.N. Ross, C.A. Lucas, N.M. Markovic, *Science* 315 (2007) 493.
- [17] T. Toda, H. Igarashi, H. Uchida, M. Watanabe, *J. Electrochem. Soc.* 146 (1999) 3750.
- [18] X. Liu, G. Fu, Y. Chen, Y. Tang, P. She, T. Lu, *Chemistry* 20 (2014) 585.
- [19] G. Fu, K. Wu, J. Lin, Y. Tang, Y. Chen, Y. Zhou, T. Lu, *J. Phys. Chem. C* 117 (2013) 9826.
- [20] E. Antolini, T. Lopes, E.R. Gonzalez, *J. Alloys Compd.* 461 (2008) 253.
- [21] B.C. Beard, P.N. Ross, *J. Electrochem. Soc.* 137 (1990) 3368.
- [22] V.R. Stamenkovic, T.J. Schmidt, P.N. Ross, N.M. Markovic, *J. Phys. Chem. B* 106 (2002) 11970.
- [23] N.M. Markovic, T.J. Schmidt, V.R. Stamenkovic, P.N. Ross, *Fuel Cells* 1 (2001) 105.
- [24] J.R.C. Salgado, E. Antolini, E.R. Gonzalez, *J. Power Sources* 141 (2005) 13.
- [25] J.R.C. Salgado, E. Antolini, E.R. Gonzalez, *J. Power Sources* 138 (2004) 56.
- [26] T. Lopes, E. Antolini, F. Colmati, E.R. Gonzalez, *J. Power Sources* 164 (2007) 111.
- [27] E. Antolini, J.R.C. Salgado, E.R. Gonzalez, *J. Electroanal. Chem.* 580 (2005) 145.
- [28] I. Spanos, J.J.K. Kirkensgaard, K. Mortensen, M. Arenz, *J. Power Sources* 245 (2014) 908.
- [29] K. Jayasayee, J.A.R. Van Veen, T.G. Manivasagam, S. Celebi, E.J.M. Hensen, F.A. de Bruijn, *Appl. Catal. B Environ.* 111–112 (2012) 515.
- [30] K.J.J. Mayrhofer, K. Hartl, V. Juhart, M. Arenz, *J. Am. Chem. Soc.* 131 (2009) 16348.
- [31] S.C. Zignani, E. Antolini, E.R. Gonzalez, *J. Power Sources* 182 (2008) 83.
- [32] E. Antolini, J.R.C. Salgado, E.R. Gonzalez, *J. Power Sources* 160 (2006) 957.
- [33] V.R. Stamenkovic, B.S. Mun, K.J.J. Mayrhofer, P.N. Ross, N.M. Markovic, *J. Am. Chem. Soc.* 128 (2006) 8813.
- [34] C. Wang, M. Chi, D. Li, D. Strmcnik, D. van der Vliet, G. Wang, V. Komanicky, K.-C. Chang, A.P. Paulikas, D. Tripkovic, J. Pearson, K.L. More, N.M. Markovic, V.R. Stamenkovic, *J. Am. Chem. Soc.* 133 (2011) 14396.
- [35] C. Wang, D. van der Vliet, K.L. More, N.J. Zaluzec, S. Peng, S. Sun, H. Daimon, G. Wang, J. Greeley, J. Pearson, A.P. Paulikas, G. Karapetrov, D. Strmcnik, N.M. Markovic, V.R. Stamenkovic, *Nano Lett.* 11 (2011) 919.
- [36] H.E. Swanson, E. Tatge, *Natl. Bur. Stand. Circ.* 539 (1953) 1.
- [37] E.A. Owen, D. Madoc Jones, *Proc. Phys. Soc. Sect. B* 67 (1954) 456.
- [38] A.S. Darling, *Platin. Met. Rev.* (1963) 96.
- [39] P. Scherrer, *Nachr. Ges. Wiss. Göttingen* 26 (1918) 98.
- [40] Y. Garsany, O.A. Baturina, K.E. Swider-Lyons, S.S. Kocha, *Anal. Chem.* 82 (2010) 6321.
- [41] K.J.J. Mayrhofer, D. Strmcnik, B.B. Blizanac, V.R. Stamenkovic, M. Arenz, N.M. Markovic, *Electrochim. Acta* 53 (2008) 3181.
- [42] R.W.G. Wyckoff, *The Structure of Crystals*, second ed., vol. 1, Interscience Publishers, New York, 1963.
- [43] E.I. Santiago, L.C. Varanda, H.M. Villullas, *J. Phys. Chem. C* 111 (2007) 3146.
- [44] P. Strasser, S. Koh, T. Anniyev, J. Greeley, K. More, C. Yu, Z. Liu, S. Kaya, D. Nordlund, H. Ogasawara, M.F. Toney, A. Nilsson, *Nat. Chem.* 2 (2010) 454.
- [45] L. Xiong, A. Manthiram, *Electrochim. Acta* 50 (2005) 2323.
- [46] M.E. Orazem, B. Tribollet, *Electrochemical Impedance Spectroscopy*, John Wiley & Sons, Inc., Hoboken, New Jersey, 2008.
- [47] S.M. Rezaei Niya, M. Hoorfar, *J. Power Sources* 240 (2013) 281.
- [48] D.D. Macdonald, *Electrochim. Acta* 51 (2006) 1376.
- [49] J. Zhang, Y. Tang, C. Song, J. Zhang, *J. Power Sources* 172 (2007) 163.
- [50] J. Jespersen, E. Schaltz, S. Kær, *J. Power Sources* 191 (2009) 289.
- [51] X. Yuan, H. Wang, J.C. Sun, J. Zhang, *Int. J. Hydrogen Energy* 32 (2007) 4365.
- [52] T.J.P. Freire, E.R. Gonzalez, *J. Electroanal. Chem.* 503 (2001) 57.
- [53] W.H. Zhu, R.U. Payne, B.J. Tatarchuk, *J. Power Sources* 168 (2007) 211.
- [54] X. Yuan, J.C. Sun, M. Blanco, H. Wang, J. Zhang, D.P. Wilkinson, *J. Power Sources* 161 (2006) 920.
- [55] S. Kamarajugadda, S. Mazumder, *J. Power Sources* 208 (2012) 328.